

INTERACTION OF NON-IDEAL SURFACES IN PARTICULATE SYSTEMS

By

JOSHUA JOHN ADLER

A DISSERTATION PRESENTED TO THE GRADUATE SCHOOL
OF THE UNIVERSITY OF FLORIDA IN PARTIAL FULFILLMENT
OF THE REQUIREMENTS FOR THE DEGREE OF
DOCTOR OF PHILOSOPHY

UNIVERSITY OF FLORIDA

2001

Copyright 2001

by

Joshua J. Adler

This study is dedicated to my father, who taught me that there is science in all things.

ACKNOWLEDGMENTS

I would like to acknowledge my advisor, Brij Moudgil, for giving me the opportunity to pursue a broad range of scientific explorations while enhancing my professional skills. His hard work and attention to detail was an excellent example during my studies. Yakov Rabinovich additionally deserves acknowledgment for introducing me to and guiding me through the finer points and rich history of the interaction of surfaces. Many of the advances achieved during my graduate school career would not have been possible without his assistance. I would also like to thank the National Science Foundation's Engineering Research Center for Particle Science and Technology and our industrial partners for financially supporting this research.

Through my involvement with the Center, I have interacted with a number of professors who have aided me in my graduate school career. Those which deserve special recognition include Hassan El-Shall, Dinesh O. Shah, Rajiv K. Singh, and E. Dow Whitney for their useful discussions, involvement in collaborative projects, and willingness to serve on my advisory committee. Other professors and industry professionals who deserve special recognition include James Adair, Lennart Bergström, P. C. Kapur, Richard Klimpel, Hans Lyklema, Pradip, Mitch Willis, and Abbas Zaman.

My time was further enhanced by the support and collaboration with both past and present students, post-docs, and research scientists including Ali Ata, Bahar Basim, Scott Brown, Aaron Clapp, Kim Christmas, Ravi Domodaran, Madhavan Esayanur, Mike

Fahey, James Fitz-Gerald, Woo-Hyuk Jang, Christopher Izzo, Raja Kalayanaraman, James Kanicky, Dhirendra Kumar, Uday Mahajan, Sharad Mathur, Anders Meurk, Byron Palla, Alex Patist, Robert Pekar, Ron Sabo, Sudhir Shrotri, Pankaj Singh, Prakash Thatavarthy, Steve Truesdale, Rachel Worthen, Joseph Zhu, and all the other students and friends who made my time at the University of Florida interesting.

Lastly, I would like to thank the staff of the Engineering Research Center for Particle Science and Technology including Soo Aldrich, Rhonda Blair, Gill Brubaker, Shelley Burlison, Bret Chen, Anne Donnelly, John Henderson, Lenny Kennedy, Sophie Leone, Kevin Powers, Byron Salter, Erik Sander, Gary Scheiffele, and Nancy Sorkin.

TABLE OF CONTENTS

	<u>page</u>
ACKNOWLEDGMENTS	iv
LIST OF TABLES	ix
LIST OF FIGURES	x
ABSTRACT	xii
1 INTRODUCTION	1
2 INTERPARTICLE FORCE THEORY	7
van der Waals Forces	7
Microscopic Approach	8
Macroscopic Approach	9
Retardation	14
Screening	16
The Derjaguin Approximation	17
Surface Energy Approach to Adhesion	19
Surface Energy	19
Hertzian Mechanics	21
DMT Mechanics	22
JKR Mechanics	24
Electrostatic Forces	26
Origin of Surface Charge	27
Electrical Double Layers	29
Zeta Potential	33
Boundary Conditions for Calculation of Electrostatic Force	35
Linearized Poisson-Boltzmann Approach	38
Non-Linear Approach	40
DLVO and Extended DLVO Theory	43
Surface Force Summary	44
3 ROLE OF ASPERITY GEOMETRY ON THE ADHESION OF SURFACES	45
Introduction	45
Modified Rumpf Model	49
Proposed Model	52
Summary	63

4 ADHESION BETWEEN NANOSCALE ROUGH SURFACES (VALIDATION).....	64
Introduction.....	64
Experimental.....	66
Methods.....	66
Materials.....	67
Results.....	70
Comparison with the Modified Rumpf Model.....	72
Comparison with the Proposed Model (van der Waals Approach).....	74
Comparison with the Proposed Model (Surface Energy Approach).....	80
Summary.....	85
5 CAPILLARY FORCES BETWEEN NANOSCALE ROUGH SURFACES.....	87
Introduction.....	87
Theory.....	90
Adhesion to Surfaces with Nanoscale Roughness.....	90
Capillary Adhesion to Surfaces with Nanoscale Roughness.....	92
A Critical Relative Humidity for Capillary Forces.....	96
Experimental.....	99
Materials.....	99
Methods.....	100
Results and Discussion.....	102
Summary.....	110
6 INFLUENCE OF A TRANSITION LAYER ON INTERPARTICLE FORCE.....	112
Introduction.....	112
Long Range Interaction Forces.....	114
Structuring of Water at the Silica Interface.....	115
Gel-Layer Formation.....	118
Forces between Surfaces with Transition Layers.....	120
Homogeneous Gel-Layer.....	121
Gel-Layer with an Exponential Compositional Decay.....	124
Experimental.....	129
Materials.....	129
Methods.....	130
Results.....	131
Discussion.....	135
Previous Gel-Layer Models.....	135
Homogeneous Gel-Layer Model.....	135
Gel-Layer with an Exponential Compositional Decay.....	138
Summary.....	143
7 SUMMARY AND SUGGESTIONS FOR FUTURE WORK.....	144
Summary.....	144
Suggestions for Future Work.....	146

LIST OF REFERENCES	149
BIOGRAPHICAL SKETCH	156

LIST OF TABLES

<u>Table</u>	<u>Page</u>
2-1 van der Waals Attraction between Different Geometries.....	10
2-2 Components of van der Waals Attraction.....	11
2-3 Results of the Derjaguin Approximation.....	19
4-1 Characteristics of the Model Surfaces	70
4-2 Measured Force of Adhesion.....	71
4-3 Normalized Force of Adhesion: Glass Sphere	83
4-4 Normalized Force of Adhesion: AFM Tip	84
5-1 Substrate Characteristics and Adhesion Parameters.....	107
6-1 Fitting Parameters for the Relative Effective Hamaker Constant	128

LIST OF FIGURES

<u>Figure</u>	<u>Page</u>
1-1 Relative Magnitude of Forces Acting on an Adhered Particle.....	2
2-1 Calculation of the Derjaguin Approximation.	18
2-2 Hertzian Mechanics.	23
2-3 DMT Mechanics.....	24
2-4 JKR Mechanics.....	26
2-5 Schematic of the Stern-Grahame Electrical Double Layer	31
3-1 Asperity Schematic Using the Rumpf Model.....	47
3-2 Prediction of Adhesion Using the Rumpf Model.....	51
3-3 Asperity Schematic Using the Proposed Model.....	53
3-4 Effective Zone of Interaction.....	59
3-5 Comparison of Adhesion Models.....	61
4-1 Experimental Configuration.....	67
4-2 Surface Profiles.....	69
4-3 Comparison of Measured Adhesion with Modified Rumpf Model.....	74
4-4 Asperity Schematic for Surfaces with Two Roughness Scales	76
4-5 Experimental and Theoretical Adhesion for Sphere/Surface Interaction.....	78
4-6 Experimental and Theoretical Adhesion for AFM Tip/Surface Interaction.....	80
5-1 Capillary Schematic.....	93
5-2 Particle/Asperity Capillaries.....	94

5-3 Morphology of CVD Silica Samples.....	101
5-4 Approaching and Retracting Force Profiles	103
5-5 Adhesion Profiles for Silica.....	105
5-6 Adhesion Force Profile for Other Substrates.....	108
6-1 Five Layer Ideal Interaction	123
6-2 Five Layer Non-Ideal Interaction	125
6-3 Effective Hamaker Constant.....	127
6-4 Interaction Force Profile between Boiled Surfaces	132
6-5 Interaction Force Profile between Heat Treated Surfaces	133
6-6 Interaction Force Profile in Attractive Regime	134
6-7 Interaction Force Profile with Electrostatic and DLVO Fitting	136
6-8 Experimental Effective Hamaker Constant	137
6-9 Theoretical van der Waals Force Comparison	140
6-10 Theoretical Interaction Force Profiles	141
6-11 Fitted Interaction Force Profiles.....	142

Abstract of Dissertation Presented to the Graduate School
of the University of Florida in Partial Fulfillment of the
Requirements for the Degree of Doctor of Philosophy

INTERACTION OF NON-IDEAL SURFACES IN PARTICULATE SYSTEMS

By

JOSHUA JOHN ADLER

May 2001

Chairman: Dr. Brij M. Moudgil

Major Department: Department of Materials Science and Engineering

Adhesion between surfaces plays a critical role in the macroscopic behavior of particulate systems such as the flow of cohesive powders, the removal of particulates from substrates, and the formation of particulate coating on host surfaces. Similarly, the repulsive force profile between two particles in suspension influences properties such as rheological behavior and polishing efficiency. The majority of theoretical predictions of surface forces assume that the interface between the particle and surrounding media is ideal. Namely, that there is an atomically sharp demarcation between the properties of the bulk material and the properties of the medium. Furthermore, the interface is often considered perfectly monotonic. While this assumption is likely valid at larger separation distances, significant deviation from theory is expected when two particles are in a contact or near-contact configuration, as they are in adhesion processes or high force operations.

This study explores the impact of the non-ideality of surfaces on the adhesion between particulates in dry and humid atmospheres as well as in solution. Specifically,

the influence of nanoscale roughness in the range of 0.2 to 20 nm RMS has been investigated on the van der Waals, polar, and capillary forces that bind particulates together or prevent particulate removal from surfaces. Additionally, the influence of transition layers, consisting of chemically modified layers of nanoscale thickness at the interface, on the interaction of particulates in suspension has been delineated. For each of these cases, theoretical predictions are developed and validated through direct measurement of surface forces. The presence of non-ideal interfaces is determined to have a significant impact on the magnitude of the surface force that govern the ensemble behavior of many particulate systems.

CHAPTER 1 INTRODUCTION

Particle-particle interactions govern phenomena such as dispersion, agglomeration, coatings, and polishing which play a critical role in materials and product development. The behavior and properties of a particulate system are controlled by the balance of forces acting on a given particle. Gravitational forces are proportional to the radius cubed, whereas, most surface forces are directly proportional to the radius. Hence, the relative importance of surface forces is increased as particle size is reduced.

The balance of forces acting on a particle is shown schematically in Figure 1-1. For a large particle, adhesion behavior, for example, is dominated by gravitational force. The weight of a particle is the principal mechanism that resists removal from surfaces. Alternatively, at very small particle sizes, adhesion due to surface forces dominates. In order to predict behavior, these extremes should be compared to forces that act to remove particle from surfaces. In many cases, such as water or air jets, the removal force is proportional to the particle radius squared (projected area) [MAS94]. Hence, three regimes are often observed in particulate systems as a function of size. Of particular interest in this study, is the middle region of transition between the dominance of surface forces and gravitational force. For many systems this transition occurs in the micron size range.

For particles in this regime, surface forces may be utilized to control the viscosity of suspensions; to separate particles of different properties through operations such as

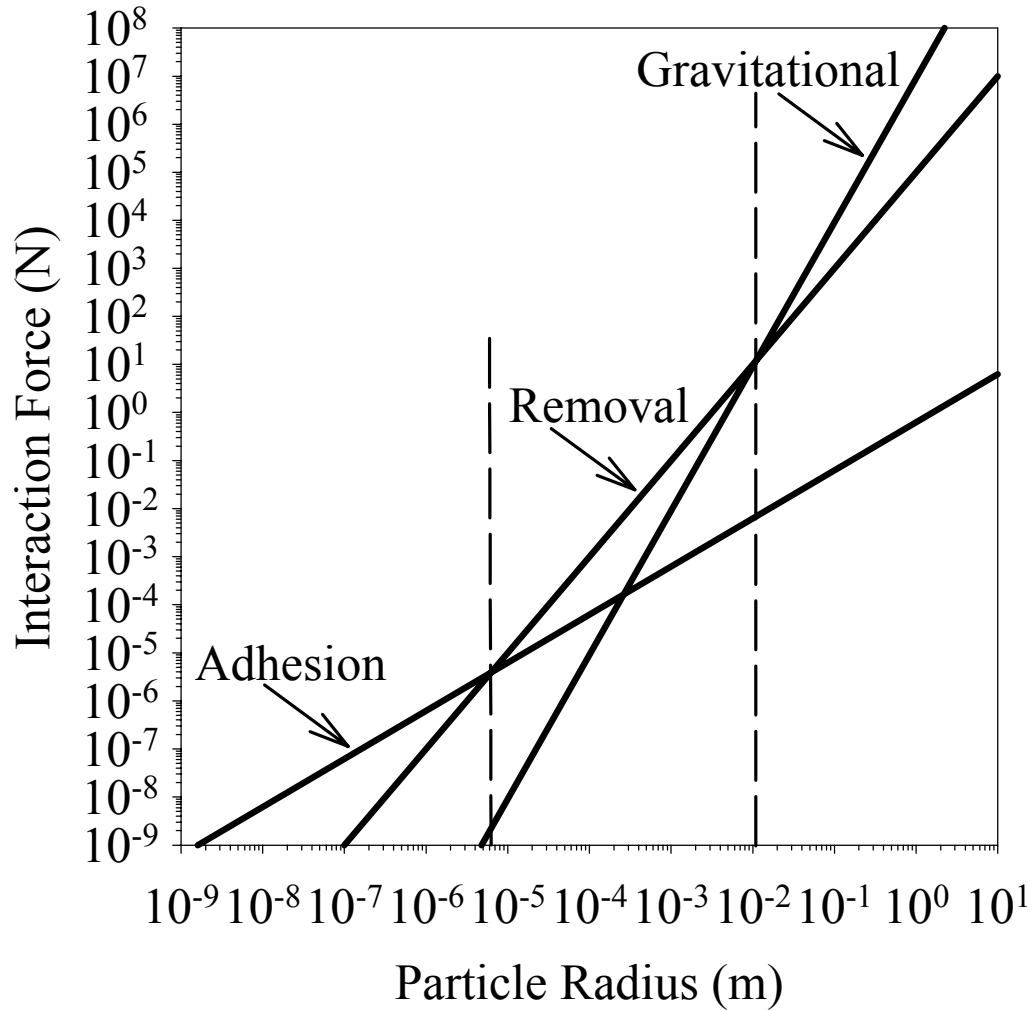


Figure 1-1: Relative Magnitude of Forces Acting on an Adhered Particle. Shown are the relative magnitudes and regions of dominance of adhesion, removal, and gravitational forces for a hypothetical particle adhered to a surface.

filtration, flocculation, or flotation; to polish surfaces with controlled rate and minimal defects; to enhance the flowability of powders; and to synthesize novel particulates by crystallization or particulate coatings. In many of these examples, utilizing the inherent properties of the surface to promote or prevent agglomeration is not sufficient. Rather the surfaces must be modified by chemical additives. These reagents, such as polymers and

surfactants, may be applied to significantly alter the repulsive or attractive forces between particles through a variety of mechanisms.

Similar to the balance surface forces and gravitational forces, there is also competition between surface forces. The net surface force may either be attractive or repulsive depending on the dominance of a particular mechanism. Interactions of surfaces in gaseous media tend to be attractive due to contributions from van der Waals forces, polar forces, plastic deformation, tribocharging, image charging, and capillary condensation. In a liquid medium, the net force may either be attractive or repulsive due to the action of van der Waals, electrostatic, solvation, hydrophobic, and steric forces. In both dry and wet systems, the various forces may not be completely independent of each other, and may significantly affect individual and ensemble particulate behavior.

There have been a number of methodologies developed to predict the interaction of surfaces, as will be discussed further in Chapter 2. However, these models are often based on an ideal model of the surface. The interface between a particle and the medium is characterized as perfectly smooth and discrete. However, most interfaces, due to the reaction with the environment during formation or rearrangement of the bonding between atoms, are compositionally different from the bulk material. The question then arises as to the contribution of the modified interface to the overall force. Most surfaces also have some degree of roughness associated with them. Even for surfaces normally considered smooth, the atoms themselves have an inherent size and thus give rise to roughness that could affect particulate interactions.

For many colloidal systems, such as particulate suspensions under normal conditions, the repulsive force between particulates is large enough that the distance of

closest approach is much greater than the inherent roughness or the thickness of a modified interface. Hence, the overall contribution of such a non-ideal surface is minimized. However, some aspects of the chemically modified interface are accounted for in the classical treatment of the interaction of particles. For instance, the prediction of electrostatic repulsion depends on the number of charges developed after reaction with the environment.

It has not been necessary, until recently, to explore the effect of non-ideal interfaces on other surface force mechanisms in more detail. However, in the field of cohesive powder flow, models are being developed through which ensemble behavior is predicted directly from the interaction and relative movement of particles. This is in contrast to previous approaches that primarily predicted behavior based on empirical measurement of macroscopic properties under controlled conditions. During adhesion processes, particles come into direct contact with one another. In the past, deviations from ideality could be accounted for in a flexible surface energy parameter. However, to implement these newer powder flow models, more realistic prediction of the interaction force is needed.

A more precise description of the interface and its effect on surface force is also becoming necessary in the control of colloidal suspensions, particularly when processing in extreme environments is required. An extreme environment such as high electrolyte concentration, low or high pH, high shear rate, or high normal force may cause particles to interact at much smaller separation distances than under normal solution conditions. An example of such a system is chemical mechanical polishing (CMP) of microelectronic substrates where abrasives under chemically active conditions are pressed into a substrate

by a polymeric pad in order to remove material from the substrate. The nature of the abrasive and substrate surfaces is critical to the prediction of polishing performance. In CMP systems, the properties of the surface must be evaluated at the nanometer level in order to accurately predict forces.

In this study, the influence of two types of non-ideal interfaces is explored. The first is the effect of nanoscale roughness on adhesion forces. It is shown that roughness on the nanoscale has a dramatic influence on adhesion in dry atmospheres, where van der Waals and polar forces are dominant, as well as humid environments, where capillary forces begin to dominate. Theoretical models are developed for both cases and validated by direct measurement of surface forces.

The influence of a compositional alteration of the surface is explained using the silica/water system as an example. In the past, there have been some theories proposed to explain the anomalous short-range surface forces that have been observed in this system. However, none of the approaches can predict the full range of silica's colloidal stability. Through theoretical and experimental methods, a more complete theory of the behavior of silica in aqueous solution and an improved description of the silica surface is advanced.

In all these examples, changes in the surface that dramatically affect the interaction of particles are occurring over length scales of less than 20 nm. Furthermore, it is demonstrated that the most significant deviations from an ideal system occur over a length scales of only 1 to 2 nm. As processes are developed where particle interactions on these same length scales are more common, (e.g. CMP, surface cleaning, coatings), and theoretical predictions of ensemble behavior increasingly rely on accurate prediction of

surface force (e.g. flow of cohesive powder, viscosity of concentrated suspensions), the need to more precisely describe surface properties and develop models to predict surface forces is clear. The following chapters are expected to advance the state-of-the-art toward this goal.

The discussion will begin, in Chapter 2, with a brief overview of surface force predictions between ideal surfaces relevant to the mechanisms described in later chapters. Chapter 3 will define a model based on the geometry of a non-ideal surface with nanoscale roughness to predict particulate adhesion. This model will then be experimentally validated and expanded upon in Chapter 4. Chapter 5 introduces capillary adhesion and explores effects, due to nanoscale roughness, on the magnitude and onset of capillary adhesion. In Chapter 6 an alternate type of non-ideal interface is discussed. The effect of a surface layer, differing in composition from the bulk, on the interaction of particles in suspension will be delineated. Finally, Chapter 7 will summarize the findings of this investigation and propose possible avenues for further research.

CHAPTER 2 INTERPARTICLE FORCE THEORY

Before a detailed discussion of the interaction of non-ideal surfaces, a brief description of current theory regarding the interaction of ideal surfaces is necessary. The topics presented in this chapter are intended to introduce the fundamentals of surface forces relating to interactions in gaseous atmospheres and between particles in aqueous suspension. The scope and application of surface forces is large. Hence, the following discussions will be limited to concepts necessary for interpretation of the specific examples in this study.

van der Waals Forces

In 1873, J. D. van der Waals [VAN73] first suggested that the behaviors of gases and their deviation from ideality could be expressed as a modification of the ideal gas law, $PV = nRT$, to

$$\left(P + \frac{n^2 a}{V}\right)(V - nb) = nRT \quad (2-1)$$

where P is pressure, n is the number of moles of gas, V is the volume, R is the gas constant, T is temperature, and a and b are constants specific to a particular gas. This modification is significant because a number of assumptions are inherent in the interpretation of the constants a and b . The constant b particularly describes the finite volume of the molecules comprising the gas and the constant a is needed to describe attractive forces between the molecules. A primary result of this development was a significantly improved model of the behavior of gases. The various types of attractive

forces between molecules are now collectively termed van der Waals forces. The concept of an attractive force was also used to describe the properties of condensed matter. The familiar Lennard–Jones potential [LEN28]

$$W_{\text{atom/atom}} = -\frac{C}{r^6} + \frac{B}{r^{12}} \quad (2-2)$$

where the net potential energy between atoms, $W_{\text{atom/atom}}$, at distance, r , can be described by the competition of an attractive London dispersion forces [LON37], characterized by constant C and a Born repulsion term (arising from the overlap of electron clouds) characterized by constant B . The London constant, C , is primarily related to the synchronization of instantaneous dipoles created when the energy fields of neighboring atoms overlap. Both these expressions of the attraction between atoms becomes evident when the dispersion constant is related to a and b in the non-ideal gas law through

$$C = \frac{9ab}{4\pi^2 N_a^3} \quad (2-3)$$

where N_a is Avogadro's number. The characteristic frequencies principally associated with this constant are in the infrared to ultraviolet range of light and are principally associated with the opacity of solids. As such, the term dispersion force is often used.

Microscopic Approach

Hamaker [HAM37], Derjaguin [DER34], and de Boer [DEB36] all contributed significantly to the understanding of the van der Waals interactions between macroscopic bodies based on the individual interactions of London dispersion forces between atoms. In the microscopic approach, it is assumed that pairwise addition of all the interactions between the atoms in one body with another body may be used to derive an expression for the energy of attraction between them. Following this approach, the interaction energy, W , between two spherical particles may be expressed in the following manner.

$$W_{\text{sph/sph}} = \frac{A}{6} \left[\frac{2R^2}{H(4R+H)} + \frac{2R^2}{(2R+H)^2} + \ln \left(1 - \frac{4R^2}{(2R+H)^2} \right) \right] \quad (2-4)$$

where A is Hamaker's constant, R is the particle radius, and H is the separation distance between the particle surfaces. Note that this relation does not place a restriction on particle size. However, if it is considered that the radius of the two particles is much greater than the separation distance, the expression may be reduced to the more familiar form represented by Eq. (2-5) [DER34].

$$W_{\text{sph/sph}} = \frac{AR}{12H} \quad (2-5)$$

Energies of interaction based on different geometries, assuming the extent of the van der Waals attraction is small compared to the radius of curvature, are given in Table 2-1. However, the more important outcome of these initial approaches was the separation of the fundamental nature of the interaction of materials from their geometry. In this manner the force or energy between two bodies may be expressed as a factor which may be changed depending on shape and a constant resulting from the material's fundamental composition. This is a critical development considering that although the total van der Waals attraction is dominated by the London dispersion component, arising from the interaction of instantaneous dipoles, there are a number of other mechanisms that should often be taken into account when considering the total attraction. Table 2-2 describes a number of these forces and the corresponding atomic/molecular interactions.

Macroscopic Approach

In real materials there may be many fundamental interactions which contribute to the total interaction force. Additionally in the microscopic approach, the interaction between atoms or dipoles is calculated as if a vacuum were intervening. However,

considering an atom at the core of a solid particle interacting with an atom in the core of another particle, this is clearly not the case. The intervening atoms have a significant impact on the interaction. Hence, it is desirable to determine an improved method to predict the attraction between solids that takes into account the different types of interactions and more accurately sums them. Accounting for the types and orientations of the many type of species in a solid is difficult and hence a different approach must be taken. In 1956 Lifshitz [LIF56], based on the assumption that both the static and

Table 2-1: van der Waals Attraction between Different Geometries. Theoretical formulae for the prediction of the energy or force of attraction between bodies of differing geometries where A is Hamaker's constant, H is surface separation distance, R_1 and R_2 are particle/cylinder radii, and L is cylinder length. Note that these were derived for conditions in which the extent of significant van der Waals attraction is far less than the radius of the particles or cylinders and that force is the negative differential of energy.

Geometry of Interaction	Energy of Interaction (J)	Force of Interaction (N)
Two Plates	$\frac{A}{12\pi H^2}$	$\frac{A}{6\pi H^3}$
Sphere/Plate	$\frac{AR}{6H}$	$\frac{AR}{6H^2}$
Sphere/Sphere	$\frac{A}{6H} \frac{R_1 R_2}{(R_1 + R_2)}$	$\frac{A}{6H^2} \frac{R_1 R_2}{(R_1 + R_2)}$
Crossed Cylinders	$\frac{A\sqrt{R_1 R_2}}{6H}$	$\frac{A\sqrt{R_1 R_2}}{6H^2}$
Parallel Cylinders	$\frac{AL}{12\sqrt{2}H^{3/2}} \sqrt{\frac{R_1 R_2}{R_1 + R_2}}$	$\frac{AL}{8\sqrt{2}H^{5/2}} \sqrt{\frac{R_1 R_2}{R_1 + R_2}}$

oscillatory fields produced by the atomic components of solids should directly affect the absorption of electromagnetic energy by the material, derived a method to calculate the attraction between materials based on the differences in their dielectric spectra. Thus, the continuum or macroscopic approach was founded. Although it is clear that this approach

Table 2-2: Components of van der Waals Attraction. Theoretical predictions of the possible contributions to the total attraction between particles. Q is the electric charge (C), u is the electric dipole moment (Cm), α is the electric polarizability (C^2m^2/J), r is the distance between interacting atoms or molecules (m), k is Boltzmann's constant (1.381×10^{-21} J/K), T is absolute temperature (K), h is Plank's constant (6.626×10^{-14} Js), ν is the electronic absorption (ionization) frequency (1/s), and ϵ_0 is the dielectric permittivity of free space (8.854×10^{-12} C²/Jm) [ISR92].

Interaction Type	Interaction Energy	
Covalent/Metallic	Complicated	
Charge – Charge	$Q_1Q_2/(4\pi\epsilon_0r)$	Coulomb
Charge - Fixed Dipole	$-Qu \cos(\theta)/(4\pi\epsilon_0r^2)$	
Charge – Rotating Dipole	$-Q^2u^2/(96\pi^2\epsilon_0^2kTr^4)$	
Fixed Dipole – Rotating Dipole	$-u_1u_2[2\cos(\theta_1)\cos(\theta_2)-\sin(\theta_1)\sin(\theta_2)\cos(\phi)]/(4\pi\epsilon_0r^3)$	
Two Rotating Dipoles	$-u_1^2u_2^2/(48\pi^2\epsilon_0^2kTr^6)$	Keesom
Charge - Nonpolar	$-Q_2\alpha/(32\pi^2\epsilon_0^2r^4)$	
Fixed Dipole - Nonpolar	$-u^2\alpha(1+3\cos^2(\theta))/(32\pi^2\epsilon_0^2r^6)$	
Rotating Dipole - Nonpolar	$-u^2\alpha/(16\pi^2\epsilon_0^2r^6)$	Debye
Two Nonpolar	$-3h\nu\alpha^2/(64\pi^2\epsilon_0^2r^6)$	London Dispersion
Hydrogen Bond	Roughly proportional to r^2	

accounts for the different types of bonding and screening in a body, it is still a very difficult function to measure due to the wide range of frequencies and types of experiments needed to determine the entire function.

To overcome this barrier Ninham and Parsegian [NIN70a] in the early seventies proposed that the principle contributions to the overall attraction come from the regions of dielectric relaxation. In other words, the regions where a specific atomic or molecular mechanisms creates a resonant vibration. The characteristic absorption frequencies of some materials are relatively well characterized, for example the spectra of water has been characterized in the ultraviolet, infrared, microwave, and static frequency regimes [GIN72, DAG00]. However, it is still difficult to extract information for a wide variety of materials.

To simplify this situation it was demonstrated, by Hough and White [HOU80], that the majority of the contributions to the overall Hamaker constant come from dielectric relaxations in the UV and infrared regions. This may be expressed in a simplification of the Ninham-Parsegian representation as Eq. (2-6)

$$\epsilon(i\xi) = 1 + \frac{C_{\text{IR}}}{1 + (\xi/\omega_{\text{IR}})^2} + \frac{C_{\text{UV}}}{1 + (\xi/\omega_{\text{UV}})^2} \quad (2-6)$$

where ϵ is the dielectric response function as a function of the imaginary frequency $i\xi$, C is the spectral constant in the IR and UV regions, ω is the characteristic absorption frequency in the IR and UV regions, and ξ is a constant frequency equal to $(4\pi^2 kT/h)$ in which k is Boltzmann's constant, T is absolute temperature, and h is Plank's constant.

This approximation was found to be valid for materials that are transparent and exhibit negligible absorption or where $\epsilon(\omega) \cong n^2$, n being the index of refraction. Note

also that for these conditions the UV spectral constant, C_{UV} , may be related to the index of refraction in the visible regime, n_{VIS} , through

$$C_{UV} = n_{VIS}^2 - 1 \quad (2-7)$$

and the spectral constant in the IR regime, C_{IR} , may be approximated by the static dielectric constant, $\epsilon(0)$, and C_{UV} through Eq. (2-8).

$$C_{IR} = \epsilon(0) - C_{UV} - 1 \quad (2-8)$$

Using these approximations the Hamaker constant can now be expressed by the static dielectric constant and the UV absorption parameters. To acquire these UV parameters the index of refraction in the visible and UV regions may be measured and according to the Cauchy equation,

$$n^2(\omega) - 1 = (n^2(\omega) - 1) \frac{\omega^2}{\omega_{UV}^2} + C_{UV} \quad (2-9)$$

plotted to extract C_{UV} and ω_{UV} . The UV relaxation frequency for such materials is relatively constant at approximately 3×10^{15} Hz. Considering a single UV relaxation frequency, an approximation for the Hamaker constant, A_{131} , of material 1 interacting with similar material through medium, 3, may be written solely as a function of the differences in the static dielectric constants, $\epsilon(0)$, and indices of refraction in the visible range, n . The result is the Tabor-Winterton (TAB69) approximation

$$A_{131} = \frac{3kT}{4} \left(\frac{\epsilon_1(0) - \epsilon_3(0)}{\epsilon_1(0) + \epsilon_3(0)} \right)^2 + \frac{3h\omega_{UV}}{32\pi\sqrt{2}} \frac{(n_1^2 - n_3^2)^2}{(n_1^2 + n_3^2)^{3/2}} \quad (2-10)$$

where kT is the product of Boltzmann's constant and temperature and h is Plank's constant. Note also that a similar equation may be derived for the interaction of dissimilar materials, 1 and 2, across medium 3.

$$A_{132} = \frac{3}{4} kT \left(\frac{\epsilon_1(0) - \epsilon_3(0)}{\epsilon_1(0) + \epsilon_3(0)} \right) \left(\frac{\epsilon_2(0) - \epsilon_3(0)}{\epsilon_2(0) + \epsilon_3(0)} \right) + \frac{3h\omega_{UV}}{16\pi\sqrt{2}} \frac{(n_1^2 - n_3^2)(n_2^2 - n_3^2)}{(n_1^2 + n_3^2)^{1/2} (n_2^2 + n_3^2)^{1/2} \left[(n_1^2 + n_3^2)^{1/2} + (n_2^2 + n_3^2)^{1/2} \right]} \quad (2-11)$$

Through the methodologies described above, a relatively comprehensive theory of the interaction of surfaces has been developed. However, there is still a debate as to which measurements of the spectral constants and which approximations are most valid [BER96, DAG00, FER00]. Hence, as models are developed that more accurately link nanoscale phenomena with ensemble behavior, it is expected that more accurate determination of many of the constants proposed in the literature will be necessary.

Retardation

The principle atomic process that controls the magnitude of the van der Waals forces between surfaces is the synchronous oscillations between instantaneous dipoles in the two materials, known as London dispersion forces [LON37]. However, the speed at which the field of one instantaneous dipole may interact with another is limited by the speed of light. As a result, when two bodies are moved further apart there is more of a phase lag between the alignment of dipoles, this results in the magnitude of the total van der Waals force being reduced from that predicted by the non-retarded value. Another consequence of this phenomenon is that as the magnitude of the contribution to the total van der Waals force of the instantaneous dipoles decreases, the relative contribution of the static dipoles (permanent dipoles/charges) increases.

There are several methods to account for the decreased efficiency of interaction between the instantaneous dipoles. It has been demonstrated that the full numerical

solution to the Lifshitz equations do account for retardation [MAH76, PAS77].

However, these calculations are tedious and the full dielectric spectra for many materials is not described adequately. Hence, for separation distances where the contribution of instantaneous dipoles is still significant, approximately 5 to 15 nm in water, Gregory [GRE81] has proposed an analytical correction, given by Eq. (2-12),

$$A_{\text{ret}} = A \left[1 - 5.32 \frac{H}{\lambda} \ln \left(1 + \frac{1}{5.32H/\lambda} \right) \right] \quad (2-12)$$

where A_{ret} is the retarded Hamaker constant, A is the non-retarded Hamaker constant, H is surface separation distance, and λ is the London wavelength (characteristic wavelength for instantaneous dipole oscillation: approximately 100 nm).

At larger separation distances the contribution of instantaneous dipoles becomes small. Under this assumption Casimir and Polder [CAS48a] derived an expression for van der Waals energy between two plates, $W_{\text{plt/plt}}$, of the form

$$W_{\text{plt/plt}} = \frac{B_{131}}{3H^3} \quad (2-13)$$

where B (Jm) is a constant analogous to that of Hamaker equal to

$$B_{131} = \frac{\pi c h}{480 \sqrt{\epsilon_3(0)}} \frac{(\epsilon_1(0) - \epsilon_3(0))^2}{(\epsilon_1(0) + \epsilon_3(0))^2} \Phi \quad (2-14)$$

where $\epsilon(0)$ is the static dielectric constant of material 1 or medium 3, c is the speed of light, h is Plank's constant, and Φ is 0.24 for dielectrics and 1 for conductors.

Note that at large separation distances the magnitude of the van der Waals forces under these assumptions decays as a function of H^3 instead of H^2 as predicted by a non-retarded interaction. Hence, even for separation distances in the 5-15 nm regime the measured forces may be less than approximately half that predicted by non-retarded theory. At larger distances in water, the absolute magnitude of the interaction energy due to van der Waals attraction approaches that of Brownian motion (~ 1 kT) and as such the

long range formulas are not often applied. However, for non-contact interactions in gaseous atmosphere, they may need to be considered.

Screening

Screening is a phenomena similar to retardation in that it acts to reduce the total van der Waals interaction between surfaces. However, screening primarily acts to reduce the contribution of the static component of the total interaction energy and occurs primarily in aqueous solutions. The van der Waals interaction is essentially an electromagnetic effect. As such, free charges such as ions in solution will act to reduce the field strength. In real systems, this effect may act to reduce the static attraction term, see Eq. (2-10) or (2-11), over very short separation distances.

For example in a 0.1 M aqueous solution at 1 nm separation distance the static contribution to the van der Waals force will be approximately 10% of its contribution at zero separation distance. Hence at larger separations in high ionic strength solutions the interaction is primarily controlled by London dispersion forces. This effect has been described mathematically by Mahanty and Ninham [MAH76] for non-retarded van der Waals forces through Eq. (2-15).

$$A_{\text{screen}} = A_{\omega=0} (2\kappa H)e^{-2\kappa H} + A_{\omega>0} \quad (2-15)$$

where A_{screen} is the screened Hamaker constant, $A_{\omega=0}$ is the zero frequency Hamaker constant component, $A_{\omega>0}$ is the sum of all the other components, H is separation distance, and κ is a characteristic inverse length, called the Debye-Hückel parameter (the inverse is commonly called the Debye length) that describes the distribution of ions near a charged interface according to

$$\kappa = \left(\frac{2nZ^2e^2}{\epsilon_r\epsilon_0kT} \right)^{1/2} \quad (2-16)$$

where n is the number concentration of ions, Z is ion valency, e is the fundamental charge on an electron, ϵ_r is the relative dielectric constant of water (static), ϵ_0 is the permittivity of free space, and kT is the product of Boltzmann's constant and absolute temperature.

The Derjaguin Approximation

In the previous section, a methodology to determine the interaction between bodies was discussed. Using the microscopic approach, Hamaker was able to separate the critical interaction components into a material constant and a factor dependent on the geometry of the interacting surfaces [HAM37]. While the macroscopic approach delineated more clearly the value of the Hamaker constant, changes in the geometry of the interacting bodies is still a difficult multidimensional integration process.

An approach to simplify this problem was proposed by Derjaguin in 1934 [DER34]. It was proposed that the energy of interaction between two bodies could be calculated based on the summation of the interaction force as separation distance, H' , goes from H to infinity for infinitesimally thin concentric rings of radius x and thickness dx interacting with the projection of that ring on the opposing body as if it were two plates of area $2\pi dx$ separated by H' , as shown in Figure 2-1. If the assumption is then made that the range of the force between the interacting bodies is small compared to their radii and that at large separation distances the magnitude of the interaction approaches zero, relatively simple relations for the energy of interaction between flat plates and the force of interaction between bodies of differing shapes may be extracted.

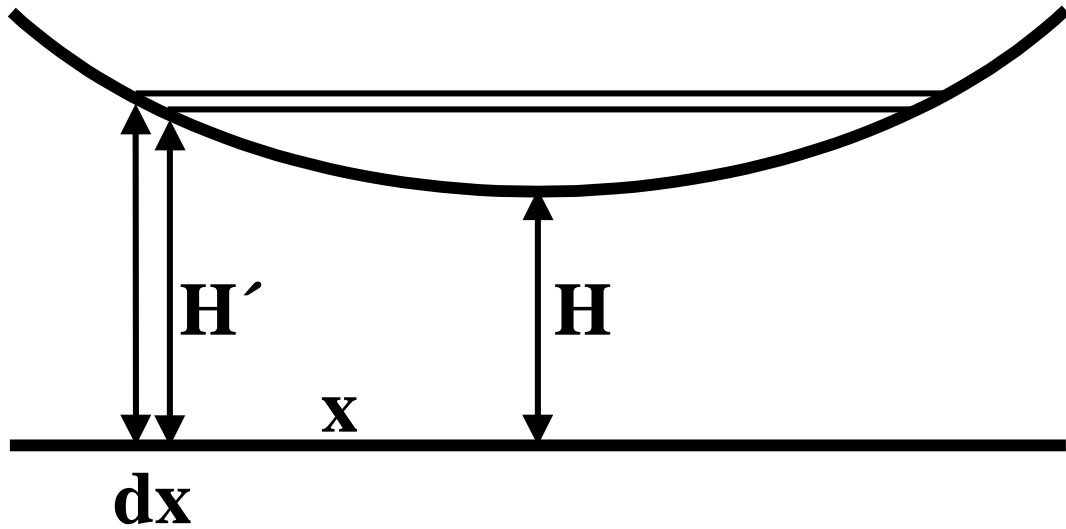


Figure 2-1: Calculation of the Derjaguin Approximation. Integration of the force between the flat surface created by a ring of thickness dx and radius x with its projection on the sphere as separation distance goes from H to ∞ yields the equivalent energy between flat surfaces.

This approximation is extremely important for the measurement of surface forces because it simplifies the derivation of analytical formulae and allows comparison between bodies of different geometries. Although van der Waals attractive force has a relatively simple form, other forces are considerably more complicated and derivation or integration may not yield analytical solutions. Additionally, many computations, such as the distribution of ions from a charged interface, are simplified if the interface is flat. As illustrated in Table 2-3, multiplying the interaction energy between flat surfaces by a factor, the force between different geometry bodies may be calculated.

An even more important result of this approximation is that all of the forces or energies of interaction between curved bodies are seen to be directly proportional to the radius or mean radius. Hence, forces measured between spheres, cylinders, and plates

may be directly related to each other. Moreover, experiments measured between surfaces of differing radii may also be compared to a single theoretical prediction. Surface forces for this reason are often presented normalized by the radius of the interacting bodies. Note that in this form, force divided by radius is equivalent to energy per unit area.

Surface Energy Approach to Adhesion

Surface Energy

The application of the above models, based on van der Waals attraction, are necessary to describe the distant dependent nature of the interaction of surfaces. However, for the specific case when two surfaces are in contact, a different approach to quantify the magnitude of the adhesion force may be considered. The work of adhesion (cohesion for similar materials) describes the energy needed to bring two half spaces (flat plates) from contact to infinite separation distance. This work, W_{132} , may be further described, Eq. (2-17), as the sum of the surface energies, γ_{13} or γ_{23} , associated with the newly created interfaces.

Table 2-3: Results of the Derjaguin Approximation. The interaction force, F , between surfaces of different geometries, according to the Derjaguin approximation, is the energy of interaction between flat plates, $W_{\text{plt/plt}}$, multiplied by a simple prefactor.

Geometry of Interaction	Force	Derjaguin Approximation
Sphere/Plate	$F_{\text{sph/plt}}$	$(2\pi R)W_{\text{plt/plt}}$
Sphere/Sphere	$F_{\text{sph/sph}}$	$(\pi R)W_{\text{plt/plt}}$
Crossed Cylinders	$F_{\text{cyl/cyl}}$	$(2\pi R)W_{\text{plt/plt}}$

$$W_{132} = \gamma_{13} + \gamma_{23} \quad (2-17)$$

For liquid interfaces the surface energy is normally referred to as surface tension. For solid materials in very close contact, this quantity may be referred to as fracture energy. Since the contact separation distance at which surface energy is defined is not specified, different methods of evaluating surface energy are expected to provide different values. For example between two liquid interfaces, separation distance may be taken as the intermolecular distance (minimum in the Lennard-Jones potential) which is approximately 0.16 nm [ISR92]. However, between two adhered solid surfaces the atoms are not free to arrange themselves and separation distance is often larger (approximately 0.3 to 0.4 nm for many materials). Additionally, different types of bonding may occur in different systems. Considering two adhered silica surfaces, surface energy measurements based on adhesion result in values of γ_{13} of 25 to 40 mJ/m², depending on the degree of hydroxylation [BRA32, YAM75, YAM98]. However, surface energy based on fracture is approximately 5000 mJ/m² [ASH91]. This enormous discrepancy is reasonable if it is considered, that in the case of fracture, covalent bonds must be overcome to separate the surfaces. Consequently, surface energy values are often derived from a number of different sources and may not always incorporate the true fundamental mechanisms of adhesion relevant to a specific system.

The surface of a material is often different from the bulk. For example hydroxyl groups or other polar groups often satisfy the broken bonds at the interface. These species normally have a dipole moment, or may form hydrogen bonds (acid/base reactions) with similar species. These dipoles at the interface are not accounted for in the determination of van der Waals forces between surfaces in which the interface is treated as a sharp

transition between the properties of the body and medium. On the other hand, these polar groups may add significantly to the measured adhesion. For a surface with a high concentration of hydroxyl groups, such as silica, the contribution of van der Waals adhesion, assuming a 0.3 nm minimum separation distance, results in a contribution of only 9.5 mJ/m^2 to the total measured surface energy (25-40 mJ/m^2). For more hydrophobic materials this contribution is significantly less but should still be considered.

It is known that contributions to adhesion from polar forces decay sharply with distance and essentially are only critical for surfaces in contact in gaseous atmospheres. Unfortunately, adequate characterization of the orientation, concentration, and contribution of the individual polar groups is not available. Because of the importance of these polar forces, many investigators chose to work with the surface energy approach to describe adhesion phenomena. Considering that surface energies are dependent on surface history and are generally poorly characterized, this parameter is often used to fit experimental data. Despite this limitation, there is substantial theory to describe the interaction of particles based on the surface energy approach. Since contact is assumed, these approaches are generally valid only after contact has been achieved.

Hertzian Mechanics

When a particle is in contact with a surface, for example, there are generally two classes of forces acting between the bodies. The forces mentioned in the preceding sections tend to attract the particle towards the surface. If the particle were a liquid droplet, after contact, these forces would begin to deform the droplet until the surface was wetted. However, for solid materials this deformation is resisted by the force needed to

elastically deform the particle. This force of resistance to elastic deformation, $F_{\text{sph/plt}}$, was described mathematically by Hertz [HER81] and may be written as

$$F_{\text{sph/plt}} = \frac{Ka^3}{R} \quad (2-18)$$

where a is the radius of the contacting area between the particle and plate, R is the radius of the particle, and K is the reduced elastic modulus. Note that

$$K = \frac{4}{3} \left[\left(\frac{1-\nu_1^2}{E_1} \right) + \left(\frac{1-\nu_2^2}{E_2} \right) \right]^{-1} \quad (2-19)$$

where ν is Poisson's ratio and E is the elastic modulus for materials 1 and 2. From these relations the indentation depth, δ , relative to initial contact ($\delta = 0$) may also be determined.

$$\delta = \frac{a^2}{R} \quad (2-20)$$

The above forces are purely repulsive and act to keep the particle from deforming. In fact, with no externally applied force, the model predicts zero deformation, zero radius of contact, and zero surface force, Figure 2-2. In systems that behave according to the Hertzian indentation model, attractive surface forces should be negligible. For particles in the micron-size regime, this assumption is not generally valid. Instead the attractive forces act to pull the particle towards the plate. This action is resisted by Hertzian repulsion. An account of net area in contact based on this model was proposed by two groups for different limiting cases and is described below.

DMT Mechanics

Derjaguin, Muller, and Toporov [DER75] proposed, in the limiting case of high elastic modulus, small particle size, low attractive forces or appropriate combination of the above, that any deformation that occurs will not significantly affect the force of

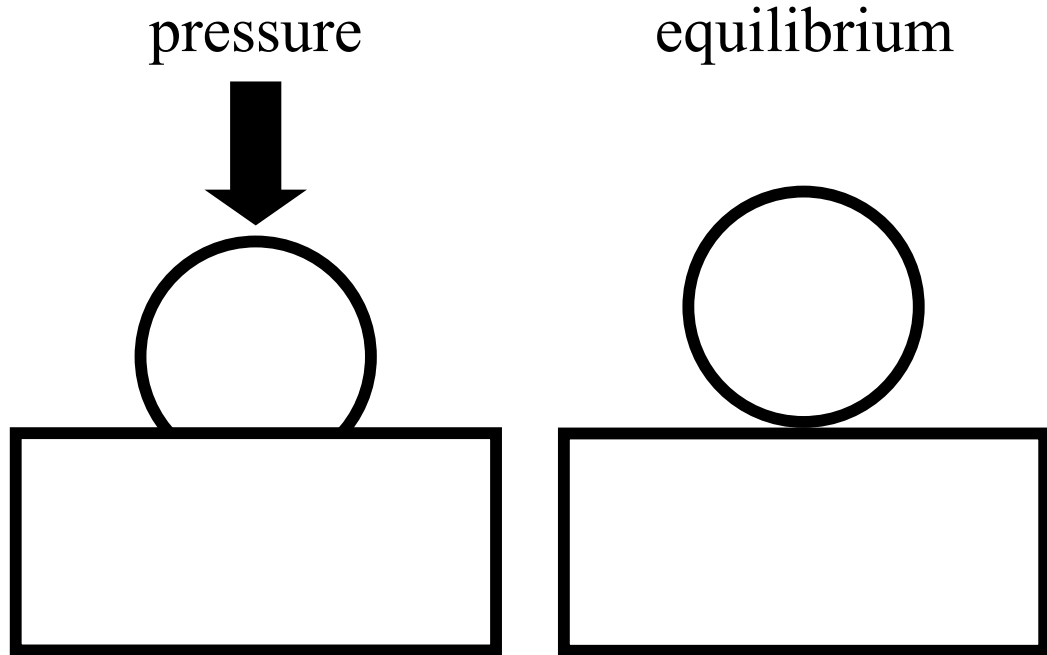


Figure 2-2: Hertzian Mechanics. Under pressure, the particle resists being pushed into the surface by elastic deformation. At equilibrium, the particle is neither attracted nor repelled from the surface.

attraction between the sphere and flat plate. Hence the resulting interaction may be written as

$$F_{\text{sph/plt}} = \frac{Ka^3}{R} - 4\pi R\gamma_{131} \quad (2-21)$$

where the first term is Hertzian repulsion and the second is attraction. As indicated by Fig. 2-3, The indentation depth for this model is the same as for the Hertzian model, Eq. (2-20). In DMT mechanics, when the particle detaches from the surface the area in contact is zero and the particle is truly not deformed. In other words, the force applied to remove the particle exactly equals the adhesion term and Hertzian repulsion is zero. Hence, the force of adhesion may be written as Eq. (2-22).

$$F_{\text{adhesion: sph/plt}} = 4\pi R\gamma_{131} \quad (2-22)$$

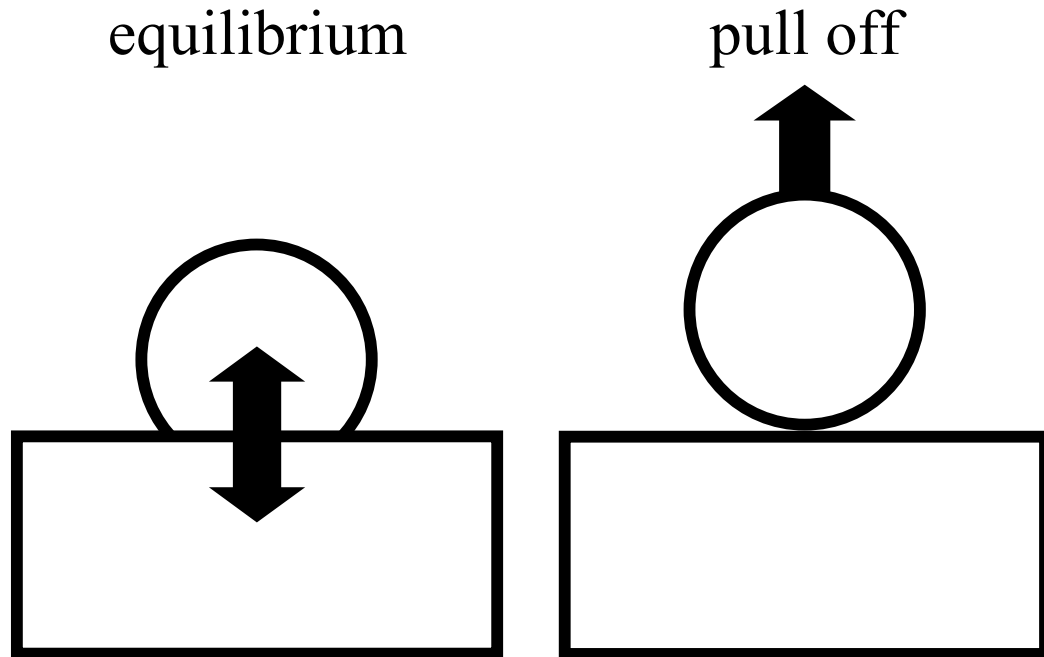


Figure 2-3: DMT Mechanics. At equilibrium, attractive surface forces are balanced by Hertzian repulsion arising from elastic deformation. At pull-off, removal force equals surface force and the particle is not deformed.

It should be noted that Eq. (2-22) is really equivalent to the Derjaguin approximation, $F_{\text{sph/plt}} = 2\pi RW_{131}$. The difference is that in this methodology the work of adhesion is a specific value independent of separation distance. The simplicity of these mechanics is due to the assumption of a rigid spherical body. However, many materials such as latex, do not fit the assumptions made in the DMT model.

JKR Mechanics

To extend the model to cases where deformation of the particle should be accounted for, Johnson, Kendall, and Roberts [JOH71], in the limiting case of low elastic modulus, large particle size, high attractive forces or appropriate combination of the

above, derived an expression for the attraction between a particle and a plate as a function of the radius of the contact area, a ,

$$F_{\text{sph/plt}} = \frac{Ka^3}{R} - \sqrt{12\pi Ka^3 \gamma_{131}} \quad (2-23)$$

where K is the reduced elastic modulus, R is the particle radius, and γ_{131} is surface energy. The depth of indentation, δ , also has a very different functional form as shown in Eq. (2-24).

$$\delta = \frac{a^2}{R} - \frac{2}{3} \sqrt{\frac{12\pi a \gamma_{131}}{K}} \quad (2-24)$$

In the JKR scheme, because the surfaces are deformable, detachment of the particles does not occur when the penetration depth is zero as in the DMT model, as shown in Fig. 2-4. Instead as the particle is pulled from the surface a neck forms between the two surfaces as they try to remain adhered. Detachment occurs when the neck becomes too thin to maintain contact ($dF/da = 0$). In this case, the force of adhesion may be written as, Eq. (2-25).

$$F_{\text{adhesion: sph/plt}} = 3\pi R \gamma_{131} \quad (2-25)$$

There are alternative descriptions of the interaction of surfaces, such as Maugis mechanics for spheres and plates, that more accurately predict adhesion between the DMT or JKR limits based on material properties [MAU92]. However, for practical application, the magnitude of the force of adhesion predicted by JKR mechanics is 75% of that predicted by the DMT model. This difference is relatively small compared to the uncertainty in the magnitude of the surface energy. Another complication arises from the comparison of bodies of differing geometry. In the literature, the Derjaguin approximations are commonly applied to both JKR and DMT mechanics. However, the validity of these transformations has not been adequately tested.

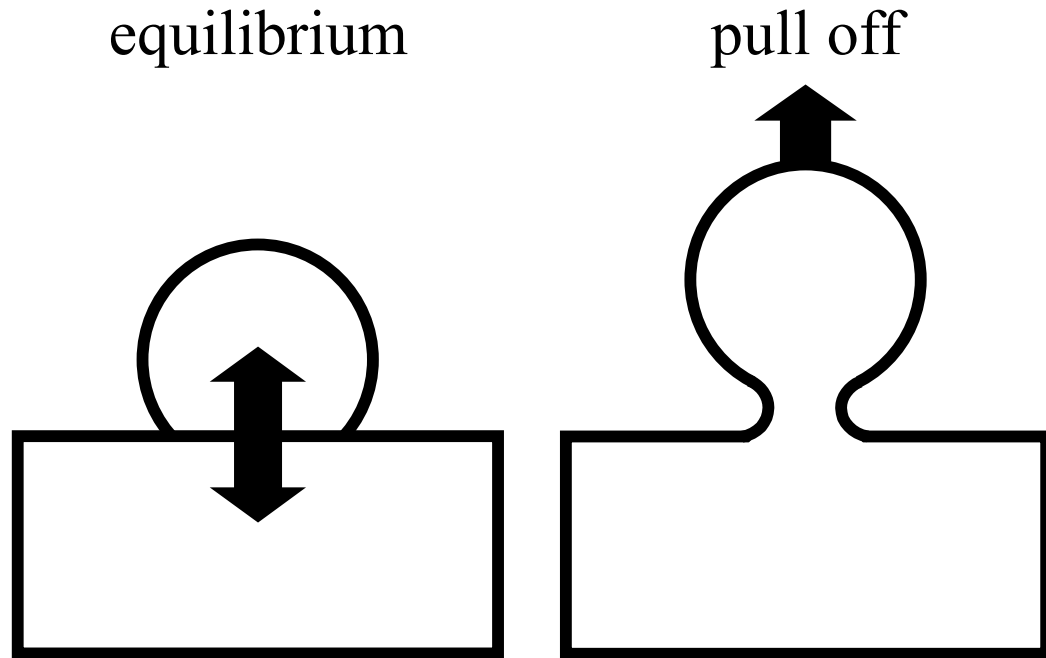


Figure 2-4: JKR Mechanics. At equilibrium, attractive surface forces (although with a different functional form than in DMT mechanics) are balanced by Hertzian repulsion arising from elastic deformation. At pull-off, JKR mechanics predicts neck formation. The maximum force of adhesion occurs when the neck breaks.

Electrostatic Forces

The forces described above, with the exception of polar forces, operate at some level whether the particles are in gaseous atmospheres or in aqueous suspension. Additionally, the forces mentioned above are usually attractive. However, when particles are introduced to an aqueous medium they often develop charge at the solid/water interface. If the charges are of the same sign the particles will repel each other. This force that is often utilized to prevent coagulation in suspensions is called electrostatic repulsion.

Origin of Surface Charge

Charge on the surface of particles may develop through a variety of mechanisms. When new surface area is created either through precipitation, fracture, or other mechanisms the atoms at the interface seek to lower their free energy by combining with molecules from their environment. In the case of oxides, nitrides, carbides, phosphates, or sulfides this often takes the form of surface hydroxyl, nitride, carboxylate, phosphate, or sulfate groups. These groups are essentially Brönsted acids and, as such, upon immersion in aqueous solution may dissociate. This dissociation is often characterized by a reaction rate equation such as



where MOH represents a metal hydroxide, for example, and K is a rate constant equal to

$$K = \frac{[\text{M}^+][\text{OH}^-]}{[\text{MOH}]} \quad (2-27)$$

with the brackets indicating surface concentrations. Using this terminology it is clear that the relative magnitude of the charge at the interface is highly dependent on the concentration of hydroxyl, hydronium, and metal ions at the interface. Dissolved species, such as these, that may directly affect surface charge are called potential determining ions.

Of course, most surfaces have more than one type of group either due to a multi-atomic composition, the propensity to form multiple hydroxylated (or other) species, or changes in the local surface molecular architecture. Similarly, dissolved ions from the surface, especially metal oxides in aqueous solution, may form a number of species in solution. All these factors can affect the actual dissociation constant. However, for most dissociating materials in water, there is a general trend that at low pH surface charge is positive and negative at high pH. The pH at which there is a net zero charge on the

surface is called the point of zero charge (PZC) and is generally characteristic of a particular material.

A second method of generating charges at the interface of a particle is through selective dissolution or adsorption of ions. Many salts including AgI, BaSO₄, CaF₂, NaCl, and KCl generate charge through this mechanism. The origin lies in the more favorable solubility of one of the ionic constituents over the other and may be predicted through a combination of hydration energy and surface hydration [VEE97]. The balance between the ions in this case may be quite delicate as exemplified by the fact that NaCl has a net positive charge due to the enhanced dissolution of chlorine, whereas KCl has a net negative charge due to enhanced dissolution of potassium [MIL92]. These systems may also approach equilibrium (saturation) as in the case of AgI where the difference in concentration of the potential determining ions (Ag⁺ or I⁻) determines surface charge. Several clay minerals, such as mica, may also develop charge via this mechanism. If charges between layers are satisfied by metal cations such sodium, potassium, calcium, or magnesium, when these surfaces are exposed to solution a proportion of these ions may dissolve leaving a negatively charged site.

The third principle way in which surfaces may acquire charge is through isomorphic substitution. In this mechanism, an ion may be incorporated into the lattice that has a different valence than the surrounding structure. An example is the substitution of aluminum for a silicon atoms in the structure of kaolin clay which leads to a net negative charge.

In many materials, several mechanisms of surface charge may be operating simultaneously. Prediction of the surface charge, therefore, is difficult and experimental

techniques become necessary to characterize the surface. In the following sections the influence of surface charge on the structure of the surrounding solution and the interaction of surfaces will be discussed in more detail.

Electrical Double Layers

Well over 100 years ago Helmholtz modeled charged surfaces in aqueous solution as being neutralized by an equal number of oppositely charged ions (counter-ions), adsorbed to the interface. This description formed the basis for what is now called the electrical double layer. That is to say, one layer of charges at the interface being neutralized by a second layer of counter-ions in solution. With this description, electrical potential was suggested to drop linearly from the magnitude at the interface, ψ_0 , to zero at the midpoint of the counter-ion layer. Unfortunately, this description was not able to adequately describe many commonly observed colloidal properties, such as electrophoresis.

To overcome this discrepancy, Gouy [GOU10] and Chapman [CHA13] assumed, due to thermal energy of the counter-ions in the double layer, that not all of them would necessarily be adsorbed to the interface. Instead, there would likely be a concentration gradient near the surface. Under this assumption, the local concentration of counter-ions near the interface would be greater than in the bulk, whereas the local concentration of similarly charged ions (co-ions) would be depleted. If the ions are assumed to be point charges that do not interact with each other, then according to the principles of electrostatics the distribution of charge may be described by the Poisson-Boltzmann equation,

$$\frac{d^2\psi}{dx^2} = \frac{2Zen}{\epsilon_r\epsilon_0} \sinh\left(\frac{Ze\psi}{kT}\right) \quad (2-28)$$

where ψ is potential, x is distance from the interface, Z is counter-ion valence, e is the charge on an electron, n is the electrolyte number density, ϵ_r is the relative dielectric constant of the medium, ϵ_0 is the permittivity of free space, and kT is the product of Boltzmann's constant and absolute temperature. This relation, however, is only assumed to be valid starting at some distance away from the interface.

A more complete description of the electrical double layer was developed by Stern [STE24] and Grahame [GRA47]. The Stern-Grahame model utilizes concepts from both Helmholtz and Gouy-Chapman to describe the overall properties of the electrical double layer. However there is a primary difference in that the number of counter-ions adsorbed to the interface is assumed to be proportional to surface potential and bulk electrolyte concentration. A schematic illustration of the Stern-Grahame model of the electrical double layer is shown in Fig. 2-5. This figure indicates a net negatively charged surface that may be described by either a surface potential, ψ_0 , or surface charge, σ_0 . Due to adsorbed counter-ions, the potential drops from ψ_0 to ψ_δ according to

$$\psi_\delta = \frac{\sigma_0 \delta}{\epsilon_\delta \epsilon_0} \quad (2-29)$$

where δ is the radius of the adsorbed hydrated counter-ions, σ_0 is surface charge and ϵ_δ is the relative dielectric constant of the Stern layer. Note that this layer may also be referred to as the Grahame layer and associated potentials or charges are referred to by either Stern or Grahame as well as the outer Helmholtz potential (OHP).

To apply Eq. (2-29), the number of adsorbed counter-ions needs to be known as a function of surface potential and bulk electrolyte concentration. Using the formalism of Grahame, the Stern charge, σ_δ , which is nothing more than the difference in the number

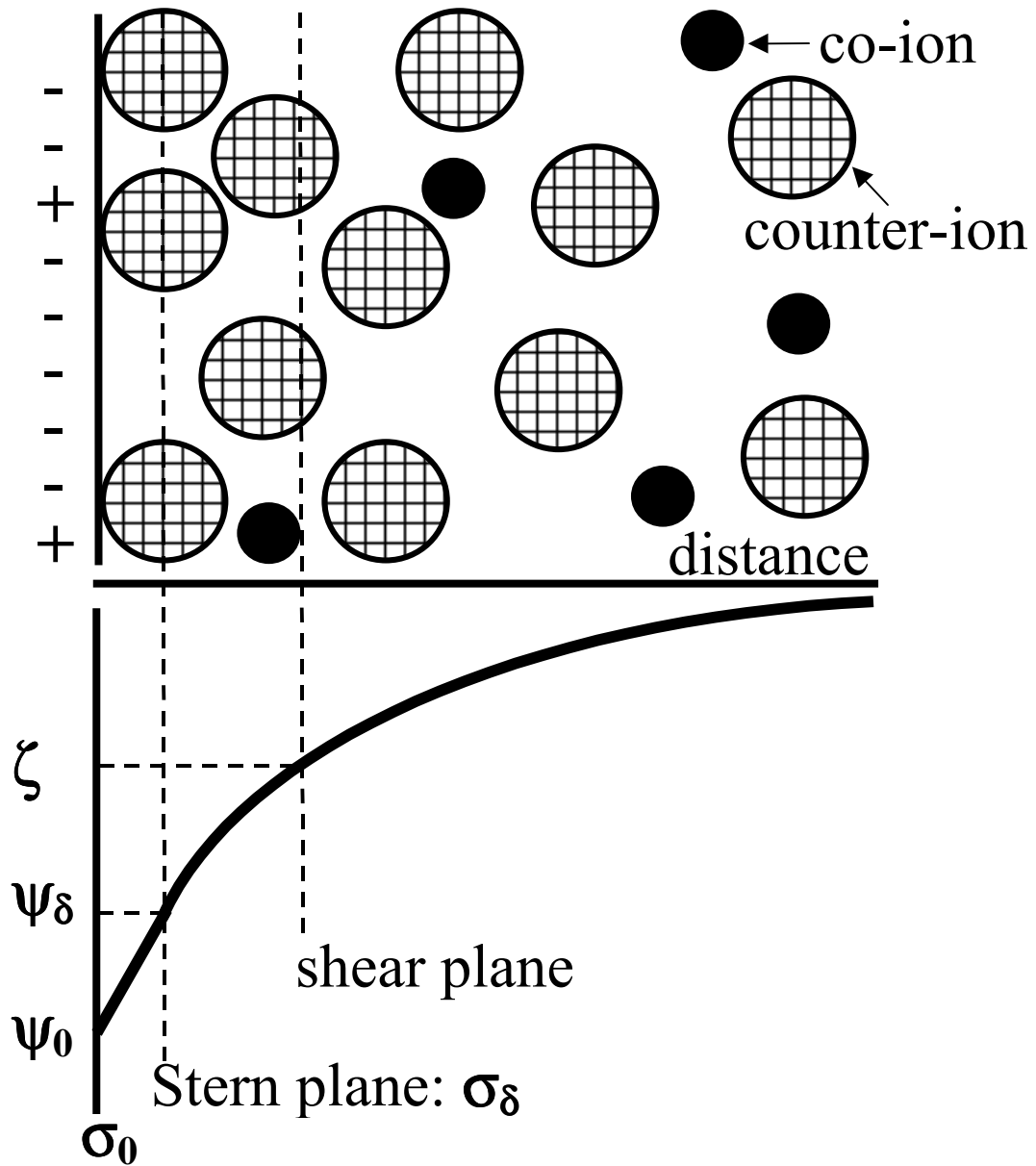


Figure 2-5: Schematic of the Stern-Grahame Electrical Double Layer. At a net negatively charged interface, cations (counter-ions: hatched) will adsorb in the Stern plane and accumulate near the surface while anions (co-ions: solid) will be depleted. At large distances from the surface the concentration of both counter and co-ions approaches the bulk concentration. This double layer structure leads to a linear decay of potential and charge across the Stern plane and a roughly exponential decay thereafter. The zeta potential, ζ , is measured at the shear plane.

of charge groups per unit area between the surface and Stern layer multiplied by the charge on an electron, may be written as the Grahame equation.

$$\sigma_{\delta} = \sqrt{8\epsilon_r \epsilon_0 n Z^2 kT} \sinh\left(\frac{Ze\psi_0}{2kT}\right) \quad (2-30)$$

Beyond distance δ the potential in the double layer decays according to Gouy-Chapman theory. Using an approximate solution, as outlined by Israelachvili [ISR92], the number density of ions at distance x from an interface, n_{xi} , may be written as

$$\sum_i n_{xi} = \sum_i n_i + \frac{\epsilon_r \epsilon_0}{2kT} \left(\frac{d\psi}{dx}\right)_x^2 \quad (2-31)$$

where n_i is the bulk number concentration of ionic specie i , ϵ_r is the relative dielectric constant of the medium, ϵ_0 is the permittivity of free space, k is Boltzmann's constant, T is absolute temperature, and ψ is potential at distance x . For a 1-1 electrolyte this expression simplifies to Eq. (2-32).

$$\frac{d\psi}{dx} = \sqrt{\frac{8kTn}{\epsilon_r \epsilon_0}} \sinh\left(\frac{e\psi}{2kT}\right) \quad (2-32)$$

This relation may then be integrated using the integral $\int \text{csch}(X) dX = \ln[\tanh(X/2)]$ to yield

$$\psi = \frac{2kT}{e} \ln \left[\frac{1 + \tanh\left(\frac{e\psi_{\delta}}{4kT}\right) e^{-\kappa x}}{1 - \tanh\left(\frac{e\psi_{\delta}}{4kT}\right) e^{-\kappa x}} \right] \approx \frac{4kT}{e} \tanh\left(\frac{e\psi_{\delta}}{4kT}\right) e^{-\kappa x} \quad (2-33)$$

where ψ_{δ} is the Stern potential and κ is the inverse Debye length. Note that for low potentials Eq. (2-33) reduces to the Debye-Hückel equation.

$$\psi = \psi_0 e^{-\kappa x} \quad (2-34)$$

These approaches have proven successful in describing the distribution of ions and potential emanating from a charged interface in aqueous solution and form the foundation for calculation of the electrostatic forces between two such interfaces.

However, most of the above relations are dependent on knowing the potential at the Stern plane. Through potentiometric techniques the adsorption of potential determining ions may be used to measure the charge developed at the interface under given ionic strength conditions. Unfortunately, these measurements are rather tedious and require the assumptions inherent in Eq. (2-29) to convert to the Stern potential. An alternative approach is to measure the potential on the particle directly. Zeta potential is such a technique.

Zeta Potential

When charged particles in colloidal suspension are exposed to an applied electric field they are attracted and diffuse toward the electrode of opposite charge in a process known as electrophoresis. This may seem unusual at first because the excess of counter-ions in the electrical double layer negates the charge on the surface and should result in a net neutral particle. However, the counter-ions are attracted to the electrode of similar charge to the particle. Hence, the propensity of a given counter-ion to move with the particle is a competition between the electrostatic attraction for the similarly charged electrode and hydrodynamic shear on the ion versus the attraction of that ion for the surface. The boundary at which the counter-ions cease to move with the particle is shown in Figure 2-1 as the shear plane. Since the structure of the double layer is disturbed at the shear plane, while electrophoresis is occurring, electrolyte concentration falls rapidly to that of the bulk and a potential difference between the shear surface and ground is created. In electrophoretic phenomena this potential is known as zeta potential, ζ . It should be noted that the position of the shear plane is usually quite small (0.4 nm) compared to the thickness of the double layer or Debye length ($\sim 1-30$ nm) [ATT00].

Smoluchowski [SMO21] treated this phenomena mathematically by equating the force of attraction due to the particle's interaction with the electric field with the resistance of the particle's movement through liquid due to Stokesian flow, Eq. (2-35),

$$F_{\text{hyd}} = 6\pi\eta Rv \quad (2-35)$$

where F_{hyd} is the force resisting the movement of a spherical particle radius, R , moving at velocity, v , through liquid of viscosity, η . Assuming that the extent of the electrical double layer is much smaller than the radius of the particle and that conduction within the shear plane is negligible, the velocity of the particle may be related to the zeta potential, ζ , and electric field strength, E , by

$$v = \frac{\epsilon_r \epsilon_0 \zeta}{\eta} E \quad (2-36)$$

where ϵ_r is the relative dielectric constant of the medium, ϵ_0 is the permittivity of free space and the electrophoretic mobility, μ_E , may be expressed as Eq. (2-37).

$$\mu_E = \frac{\epsilon_r \epsilon_0 \zeta}{\eta} \quad (2-37)$$

Note that these relations are independent of particle radius as both Stokesian movement and electrostatic attraction are proportional to radius. Additionally, although originally calculated for particles of zero dielectric constant the approach has been validated for particles of arbitrary dielectric constant and shape as reviewed by Hunter [HUN01]. For particles in the limiting case of a large double layer compared to particle radius, as may be the case for nanoparticles, Hückel [HÜC24] derived an expression similar to that of Smoluchowski,

$$v = \frac{2\epsilon_r \epsilon_0 \zeta}{3\eta} E(1 + \kappa R) \approx \frac{2\epsilon_r \epsilon_0 \zeta}{3\eta} E \quad (2-38)$$

where R is particle radius and κ is the inverse Debye Length. The discrepancy between these two cases was resolved by Henry [HEN31] who proposed an equation of the form

$$v = \frac{2\varepsilon_r \varepsilon_0 \zeta}{3\eta} E \cdot f_1(\kappa R) \quad (2-39)$$

where $f_1(\kappa R)$ is a function ranging from 1 in the Hückel limit of low κR to 3/2 in the Smoluchowski limit of high κR . Recently Oshima (OSH94) has proposed a single analytical formula for $f_1(\kappa R)$.

$$f_1(\kappa R) = 1 + \frac{1}{2} \left(1 + \frac{2.5 / (1 + 2e^{-\kappa R})}{\kappa R} \right)^{-3} \quad (2-40)$$

Due to the ions within the shear plane the zeta potential is always lower in magnitude than the Stern potential. However, for relatively low ionic strength conditions (approximately less than 0.03 M) and low surface potential (approximately less than 30 mV) the zeta potential may be considered a good approximation of the Stern potential. For electrolyte concentrations and potentials where this approximation is not valid, there are several methods to calculate the Stern potential based on the distribution of ions between the shear and Stern planes [ATT00]. However, to more accurately characterize the interaction of surfaces direct measurement of electrostatic force, which depends primarily on the Stern potential and ionic strength, may be necessary.

Boundary Conditions for Calculation of Electrostatic Force

When two electrical double layers of similar charge begin to overlap, electrostatic repulsion results. If these surfaces are opposite in charge, they will attract. In the above sections, surfaces were considered to be isolated. However, when surfaces approach one another the increased electric field strength and higher concentration of counter and potential determining ions may affect the charge on the surfaces. Hence, before electrostatic forces may be calculated a brief description of how the surfaces behave in the presence of each other is necessary.

There are two boundary conditions that act as upper and lower limits to the electrostatic force magnitude. Under a constant potential boundary condition, the surface charge decays from its value at infinite separation distance to zero as the two surfaces approach. In more descriptive terminology, this implies that as the two electrical double layers overlap the local concentration of both counter-ions and potential determining ions increases. Especially for materials that acquire charge by the selective dissolution mechanism this higher concentration of ions tends to reduce the surface charge. At small separation distances this effect becomes more pronounced due to the exponential nature of the ion concentration profile at an interface. Because the charge is reduced at any given separation distance using this approach, this boundary provides the lower magnitude limit of electrostatic force.

The boundary condition that predicts the maximum repulsion between surfaces is referred to as constant charge. Under this assumption, as surfaces approach no change in surface charge occurs. Hence, at small separation distances surface potential must approach zero. Physically, this indicates that the electrolyte concentration between the surfaces must increase more strongly than in the constant potential case in order to compensate the charge. Surfaces that acquire charge through dissociation are more likely to approach the constant charge limit as the concentration of counter-ions does relatively little to change the surface charge.

Unfortunately, real surfaces cannot be characterized as constant potential or constant charge. Instead both processes are likely to occur to some degree. To model the true behavior of surfaces, a charge regulation boundary condition may be employed. Under this assumption, reactions that account for both the dissociation of surface groups

and the binding of counter-ions to the interface are proposed. These reactions must depend on the local concentrations of counter and potential determining ions.

Additionally, for a given concentration of counter and potential determining ions, the total number of each type of site should be known.

Even for a relatively simple single site solid such as silica or mica this means that four additional variables need to be considered when predicting the interaction force profile. For an amphoteric surface such as alumina the relations become significantly more complicated. Such constants are usually obtained experimentally by fitting directly measured forces between surfaces. Solving for the unknown charge regulation parameters (as well as Stern potential and Hamaker constants) is difficult and requires measurement over a wide range of solution conditions. Hence, determination of the charge regulation parameters has only been attempted for a few materials such as mica [PAS82] and silica [GRA93, ZHU00].

It should be noted, however, that the practical effects of charge regulation processes only come into effect at relatively short separation distances (less than 30 nm). In fact for larger separation distances, the two limiting conditions approach one another and a single analytical expression may be used. However, as ensemble models are refined and processing conditions become more severe, more detailed knowledge of the behavior of particles at small separation distances will become necessary.

The variation in surface charge or potential as interfaces approach is important because these boundary conditions allow the Poisson-Boltzmann distribution for overlapping electrical double layers to be solved and electrostatic forces calculated. In the following two sections these conditions will be utilized to derive electrostatic force under

the linearized Poisson-Boltzmann approximation, which is generally valid for lower potentials and larger separation distances, as well as the full solution.

Linearized Poisson-Boltzmann Approach

To calculate the electrostatic force between surfaces, the full solution to the Poisson-Boltzmann equation must be performed numerically. However, in order to develop an analytical model, a linear approximation may be employed. If the scaled potential, $y(\xi)$, between two plates is represented as

$$y(\xi) = \frac{Ze}{kT} \psi \quad (2-41)$$

where Z is counter-ion valence, e is the charge on an electron, kT is the product of Boltzmann's constant and absolute temperature, ψ_δ is the Stern potential, and ξ is a dimensionless scaled length parameter,

$$\xi = \kappa x \quad (2-42)$$

where κ is the inverse Debye length and x is distance perpendicular to the interface. The Poisson-Boltzmann equation, Eq. (2-28) may be written as Eq. (2-43).

$$\frac{d^2 y(\xi)}{d\xi^2} = \sinh y(\xi) \quad (2-43)$$

Expanding the right side of Eq. (2-43) in a power series of $y(\xi)$ yields the following.

$$\frac{d^2 y(\xi)}{d\xi^2} = y(\xi) + \frac{y(\xi)^3}{6} + \frac{y(\xi)^5}{120} + \dots \quad (2-45)$$

If only the first term on the right side of the equation is considered to adequately describe the Poisson-Boltzmann distribution then it becomes possible to analytically solve for the electrostatic repulsive energy between two flat surfaces. For constant potential surfaces, these calculations were performed by Hogg et al. and the resultant equation is often referred to as the Hogg-Healy-Fuerstenau (HHF) equation [HOG66].

$$W_{\psi}(H)_{\text{plt/plt}} = 2Z^2nkT \left(\frac{e\psi_{\delta}}{kT} \right)^2 \frac{1}{\kappa} \left(1 - \tanh \frac{\kappa H}{2} \right) \quad (2-46)$$

$W_{\psi}(H)_{\text{plt/plt}}$ is the energy of interaction between flat plates under a constant potential boundary condition, Z is counter-ion valance, n is the number density of counter-ions, e is the charge on an electron, ψ_{δ} is the Stern potential, k is Boltzman's constant, T is absolute temperature, κ is the inverse Debye length, and H is the distance between the two surfaces. Similarly, the interaction energy between flat plates under a constant charge boundary condition, $W_{\sigma}(H)_{\text{plt/plt}}$, may be written as Eq. (2-47).

$$W_{\sigma}(H)_{\text{plt/plt}} = 2Z^2nkT \left(\frac{e\psi_{\delta}}{kT} \right)^2 \frac{1}{\kappa} \left(\coth \frac{\kappa H}{2} - 1 \right) \quad (2-47)$$

As mentioned earlier, at low potentials (generally less than 30 mV), low ionic strength (generally less than .03 M), and small degrees of double layer overlap (generally H greater than 30 nm), the constant charge and potential boundary conditions begin to coincide. Under these conditions the surface charge, σ_0 , may be related to the surface potential, ψ_0 , which is also equivalent to the Stern potential,

$$\sigma_0 = \epsilon_r \epsilon_0 \kappa \psi_0 \quad (2-48)$$

and where the electrostatic interaction between flat plates may be written as, Eq. (2-49).

$$W_{\psi}(H)_{\text{plt/plt}} = W_{\sigma}(H)_{\text{plt/plt}} = 2\epsilon_r \epsilon_0 \kappa \psi_0^2 e^{-\kappa H} = \frac{2\sigma_0^2}{\epsilon_r \epsilon_0 \kappa} e^{-\kappa H} \quad (2-49)$$

To extend the range of applicability of Eqs. (2-46) and (2-47) especially to higher potentials and shorter separation distances as well as account for the interaction of dissimilar surfaces, some authors have extended the power series approximation, Eq. (2-45) to the second and third terms [OSH82]. While immensely useful because the solutions retain the form of analytical equation, they are very long, over 50 terms, and still fail to accurately describe the electrostatic force at potentials greater than approximately 60 mV, especially at short separation distances. Since the principal

discussion in this study is the interaction at relatively small separation distances, electrostatic force calculation based on the full numerical solution to the Poisson-Boltzmann distribution is more appropriate.

Non-Linear Approach

The full non-linear solution to the Poisson-Boltzmann equation must be performed to accurately predict the electrostatic interaction of surfaces at high surface potentials or short separation distances. Chan et al. [CHA80] using such an approach have developed as relatively simple algorithm for these calculations. If the Poisson-Boltzmann equation, Eq. (2-28) is written in terms of the scaled potential, y , defined by Eq. (2-41) to yield Eq. (2-43) a first integration may be written as

$$\frac{dy}{d\xi} = QSgn(y_m) \quad (2-50)$$

where $Sgn(y_m)$ indicates the sign of the potential at the midpoint between the surfaces and Q is the following.

$$Q = \sqrt{2(\cosh y - \cosh y_m)} \quad (2-51)$$

Note also that at the midpoint between the surfaces, $\xi = 0$, $dy/d\xi$ must be zero and hence, $Q = 0$. With this boundary condition dQ/dy may be calculated as the following.

$$\frac{dQ}{dy} = \frac{\sinh y}{Q} = \frac{Sgn(y_m)}{Q} \sqrt{\left(\frac{Q^2}{2} + \cosh y_m\right)^2 - 1} \quad (2-52)$$

From Eqs. (2-50) and (2-52) it is now possible to derive $d\xi/dQ$, Eq. (2-53).

$$\frac{d\xi}{dQ} = \sqrt{\left(\frac{Q^2}{2} + \cosh y_m\right)^2 - 1} \quad (2-53)$$

If at the midpoint between the surfaces $Q = 0$ and $\xi = 0$, and at the interface $Q = Q_\delta$ and $\xi_\delta = \kappa H/2$ where κ is the inverse Debye length and H is separation distance, then

for selected a value of the midplane potential, y_m , numerical integration from $Q = 0$ to Q_δ will yield a specific value of ξ_δ . Repeating this procedure for $y_m = 0$, or a suitably low potential, to $y_m = y_\delta$ will the define a set of corresponding values for separation distances and midplane potentials. The electrostatic force per unit area, $F_{\text{plt/plt}}$, may be written as a function of midplane potential as

$$F_{\text{plt/plt}} = 2nkT(\cosh y_m - 1) \quad (2-54)$$

where n is the number density of counter-ions and kT is the product of Boltzmann's constant and absolute temperature. The interaction energy between plates may then be calculated by a second numerical integration represented by Eq. (2-55).

$$W_{\text{plt/plt}} = \int_H^\infty F(H)_{\text{plt/plt}} dH \quad (2-55)$$

The above equations were derived under the assumption of a constant surface potential, y_δ , which yields a constant value of Q_δ at any separation distance. Hence, Q_δ has the same form as Q , Eq. (2-51).

$$Q_\delta = \sqrt{2(\cosh y_\delta - \cosh y_m)} \quad (2-56)$$

However, for a constant charge boundary condition the integration limit Q_δ must be determined in terms of charge, σ_δ . By definition at the interface

$$\frac{dy}{d\xi} = \frac{4\pi e}{\epsilon_r \epsilon_0 kT} \frac{1}{\kappa} \sigma_\delta \quad (2-57)$$

which is equivalent to Eq. (2-50). Therefore, the integration limit may be written as Eq. (2-58).

$$Q_\delta = \frac{4\pi e}{\epsilon_r \epsilon_0 kT} \frac{1}{\kappa} |\sigma_\delta| \quad (2-58)$$

Although the mathematical description of the electrical double layer and the calculation of electrostatic force is extensive, there are still many assumptions assumed in the basic theory. As delineated by Lyklema [LYK95]:

- i) Ions are assumed to be point charges.
- ii) Non-Coulombic (specific) adsorption between counter-ions and co-ions and the surface is neglected.
- iii) Permittivity of the medium is assumed to be a constant and independent of electrolyte concentration.
- iv) Incomplete dissociation of the electrolyte is ignored.
- v) Solvent is considered to be homogeneous.
- vi) Polarization of the solvent is not accounted for.
- vii) Surface charge is assumed to be smeared out and uniform.
- viii) Image forces between ions and the surface are neglected.
- ix) Average potential and potential of the mean force are assumed to be equal.
- x) Surfaces interact in an infinite volume of solution.
- xi) Surfaces are considered ideally smooth.

For most interactions these assumptions are not violated to a significant degree. However, for interactions in which separation distance is small or ionic strength is high, models which account for some of these issues may need to be developed. Specific examples include, if hydrated ions are sufficiently large and in large enough concentration they may physically resist surfaces from approaching each other [PAS83]. These hydration forces violate the description of ions as point charges. Similarly, for highly charged interfaces in solutions of relatively high ionic strength, the permittivity of the medium may be altered, and could continue to change as a function of separation distance [NIN97]. Under similar conditions, image forces have been suspected to increase the viscosity of concentrated suspensions [COL98].

DLVO and Extended DLVO Theory

The teams of Derjaguin and Landau in Russia [DER41] as well as Verwey and Overbeek [VER48] in the Netherlands independently developed the fundamental criteria for colloidal stability known as DLVO theory. Quite simply, both groups came to the conclusion that the stability of similar particles in suspension was a competition between van der Waals attraction and electrostatic repulsion. This may be expressed as the total energy, W_{tot} , of interaction being equal to the sum of van der Waals attractive energy, W_{vdW} , and electrostatic repulsive energy, W_{elect} , as expressed in Eq. (2-59).

$$W_{\text{tot}} = W_{\text{elect}} - W_{\text{vdW}} \quad (2-59)$$

This seemingly simple relation has proven extremely powerful in predicting the behavior of nearly ideal particulates and surfaces in solution and has been validated for a wide variety of conditions and surfaces. Israelachvili [ISR92], Lyklema [LYK95], and Hunter [HUN01] have reviewed many of the successful applications of DLVO theory.

There are a number examples, however, where DLVO theory does not adequately describe measured interaction force profiles. These may range from the relatively complicated, as in examples where the increased concentration of ions in the double layer aids in the screening of van der Waals attraction such that the two quantities are not independent [NIN97], to more obvious situations where another mechanism of force is active. For example, if in a good solvent a polymeric reagent (non-ionic) is adsorbed to the surfaces, a strong steric repulsive force may be observed due to the physical and osmotic pressure developed by the overlap of soluble polymer chains. However, too much free polymer in solution, when excluded from the gap between surfaces, may cause an attractive depletion force, due to osmotic pressure. Additionally, hydration and other solvation forces arise due to the structuring of hydrated ions or solvent, respectively, in

the gap between surfaces. Alternatively, attraction may occur due to the unfavorable structure of water near a hydrophobic interface. It has become common practice to also assume that, as a first approximation, these other force mechanisms are also independent and additive. Hence, extended DLVO theory may be written as Eq. (2-60).

$$W_{\text{tot}} = W_{\text{elect}} - W_{\text{vdW}} + W_{\text{steric}} - W_{\text{depletion}} + W_{\text{hydration}} + W_{\text{solvation}} - W_{\text{hydrophobic}} + W_{\text{other}} \quad (2-60)$$

Certainly not all of these forces can occur simultaneously or are strictly independent of each other. Many also have different magnitudes and signs such that as a function of separation distance different forces may become dominant. Delineation of these forces, their interactions, and fundamental mechanisms is currently being actively pursued. However, in this study conditions and materials are avoided where these additional forces are expected to have significant impact. Hence, they will not be discussed in detail here.

Surface Force Summary

The previous sections have described in some detail the basic concepts of attraction and repulsion between surfaces under gaseous atmospheric conditions and in a solvent. Although these models are not necessarily complete, they do provide a sound theoretical basis for the fundamental interaction of surfaces. However, in all the above models, the interfaces in contact are assumed to be ideal (smooth and discrete). In the remainder of this study, these basic concepts will be extended for two specific types of non-idealities. Namely, surface roughness and chemically impure surfaces. Emphasis will be placed on the nanoscale characterization of these interfaces and impact of these deviations on ensemble behavior of particulate systems.

CHAPTER 3 ROLE OF ASPERITY GEOMETRY ON THE ADHESION OF SURFACES

Introduction

As discussed in the previous chapter, there are a wide variety of theoretical approaches to describe the adhesion between surfaces in a gaseous medium. These theories are based on the assumption that the geometry of the interacting bodies is known and that they may be treated at the macroscopic level. This precludes the discussion of interfaces on which nanoscale roughness or a transition in composition exists. This is unrealistic because every surface due to the physical size of atoms or crystal structure exhibits some order of roughness. Similarly, there are very few materials that do not form some sort of discontinuous layer, such as an oxide, at the interface. The question then arises as to how significant are these non-idealities in determining the overall interaction between surfaces. In this chapter, a description of one type of non-ideal surface, a surface on which roughness at the nanoscale is present, will be developed. Through an analysis of such a surface, models of the interaction force of adhesion between two interfaces will be developed. This concept will be further validated and expanded in Chapters 4 and 5.

Most particulate surfaces, regardless of preparation method, possess some finite surface roughness. For many modern materials, particularly in the microelectronics industry, highly polished surfaces with roughness on the nanometer scale are becoming increasingly common. Particulate adhesion to these surfaces is of critical importance due to the possibility of defects caused by small imperfections. Hence, to develop enhanced

cleaning procedures, the strength of adhesion between particles and the substrate needs to be determined. The existence of nanoscale roughness is known to dramatically reduce adhesion between surfaces due to a decrease in the real area in contact and an increase in the distance between the bulk surfaces [TAB77, BRI92, KRU67, JOH71, MIZ96]. However, the magnitude of these effects is less well understood.

Quantitative calculation of adhesion force was performed by Iida et al. [IID93] by modeling the interaction between a smooth glass particle and glass substrate possessing roughness ranging from 50 - 400 nm. In this investigation, adhesion force was estimated by the average force needed to retain 50% of particles on a substrate after bombardment by fluid or gas. A factor of ten decrease in adhesion force was initially observed as roughness increased but was then followed by a region of more gradually decreasing adhesion force. However, in developing a theoretical model, these investigators only considered the interaction between the particles and asperities (contact forces) and ignored the contribution arising from the interaction of the particles with the underlying surface (non-contact forces). Due to the proximity of the surface at lower root mean square (RMS) roughness, this omission resulted in underestimated adhesion forces.

One of the most commonly used models of adhesion force in the nanoscale roughness regime is Rumpf's model [RUM90], which is based on contact of a single hemispherical asperity, centered at the surface and interacting with a much larger spherical particle along a line normal to the surface connecting their centers, as shown schematically in Figure 3-1. The model consists of two terms that describe the total van der Waals interaction. The first represents the interaction of the adhering particle in

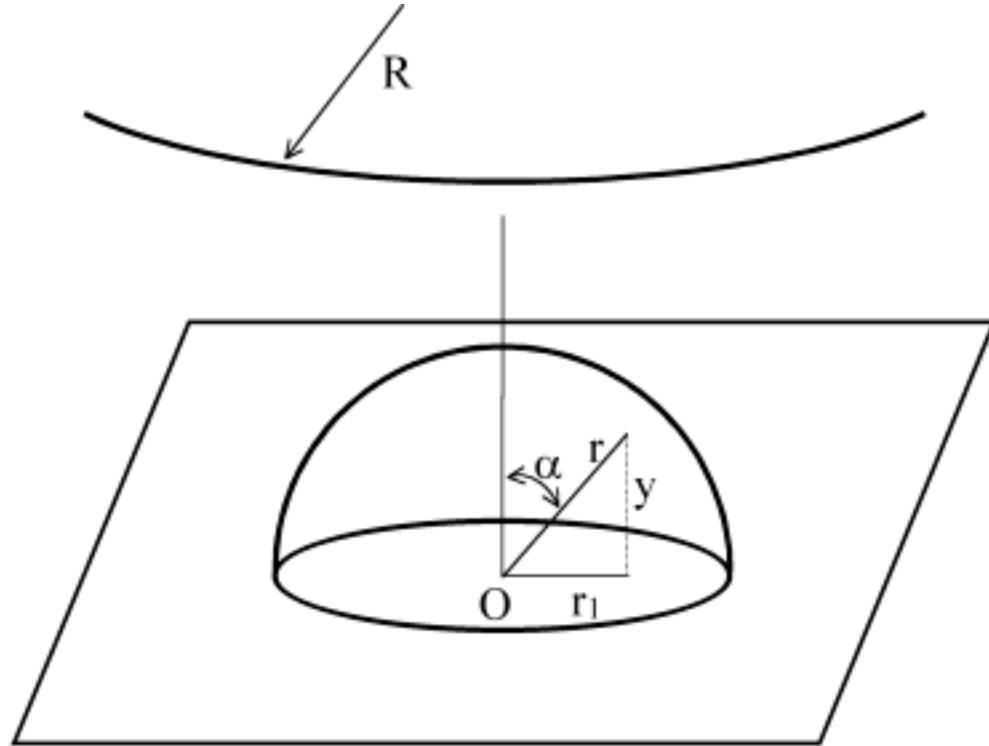


Figure 3-1: Asperity Schematic Using the Rumpf Model. Illustration of the geometry proposed by Rumpf [RUM90] for the interaction of an adhering particle with a rough surface. Diagram depicts a hemispherical asperity of radius r and origin at the surface interacting along the ordinate axis with a spherical adhering particle.

contact with the asperity, while the second describes the “non-contact” force between the adhering particle and flat surface separated by the height (radius) of the asperity.

Applying Derjaguin’s approximation [DER34] for both interactions, Rumpf obtained the following formula.

$$F_{\text{ad}} = \frac{A}{6H_0^2} \left[\frac{rR}{r+R} + \frac{R}{(1+r/H_0)^2} \right] \quad (3-1)$$

Where A is the Hamaker constant, R and r are the radii of the adhering particle and asperity, respectively, and H_0 is the distance of closest approach between surfaces (approximately 0.3 nm). A primary limitation of this model is that the center of the hemispherical asperity is required to be at the surface. As described in detail later, in real

systems, especially those with low roughness, this assumption may not accurately describe the surface asperities.

Greenwood and Williamson [GRE66] introduced a roughness model considering hemispherical asperities of equal radii, but whose origin was offset from the average surface plane according to Gaussian probability. However, as Fuller and Tabor surmised [FUL75], the application of a Gaussian distribution to model asperities on a surface may produce errors because large asperities significantly affect the interaction even though their number may be low or even singular. Czarnecki and Dabros [CZA80] modeled particles with surface roughness as spherical cores with a rough outer shell. They then proposed a correction factor, based on asperity height, to predict the van der Waals attractive force. This approach is valid only for separation distances much larger than the asperity height. Therefore, it is only applicable for non-contact dispersion forces and not adhesion force.

Recently, Xie [XIE97] also carried out a theoretical study to determine the effect of surface roughness on adhesion. A modified van der Waals force depending only on the radius of asperities was proposed and applied through two geometrical models. The first model is similar to Rumpf's but ignored the interaction of the particle with the asperity on the surface. The second assumes the asperity to be a small particle positioned between the two larger surfaces (sandwich model). It was concluded that if the radii of surface asperities are smaller than 10 nm, the surface could be treated as smooth.

The investigations described above propose methodologies to predict adhesion force between surfaces of known asperity geometry. Unfortunately, little has been said about how well those geometries correlate with known surface roughness profiles,

especially at the nanoscale. In this chapter, a more realistic model of surface roughness will be developed and the effect on adhesion force explored through parametric investigation. Chapter 4 will focus on the application of this model to predict the adhesion force between surfaces with nanoscale roughness. Chapter 5 will extend the application of this basic approach to the interaction of surfaces in a humid environment where capillary adhesion forces may become significant.

Modified Rumpf Model

A schematic of the Rumpf model is shown in Figure 3-1. This model and Eq. (3-1) were proposed by Rumpf to calculate the force of adhesion between a spherical particle and spherical surface asperity [RUM90]. The radius of the asperity, r , however, is not easily measured, while the value of RMS (root mean square) roughness is. Hence, in order to apply the Rumpf model, a relationship between the radius of the asperity and RMS roughness must be developed.

Considering a spherical coordinate system, with the origin at the center of the spherical asperity, the horizontal projection, r_1 , of any radii of the asperity, r , at angle, α , formed between any radii and vertical axis, may be related to r and α as follows:

$$r_1 = r \cdot \cos \alpha \quad (3-2)$$

Similarly, the vertical distance to the average surface plane, y , may be written as

$$y = r \cdot \sin \alpha \quad (3-3)$$

The general definition of RMS for hemi-spherical asperities is

$$\text{RMS} = \sqrt{\frac{32 \int_0^r y^2 r_1 dr_1}{\lambda^2}} k_p \quad (3-4)$$

where $\lambda = 4r$ is the peak-to-peak distance and k_p is the surface packing density for close packed spheres, 0.907. Note that a negative deviation from the average plane in term of RMS roughness is equivalent to an asperity. Hence, as long as it is assumed that the surface contains an equal number of asperities and inverse asperities (pits) the close packing assumption is valid. Substituting Eqs. (3-2) and (3-3) in (3-4) and integrating, the following equations are obtained.

$$\text{RMS} = 0.673r \quad (3-5)$$

or

$$r = 1.485 \cdot \text{RMS} \quad (3-6)$$

Using this approach, the adhesion force predicted by the Rumpf model may be calculated by a simple substitution of Eq. (3-6) into Eq. (3-1) yielding the following.

$$F_{\text{ad}} = \frac{AR}{6H_0^2} \left[\frac{1}{1 + R/(1.48 \cdot \text{RMS})} + \frac{1}{(1 + 1.48 \cdot \text{RMS}/H_0)^2} \right] \quad (3-7)$$

Adhesion force calculated using Eq. (3-7) will be termed the modified Rumpf model in the remainder of the study.

Figure 3-2 depicts the variation of the total adhesion force between a 10 μm particle and a rough surface normalized by the radius of curvature of the adhering particle as predicted by the modified Rumpf model. In the limit of both very small and very large surface roughness the predicted adhesion force approaches that of a sphere and smooth flat plate (185 mN/m). Note that when normalized by the radius of curvature this limiting value is independent of the size of the adhering particle. In the nanoscale roughness regime a dramatic decrease in adhesion force is predicted for micron sized adhering particles. To elucidate the mechanisms responsible for this decrease, the contact (particle/asperity) and non-contact (particle/surface) components of the total adhesion

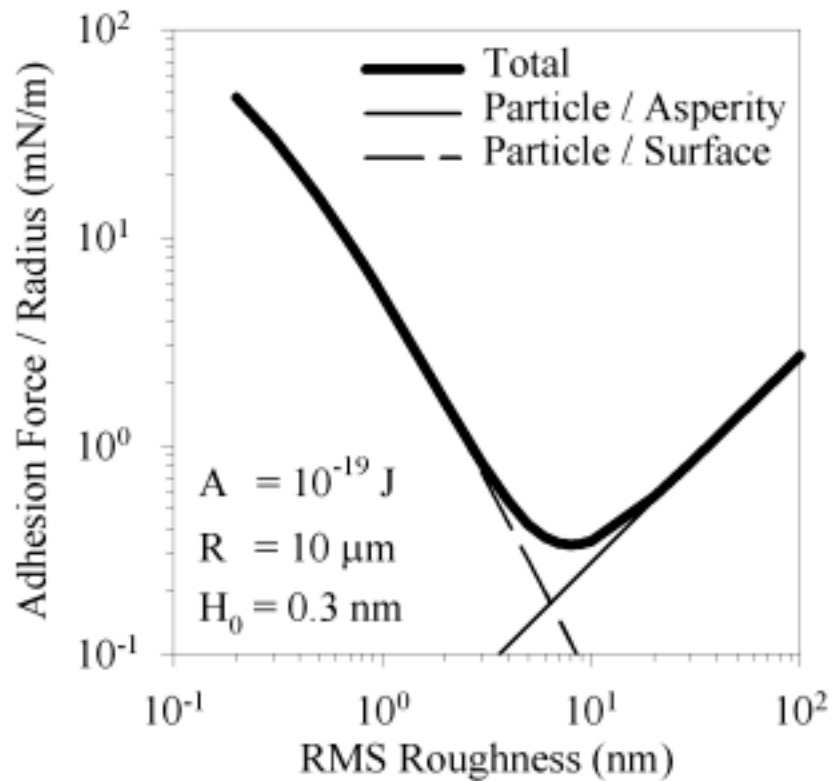


Figure 3-2: Prediction of Adhesion Using the Rumpf Model. Prediction of the total, contact, and non-contact force of adhesion, normalized by the radius of the adhering particle, between a $10\ \mu\text{m}$ smooth sphere and a surface with nanoscale roughness using the modified Rumpf model, Eq. (3-7). Hamaker constant, A , is $10^{-19}\ \text{J}$ and distance of closest approach, H_0 , is $0.3\ \text{nm}$.

force are also plotted in Figure 3-2. At larger RMS roughness, the contact adhesion force between the sphere and asperity is seen to dominate the interaction. However, as the radius of the asperity and hence roughness decreases, the non-contact adhesion force primarily contributes to the interaction.

It should be noted that even though the scale of adhesion force is normalized by the radius of curvature of the adhering particle, in the area of nanoscale roughness this

normalization is not entirely accurate. As expected in this model, the non-contact force is independent of particle size but the contact adhesion force between the particle and asperity is not. As the particle size increases, the normalized force of adhesion in the regime affected by nanoscale roughness decreases. This results in a shift in the contact component towards higher RMS roughness as particle size increases. Hence, the minimum in the total adhesion force, as predicted by this theory, further decreases in magnitude and occurs at greater roughness values as the size of the adhering particle increases.

Proposed Model

Techniques such as atomic force microscopy have enabled detailed investigation of the morphology of surfaces with small roughness. Through these investigations it has been determined that the geometry of the Rumpf model does not accurately describe the surface in the nanoscale regime. More realistically, one can imagine that as the surface roughness decreases, the radius of the asperity must really increase. Hence, as the surface roughness approaches zero the radius of the asperity should approach infinity resulting locally in a flat surface. For this situation to be valid, if the asperity is still modeled as a sphere, the center of the asperity can not be at the surface. Instead the center must be located some distance below the surface such that the observed asperity height is equivalent to the radius in the Rumpf geometric model. In the proposed model of the geometry of the surface roughness, a new parameter is introduced. Not only should the height of the asperity used but its breadth must also be considered.

Figure 3-3 depicts surface roughness as close-packed hemispherical asperity caps and troughs. As in the Rumpf model a single particle interacting with a single asperity

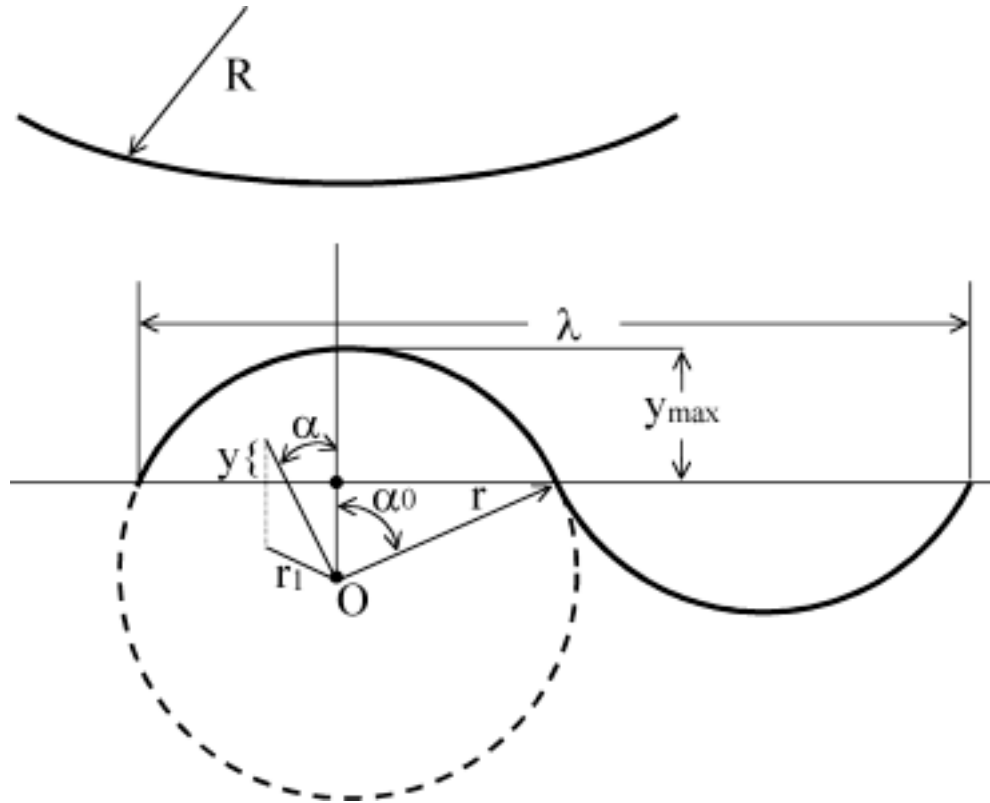


Figure 3-3: Asperity Schematic Using the Proposed Model. Illustration of the geometric model used to calculate adhesion force between a spherical adhering particle and a surface in the proposed model. Diagram depicts a hemispherical asperity of radius r , peak-to-peak distance λ , and origin below the average surface interacting along the vertical axis with a spherical adhering particle.

along a line connecting their centers and perpendicular to an average surface plane will be considered. However, the asperity will be characterized by radius, r , and peak-to-peak distance, λ . Note that in this model the height of the asperity, above the average surface plane, is not equal to the radius of the asperity. The origin of the asperity, O , is located below the average surface plane and is coincident with a spherical coordinate system.

As before, if α is defined to be any angle between the vertical direction and a radius of the asperity, r , that terminates above the average surface plane, the projection, r_1 , on a horizontal plane is the following.

$$r_1 = r \cdot \sin \alpha \quad (3-8)$$

The maximum value of the angle, α_0 , is limited to the intersection of the sphere describing the asperity and the average surface plane, $\alpha_0 = \arcsin(\lambda/4r)$. Hence, the vertical distance between any point on the asperity and the horizontal plane may be written as

$$y = r(\cos \alpha - \cos \alpha_0) \quad (3-9)$$

For small angles, α and $\alpha_0 \ll 1$, as is the case for nanoscale roughness, Eqs. (3-8) and (3-9) may be simplified, as follows

$$r_1 = r\alpha \quad (3-10)$$

and

$$y = (r/2)(\alpha_0^2 - \alpha^2) \quad (3-11)$$

where $\alpha_0 = \lambda/4r$, and hence $\alpha_0 \ll 1$, and $\lambda \ll 4r$ where all angles are in radians.

The radius of the asperity and the maximum value of the peak height, y_{\max} , are not measured parameters and should be expressed as a function of RMS roughness and peak-to-peak distance, λ , through a geometric model of the roughness profile. For the geometry defined above, the value of the peak height, y_{\max} , can be obtained from

$$y_{\max} = \frac{r\alpha_0^2}{2} = \frac{\lambda^2}{32r} \quad (3-12)$$

Introducing a relationship between y_{\max} and RMS where k_1 is a coefficient

$$y_{\max} = k_1 \text{RMS} \quad (3-13)$$

and substituting in Eq. (3-12), Eq. (3-14) is obtained.

$$r = \frac{\lambda^2}{32k_1 \text{RMS}} \quad (3-14)$$

Once again applying the general definition of RMS roughness for close packed hemispherical asperity caps or troughs

$$\text{RMS} = \sqrt{\frac{32 \int_0^{\lambda/4} y^2 r_1 dr_1}{\lambda^2}} k_p \quad (3-15)$$

and substituting Eqs. (3-10) and (3-11) in (3-15), Eq. (3-16) is obtained.

$$\text{RMS} = 0.0172 \lambda^2 / r \quad (3-16)$$

Note that if Eq. (3-16) is combined with the restriction $\lambda \ll 4r$, the following condition is imposed.

$$\text{RMS} \ll \lambda / 14.5 \quad (3-17)$$

This condition indicates that the proposed adhesion model is valid only for surfaces with small asperity amplitude and large peak-to-peak distances (not a high aspect ratio or jagged surface). At first, this restriction may seem to severely limit the systems to which this model is applicable. However, as discussed in Chapter 4, the roughness on the nanoscale is found to control the theoretical adhesion between surfaces. Even for surfaces with larger RMS roughness, it is the nanoscale asperities often found on larger asperities that dominate the adhesion interaction. Hence, the proposed model may be extended for many types of surfaces with greater RMS roughness if multiple scales of roughness are considered.

Using Eqs. (3-14) and (3-16), allows the coefficient relating RMS roughness and the maximum peak height to be determined as,

$$k_1 = 1.817 \quad (3-18)$$

To calculate the adhesion force in the framework of this model, we can use the following equation by considering the contact and non-contact van der Waals forces, similar to the method proposed by Rumpf [RUM90].

$$F_{\text{ad}} = \frac{AR}{6H_0^2} \left[\frac{r}{r+R} + \frac{1}{\left(1 + \frac{y_{\text{max}}}{H_0}\right)^2} \right] \quad (3-19)$$

Note that Eq. (3-19) becomes Eq. (3-1) when the origin of the spherical asperity is coincident with the average surface plane (i.e. when $\lambda = 4r$ and $y_{\text{max}} = r$). Substituting Eqs. (3-13) and (3-14) for y_{max} and r in Eq. (3-19), the adhesion force between an adhering particle and a surface with nanoscale roughness is the following.

$$F_{\text{ad}} = \frac{AR}{6H_0^2} \left[\frac{1}{1 + \left(\frac{32Rk_1\text{RMS}}{\lambda^2}\right)} + \frac{1}{\left(1 + \frac{k_1\text{RMS}}{H_0}\right)^2} \right] \quad (3-20)$$

The first terms in brackets of Eqs. (3-19) and (3-20) represent the contact interaction of an adhering spherical particle with an asperity on the surface. The second terms account for the non-contact interaction of adhering particle with the average surface plane.

It should be noted that Eqs. (3-19) and (3-20) only account for the van der Waals attraction between surfaces. However, as described in Chapter 2, it is known that other forces, such as polar forces [ISR92], may significantly contribute to the adhesion between contacting surfaces. Furthermore, the proposed models also do not consider elastic deformation of the surfaces. As a result, the proposed model may underestimate

adhesion. To account for any additional attractive forces and possible elastic deformation upon detachment from the surface, adhesion force is often calculated through models considering surface energy such as the Johnson-Kendall-Roberts [JOH71] or Derjaguin-Muller-Toporov [DER75] models. The application of these models to the proposed geometries is discussed further in Chapter 4.

Another assumption inherent in the proposed model and in Rumpf's original work is that the region outside the contacting asperity may be approximated by a smooth flat plane. To justify this approximation, the series approximation to the ratio of non-contact van der Waals attraction between rough planes and smooth planes may be considered [BRE74, RAB89].

$$U_{\text{rough}} / U_{\text{smooth}} = 1 + \frac{3(\text{RMS}_1^2 + \text{RMS}_2^2)}{H^2} + \frac{5(\text{RMS}_1 + \text{RMS}_2)^4}{H^4} \quad (3-21)$$

U_{rough} and U_{smooth} are the specific van der Waals energy of interaction between two rough or smooth planes, respectively. H is the separation distance between the surfaces or average surface planes. RMS_1 and RMS_2 are root mean square roughness of the first and the second interacting planes of the rough surfaces. Although this relation was originally derived for surfaces far from contact ($H \gg \text{RMS}_1$ or RMS_2), within this study it is applied at a separation distance corresponding to the asperity height, y_{max} , as related to RMS_1 through Eqs. (3-13) and (3-18). Additionally, the energy between planes may be related to the force through the Derjaguin approximation for a smooth adhering sphere ($\text{RMS}_2=0$). At contact the ratio becomes independent of RMS_1 , and approaches a value of approximately 2.4.

Although this ratio is greater than unity, it should be noted, that it includes the contribution of the central (contacting) asperity on the plane, which is excluded from the

second terms in Eqs. (3-19) and (3-20). More important is the fact that the overall contribution of the plane is significantly less than the contribution of the contact interaction between the surfaces. For example, even at extremely small RMS roughness, where the contact and non-contact terms are closest in magnitude, the non-contact term is only half the particle/asperity contribution. Above 2 nm RMS roughness, in some cases, it may even be appropriate to ignore the non-contact interaction between the particle and the average surface plane.

As indicated earlier, Eqs. (3-19) and (3-20) are only applicable over certain ranges of RMS, λ and r values. As RMS roughness decreases towards an atomically flat surface, Eq. (3-20) predicts a force of adhesion that is twice that predicted for the van der Waals interaction between a smooth surface and sphere. In this limit, the radius of the asperity approaches infinity and effectively equals the contribution of the planar non-contacting surface. This can be avoided if we restrict the range of RMS or r . These values may be evaluated if we introduce an “effective zone”, S_{eff} , i.e., the area of the surface that principally contributes to the interaction between the adhering particle and flat surface or spherical asperity.

An interacting sphere and flat surface separated by gap H are shown in Figure 3-4. Since van der Waals forces decrease rapidly as a function of distance, the effective zone for sphere may be determined by the projected area of the sphere on the flat plate where the separation distance is less than $2H$. Beyond $2H$, the contribution of non-contact forces is less than 12% of the force at distance H and may be considered negligible. For a given separation distance, H , the following formulae are obtained.

$$AB = 2R \sin \beta \quad (3-22)$$

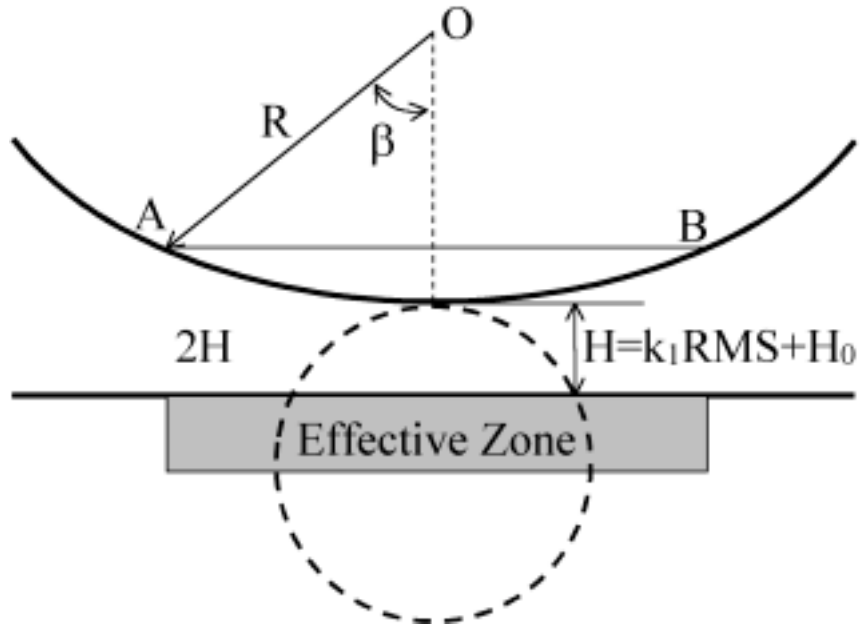


Figure 3-4: Effective Zone of Interaction. Illustration the concept of an effective zone of interaction between a flat surface and adhering spherical particle.

$$\cos \beta = \frac{R - H}{R} \quad (3-23)$$

For a small angle β ($H \ll R$), the following expression for the effective zone is obtained.

$$S_{\text{eff}} = \pi \left[\frac{AB}{2} \right]^2 = 2\pi HR \quad (3-24)$$

The effective zone, S_{eff1} , is equal to $4\pi RH_0/(r+R)$ for contact interaction between two spheres with radii R and r (i.e., adhering particle and spherical asperity), separated by the minimum intermolecular distance H_0 , 0.3 nm. For non-contact interaction between the adhering sphere, with radius R , and the average surface plane separated by gap (H_0+k_1RMS) , the effective zone S_{eff2} is equal to $2\pi R(H_0+k_1RMS)$. Therefore, Eqs. (3-19) and (3-20) are valid if $S_{\text{eff1}} \ll S_{\text{eff2}}$, meaning that the area of the average surface plane that contributes to the contact interaction between the particle and asperity is small compared

to the area of interaction between the particle and the average surface plane. Hence, the non-contact interaction between the particle and average surface plane may be calculated including the volume in common with that of the asperity. The radius, r , of the asperity increases when RMS decreases (see Eq. (3-14)), the following simple limit of applicability for Eqs. (3-19) and (3-20) may be obtained by comparing S_{eff1} and S_{eff2} for small roughness where RMS is approximately $\leq H_0/k_1$ and $r \ll R$. Using Eq. (3-14) and this condition, the range of λ , where the equations are valid may be obtained from.

$$\lambda \ll \sqrt{32k_1R \cdot \text{RMS}} \quad (3-25)$$

Eq. (3-25) may be used to determine the lower boundary for small values of roughness. The upper limit of roughness as described above yields, Eq. (3-26).

$$\lambda \gg 14.5 \cdot \text{RMS} \quad (3-26)$$

The dependence of the total normalized adhesion force as well as the contact and non-contact components as a function of RMS roughness calculated with Eq. (3-20), are presented in Figure 3-5 for an adhering particle of 10 μm radius, a Hamaker constant of 10^{-19} J, a distance of closest approach of 0.3 nm, and a peak-to-peak distance of 250 nm. Also replotted for comparison is the total normalized adhesion force as predicted by the modified Rumpf model, Eq. (3-7), at equivalent conditions. Unlike the modified Rumpf model, no minimum in the total normalized adhesion force predicted by the proposed model is observed. Instead, both the contact and non-contact terms contribute to the total predicted force of adhesion at small roughness. Also unlike the modified Rumpf model, it is now the contact term that provides the primary contribution to the total adhesion force. However, the non-contact term is not negligible in the nanoscale roughness regime. Hence, the adhesion force predicted by the proposed model may be a full order of

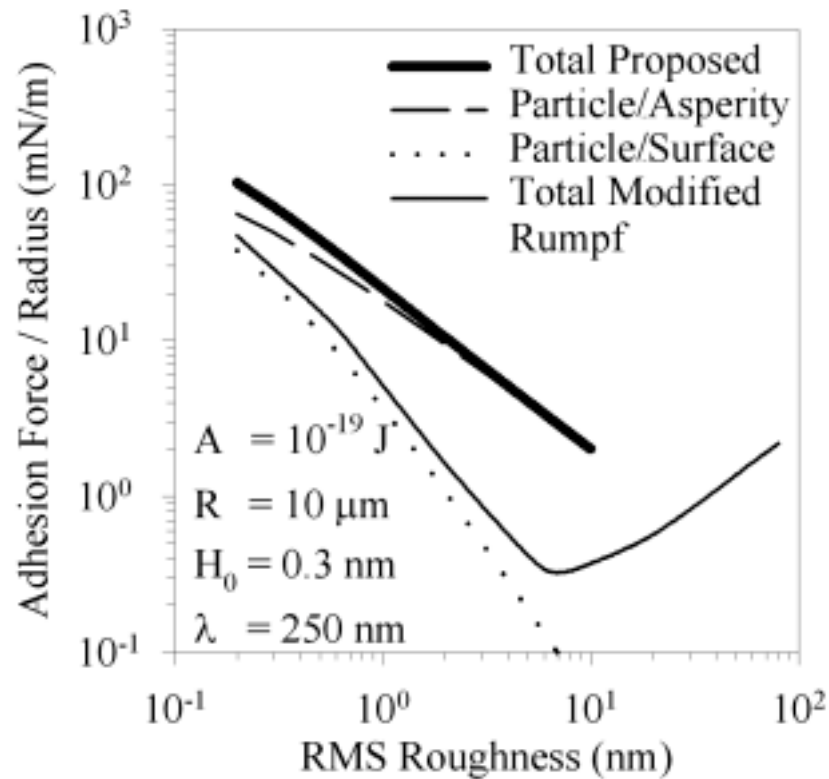


Figure 3-5: Comparison of Adhesion Models. Prediction of the total, contact, and non-contact force of adhesion, normalized by the radius of the adhering particle, between a $10 \mu\text{m}$ smooth sphere and a surface with nanoscale roughness using the proposed model, Eq. (3-20). Hamaker constant, A , is 10^{-19} J, peak-to-peak distance, λ , is 250 nm, and distance of closest approach, H_0 , is 0.3 nm. Also plotted for comparison is the predicted adhesion force from the modified Rumpf model, Eq. (3-7), using the same parameters except peak-to-peak distance which is not accounted for in the model.

magnitude greater than predicted by the modified Rumpf model. As the radius of the adhering sphere decreases, the contact contribution to the total predicted force increases, while the non-contact term remains constant. Hence, with decreasing particle size the interaction behavior approaches that of a perfect sphere/flat plate interaction.

Using the boundary conditions described above, the proposed model is valid in the range where $0.1 \ll \text{RMS} \ll 20 \text{ nm}$, for the given peak-to-peak distance. For roughness of greater magnitude, a correspondingly greater peak-to-peak distance would be present and hence would necessarily increase the upper RMS limit. While the modified Rumpf model does not theoretically have these limits, its predictive power in the extremes of roughness may still be limited. Specifically on surfaces with greater roughness, the asperities are rarely smooth. Hence, the increase in adhesion force predicted by the Rumpf model may not actually occur. Instead a second order of roughness, with a smaller radius or peak-to-peak distance, superimposed on the first may need to be considered. This concept will be explored further in Chapter 4.

Both the modified Rumpf and proposed models have other limitations in addition to those described above. These models were developed for a fixed particles adhering to a surface. Hence, the particle is not free to find an equilibrium position that would most likely consist of more than one contact with the surface. This increased number of contacts holds the possibility of increasing the total adhesion experienced by a particle. Note however, that during experimental determination of adhesion force by a method such as atomic force microscopy, the particle is fixed to the cantilever.

As stated earlier, the materials in these systems are also considered non-deformable under the applied loads. The effect of plastic deformation is neglected. In the Rumpf model at nanoscale roughness, the asperity size is necessarily small and so plastic deformation may appear to play a critical role. However, in the proposed model, the asperities are modeled as larger spheres with their centers below the surface, hence, the resistance to deformation is considerably increased. Additionally, other forces known to

act between some surfaces in dry contact such as polar interactions [ISR92] and contact electrification [HOR92] are also not considered. If the contributions of these forces were found to be significant, both would result in greater measured adhesion force.

Summary

To this point, a model has been developed to more accurately predict the force of adhesion between a particle and surface with nanoscale roughness. By modeling the surface roughness in a manner that more closely describes the true geometry of the surfaces a larger asperity radius is predicted that significantly impacts the relative contributions of contact and non-contact adhesion forces. For example, a predicted force of adhesion nearly two orders of magnitude greater, at 10 nm RMS roughness, than a similar model using a smaller radius was calculated. As this model more accurately simulates real surface geometries, it is expected that it will more accurately predict the measured force of adhesion described in Chapter 4.

CHAPTER 4 ADHESION BETWEEN NANOSCALE ROUGH SURFACES (VALIDATION)

Introduction

Few surfaces are smooth at the atomic level, and even highly polished surfaces possess some finite surface roughness. Such roughness is known to reduce adhesion between surfaces or between a particle and a surface due to a decrease in real area of contact and an increase in the distance between the bulk surfaces [TAB77, BRI92, KRU67, JOH71, MIZ96]. In Chapter 3, a theoretical framework was developed in order to more accurately account for nanoscale asperities at interfaces. This analysis resulted in a new model, based on a geometry, that considers both the height and breadth of asperities and yields an increased asperity radius compared to previous approaches. In this chapter, the proposed model will be validated by direct measurement of adhesion by atomic force microscopy (AFM) and extended to include polar forces and for surfaces with various scales of roughness.

One of the first systematic investigations of roughness effects on adhesion was conducted by Fuller and Tabor [FUL75] between a rubber surface and a polymethylmethacrylate (PMMA) surface with RMS roughness in the range of 120 - 1500 nm. They reported that a 1,000 nm increase in roughness reduced the adhesion force to approximately 10% of that predicted by van der Waals force between smooth surfaces. This study also indicated that adhesion force on rough surfaces was primarily determined by the distribution of asperity heights.

Iida et al. [IID93] experimentally determined the adhesion forces between smooth glass particles and glass substrate with roughness of 50 to 400 nm. The adhesion force was estimated by the average force needed to retain 50% of the particles after bombardment by gas or liquid. Similar to other investigations, they initially observed a factor of ten decrease in adhesion force followed by a region of more gradual decrease.

Recently, Shaefer et al. [SCH95], using AFM, have measured adhesion between 8 μm particles with roughness of 10 - 20 nm. In addition to deviation from the average center line, roughness was characterized by the estimated mean radius of curvature profile obtained by AFM. Experimental values of adhesion force were found to be fifty times less than the theoretical values for smooth glass particles based on Johnson-Kendall-Roberts, JKR, theory [JOH71]. When the estimated radius of the contacting asperity was used to calculate adhesion rather than the radius of spheres, the experimental data was only three times lower than predicted for smooth particles.

To understand the effect of surface roughness in the nanometer scale, the change in adhesion force must be accurately measured for very small deviations from ideally smooth surfaces. However, to the best of our knowledge, there has been no detailed investigation of nanoscale surface roughness effects on the adhesion force. As described previously, experimental studies have been performed for surface roughness values greater than ten nanometers [MIZ96, FUL75, IID93, SCH95]. However, both theoretical and experimental difficulties have resulted in a lack of experimental data in the nanometer surface roughness regime. Experimentally, it is difficult to obtain surfaces having regular and reproducible roughness of this scale and theoretical complications arise from an inability to characterize or properly define geometric models based on

experimentally measurable parameters. Due to a lack of experimental data, models developed to predict adhesion force as a function of surface roughness have not been accurately verified.

Experimental

Methods

Adhesion force was measured experimentally by atomic force microscopy (AFM) (Nanoscope III, Digital Instruments Inc.). Details of the technique have been described elsewhere [DUC92, RAB94]. Adhesion force measurements were made with either a glass sphere or an AFM silicon nitride tip attached to the cantilever. The experimental configuration for the two different measurements is shown in Figure 4-1. Since the radius of the glass sphere is much larger than the scale of the roughness, it is expected that contributions from both the contact and non-contact forces could be significant. In the case of the AFM tip, the radius of curvature is smaller than the scale of the surface roughness. As a result, the interaction is expected to be dominated by the contact forces and adhesion values are expected to be much closer to those predicted for the interaction of smooth surfaces as described in Chapter 3. Comparing these two geometries is intended to highlight the importance of the relative magnitude of the roughness compared to the size of the adhering particle.

Systematic errors, appearing due to the cantilever calibration, were found to produce variation in experimentally measured forces of approximately 10%. Small local variations of surface topography may also produce significant changes in adhesion force. As a result, the statistical scattering of adhesion force for a given data point was also

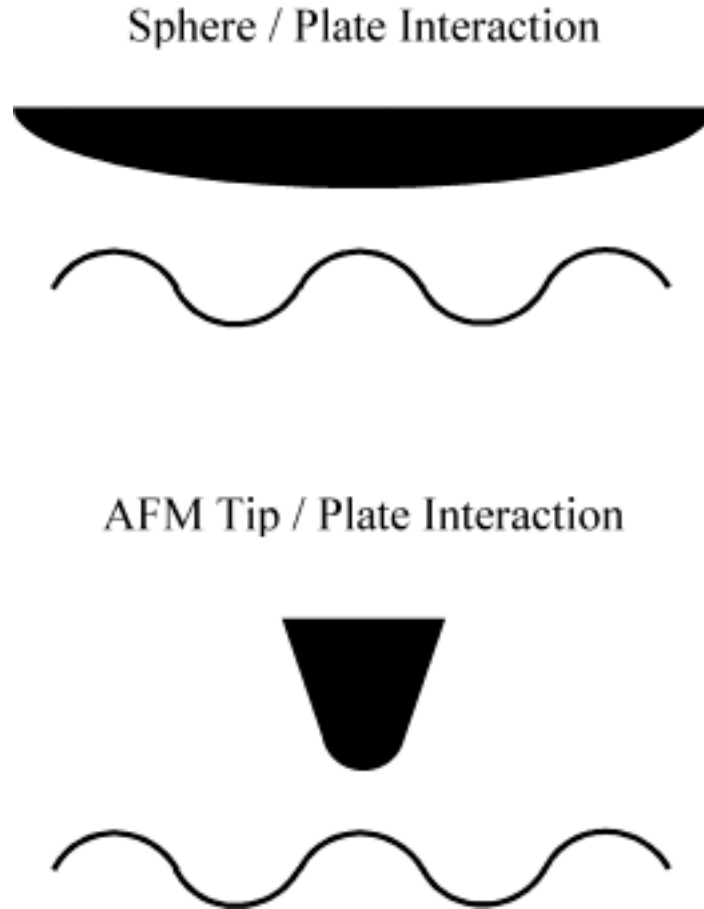


Figure 4-1: Experimental Configuration. Schematic of the experimental configuration for sphere-surface and tip-surface interactions. The radius of the AFM cantilever tip is small compared to the surface roughness, whereas the glass sphere is significantly larger.

approximately 10%. Presented data points are the average of at least 50 measurements at different locations on the surface.

Materials

Plates with controlled roughness were fabricated in the present study by deposition of titanium thin films (10 - 100 nm thick) on a silicon wafer substrate. Compositional homogeneity of the deposited films was verified by Auger spectroscopy.

In this system, the roughness of the surface is proportional to the thickness of the deposited film. In this manner, the RMS roughness was varied from 1.6 to 10.5 nm. The silicon wafer had an RMS roughness of 0.17 nm. Directly before each measurement surfaces were cleaned by rinsing with ethanol, methanol, and deionized water.

AFM surface roughness profiles for the plates used in this investigation are shown in Figure 4-2(a) through 4-2(d). Note that sample A is the silicon wafer without a coating of titanium. Upon initial inspection, the asperities seem approximately semi-spherical with their origins at the surface. However, since the vertical scale is greatly exaggerated the asperities should more appropriately be modeled, in contrast to previously proposed models of asperities, as spheres with the origin below the surface instead of semi-spheres. This allows the asperity to exhibit both the measured height and breadth, whereas, if the origin was restricted to the surface only, the height parameter is utilized. An important difference in this approach is that with the origin of the asperity located beneath the surface, the radius needed to produce a given height necessarily becomes larger.

The surfaces used in this investigation exhibited two types of roughness profiles. The first roughness to be defined, RMS_1 , is associated with the longer peak-to-peak distance, λ_1 , fluctuations (approximately 1000 nm) that occur on samples C and D (Figure 4-2(c) and 4-2(d)). The second, RMS_2 , occurs on all samples and has a peak-to-peak distance, λ_2 of approximately 250 nm. Note that on samples C and D, RMS_2 is superimposed on RMS_1 . The experimentally measured RMS and λ of the four samples are given in Table 4-1. Roughness in terms of RMS was determined by the analysis software of the AFM and the peak-to-peak distance taken in different directions from the images. Methods to calculate the radius of an asperity are detailed in Chapter 3.

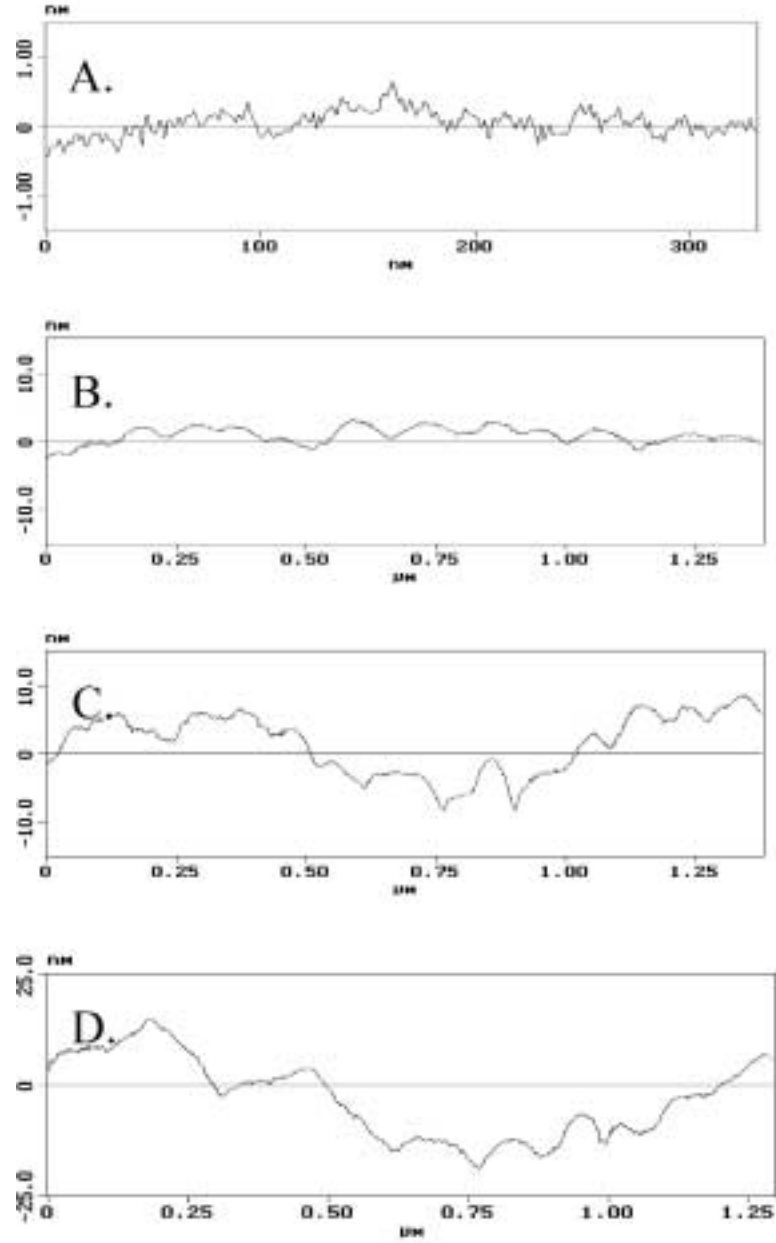


Figure 4-2: Surface Profiles. Surface roughness profiles, as determined by atomic force microscopy, of titanium deposited on the silicon substrates in order of increasing thickness and RMS roughness. Characterization parameters are summarized in Table 4-1.

Glass spheres were obtained from Duke Scientific Inc. and cantilevers from Digital Instruments Inc. The spheres possess a radius of approximately 10 μm and an RMS roughness of less than 0.2 nm. The measured radius of the AFM tip was approximately 50 nm.

Results

The force of adhesion, normalized by the radius of the adhering particle, between either the glass sphere, or AFM tip, and the samples of controlled roughness is presented in Table 4-2. For both the particle and tip a relatively sharp decrease in the normalized force of adhesion is detected upon a surface roughness increase of 0.17 to 1.6 nm RMS. For the 10 μm particle, the normalized force of adhesion decreases to 27% of the adhesion at 0.17 nm RMS. However, upon further increase in roughness to 10.5 nm RMS the adhesion is still 19% of the adhesion of sample A. Similar trends are observed when

Table 4-1: Characteristics of the Model Surfaces. Measured roughness parameters, RMS and λ , for the model surfaces. Values of radii of peaks r_1 and r_2 are calculated from Eq. (4-16) in Chapter 3. Note that sample A is the uncoated silicon wafer.

Sample	RMS ₁ (nm)	RMS ₂ (nm)	λ_1 (nm)	λ_2 (nm)	r_1 (μm)	r_2 (μm)
A	0	0.17	-	250	∞	6.3
B	0	1.64	-	249	∞	0.75
C	4.3	1.64	1180	237	5.6	0.69
D	10.5	1.64	1046	260	1.8	0.81

the particle size is less than the peak-to-peak distance of the roughness. For the interaction of the AFM tip and sample B the normalized force of adhesion is 83% of the interaction between the tip and sample A. However, even for a 7 fold increase in surface roughness to 10.5 nm (sample D) RMS, the adhesion is still nearly 60% of the interaction between that of the tip and sample A.

The absolute adhesion magnitude between the two samples is also significantly different, indicating that when normalized by the radius of the adhering particle the smaller particle (AFM tip) has relatively more intimate contact with the surface. This data indicates a rather large decrease in the normalized adhesion force with small deviations from an ideally smooth surface and that this decrease becomes less significant with further increase in surface roughness. In the following sections these experimental data will be compared to both the modified Rumpf model and the model developed in this study (Chapter 3).

Table 4-2: Measured Force of Adhesion. Measured normalized force of adhesion between the sphere or tip and the model surfaces normalized by the radius of the adhering particle.

Sample	RMS ₁ (nm)	RMS ₂ (nm)	Normalized Force of Adhesion (mN/m)	
			Glass Sphere/Plate	AFM Tip/Plate
A	0	0.17	100	600
B	0	1.64	27	500
C	4.3	1.64	23	370
D	10.5	1.64	19	350

Comparison with the Modified Rumpf Model

As described in Chapter 3, the model originally proposed by Rumpf [RUM90] modified to predict adhesion as a function of RMS roughness instead of asperity radius is given as Eq. (4-1).

$$F_{ad} = \frac{AR}{6H_0^2} \left[\frac{1}{1 + R / (1.48 \cdot RMS)} + \frac{1}{(1 + 1.48 \cdot RMS / H_0)^2} \right] \quad (4-1)$$

Adhesion forces calculated using Eq. (4-1) will be called the modified Rumpf approach in the remainder of the study. As noted above, samples C and D exhibit more than one peak-to-peak distance of roughness. Since AFM averages the smaller superimposed roughness to zero this secondary roughness is not accounted for. Therefore to apply the modified Rumpf model for the surfaces used in this investigation the total roughness of the surfaces, as calculated by Eq. (4-2), will be used.

$$RMS = RMS_{\Sigma} = \sqrt{RMS_1^2 + RMS_2^2} \quad (4-2)$$

where RMS_1 and RMS_2 are average root mean square roughness of the long and short peak-to-peak distances, respectively. Eq. (4-2) is applicable if RMS_2 is much less than or much greater than RMS_1 .

Hamaker constants for the various interactions are needed to apply Eq. (4-1) and the proposed model developed below. The Hamaker constant, A_{11} , is approximately 0.65×10^{-19} J for amorphous silica [ISR92] and 1.72×10^{-19} for silicon nitride [MEU97]. A_{11} for silicon was calculated, using the optical data of Visser [VIS72], and determined to be 2.65×10^{-19} J [FIE96]. The Hamaker constant for metals are expected to be 2 to 4×10^{-19} [ISR92], so for simplicity A_{11} for titanium is considered to be equal to that of silicon.

To estimate the Hamaker constant between dissimilar materials a combining rule approximation [ISR92]

$$A_{12} = \sqrt{A_{11} \cdot A_{22}} \quad (4-3)$$

results in $A_{12} = 1.31 \cdot 10^{-19}$ J for silica/ silicon and silica/ titanium, and $A_{12} = 2.13 \times 10^{-19}$ J for silicon nitride/silicon and silicon nitride/titanium.

Utilizing this approach, the theoretical and experimentally measured normalized adhesion force between the smooth sphere and substrates as a function of the total root mean square roughness, RMS_{Σ} , as plotted in Figure 4-3. Theoretical values were calculated by the modified Rumpf model, Eq. (4-1), for a minimum contact distance, H_0 , of 0.3 nm, and a particle diameter, R , of either 10 μm for the glass sphere or 50 nm for the AFM tip. For both the large and small particles, it is clear that the adhesion forces calculated using this model underestimate the experimental values by more than an order of magnitude. This discrepancy is primarily attributed to the underestimation of the radius of the asperity in Rumpf's model as described in Chapter 3.

The increase in adhesion force predicted for the AFM tip/surface interaction, especially at roughness greater than approximately 1 nm RMS is also to be noted. This trend is not mirrored in the experimental data suggesting that the secondary roughness may actually play a more significant role in controlling the adhesion force. Even though the radius of the asperity begins to increase to where the adhering particle/asperity forces theoretically dominate, the secondary roughness reduces the real area of contact, in effect once again reducing the roughness to the nanoscale. The phenomena of most surfaces with apparently larger scale roughness comprised of multiple roughness scales may also help to explain some of the experimentally measured differences described earlier.

Comparison with the Proposed Model (van der Waals Approach)

The roughness of the model surfaces is inadequately described by the geometry proposed in the Rumpf model. A new model, described in Chapter 3, that more

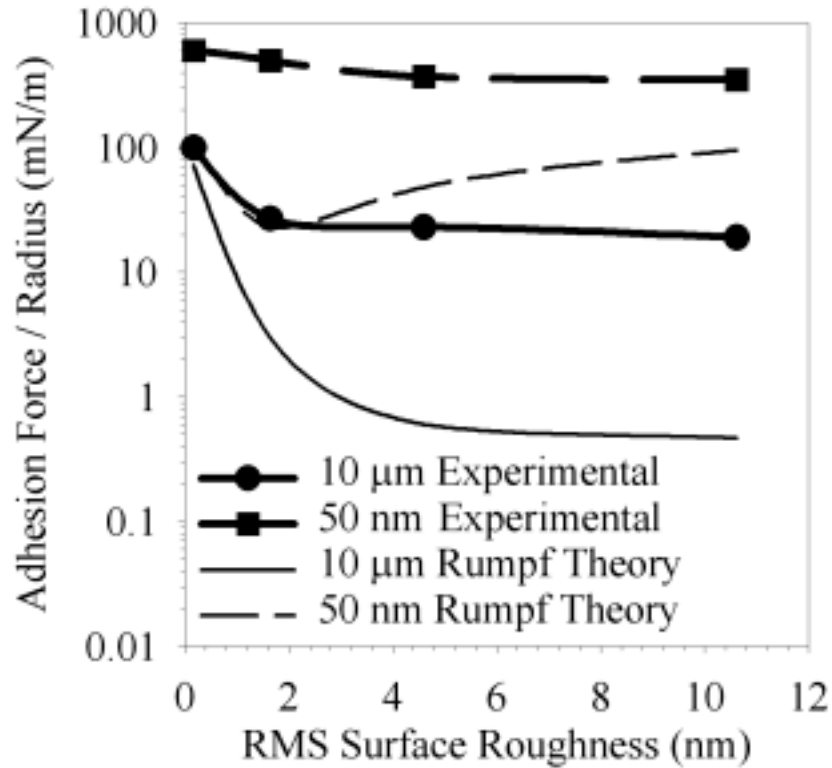


Figure 4-3: Comparison of Measured Adhesion with Modified Rumpf Model. Experimentally measured normalized adhesion force between the glass sphere or AFM tip and the model substrates as a function of increasing nanoscale roughness, RMS_{Σ} . The theoretical adhesion calculated with the modified Rumpf model (Eq. [1]) with $A_{12} = 1.31 \cdot 10^{-19}$ J for silica/silicon and silica/titanium, $A_{12} = 2.13 \times 10^{-19}$ J for silicon nitride/silicon and silicon nitride/titanium, $H_0 = 0.3$ nm, and $R_{\text{sphere}} = 10 \mu\text{m}$ or $R_{\text{tip}} = 50$ nm underestimates the measured adhesion force by more than an order of magnitude.

accurately describes the surface roughness must be employed. However, the model must be additionally modified to account for the second order of roughness on samples C and D. The geometry of this model is shown schematically in Figure 4-4. In this model roughness is described by asperities with heights $y_{1 \text{ max}}$ and $y_{2 \text{ max}}$ as well as peak-to-peak distances λ_1 and λ_2 .

To calculate the adhesion force in the framework of this model, Eqs. (3-14), (3-16), and (3-18), are considered valid for each superimposed roughness scale. As a result, similar to derivation of Eq. (3-19), but also accounting for the contact interaction of sphere with RMS_2 and non-contact interaction with the RMS_1 and flat substrate, the following formulas are obtained.

$$F_{ad} = \frac{AR}{6H_0^2} \left[\frac{r_2}{R + r_2} + \frac{r_1}{(r_1 + R) \left(1 + \frac{y_{2max}}{H_0} \right)^2} + \frac{1}{\left(1 + \frac{y_{1max} + y_{2max}}{H_0} \right)^2} \right] \quad (4-4)$$

or

$$F_{ad} = \frac{AR}{6H_0^2} \left[\frac{1}{1 + \frac{58R \cdot RMS_2}{\lambda_2^2}} + \frac{1}{\left(1 + \frac{58R \cdot RMS_1}{\lambda_1^2} \right) \left(1 + \frac{1.82RMS_2}{H_0} \right)^2} + \frac{H_0^2}{(1 + 1.82(RMS_1 + RMS_2))^2} \right] \quad (4-5)$$

In Eqs. (4-4) and (4-5), the first, second and third terms in brackets correspond to the interaction of the adhering particle with RMS_2 , RMS_1 , and the average surface plane, respectively. These equations are valid if the radius of the asperity, r_1 or r_2 and the peak-to-peak distance, λ_1 or λ_2 , associated with both superimposed roughness are much less than the radius of the adhering particle. As λ_1 becomes comparable to R , there is less and less material in the average surface plane that is not already contained in the asperity. Hence, for such a situation, the third term in Eqs. (4-4) and (4-5) is largely redundant and must be dropped, yielding the following.

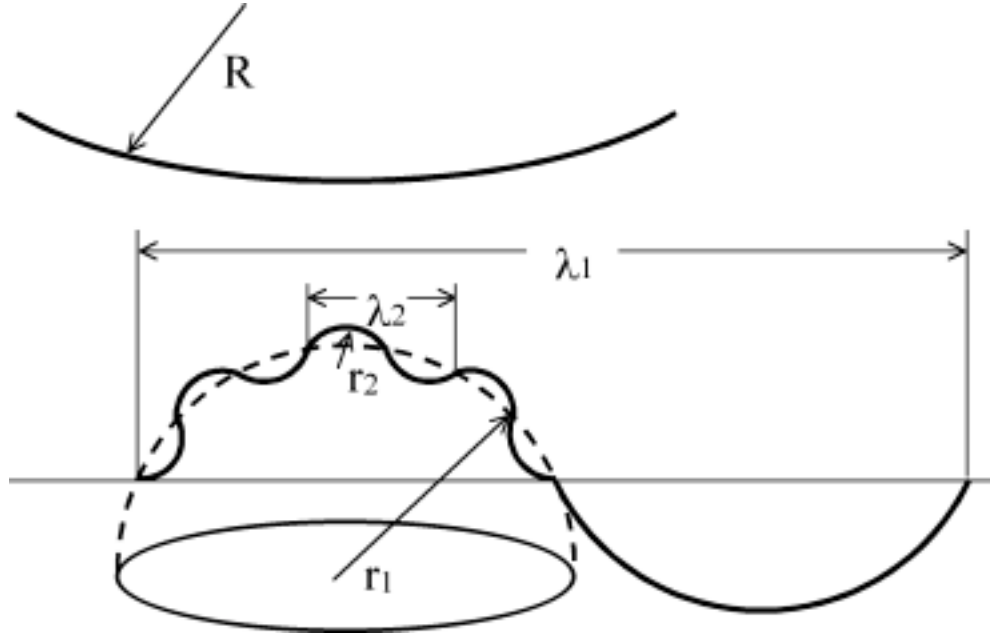


Figure 4-4: Asperity Schematic for Surfaces with Two Roughness Scales. Schematic illustration of the geometric model used to calculate adhesion force in the proposed model. The surface is proposed to consist of an array of spherical asperities and troughs with the origin of the asperities positioned below the average surface. In this model two superimposed roughness profiles are needed to model surfaces C and D.

$$F_{ad} = \frac{AR}{6H_0^2} \left[\frac{1}{1 + \frac{58R \cdot RMS_2}{\lambda_2^2}} + \frac{1}{\left(1 + \frac{58R \cdot RMS_1}{\lambda_1^2}\right) \left(1 + \frac{1.82RMS_2}{H_0}\right)^2} \right] \quad (4-6)$$

Eq. (4-6) is applicable at any value of RMS_1 . In the limit of small values of RMS_1 , when $RMS_1 \ll \lambda^2/58R$, Eq. (4-6) reduces to Eq. (3-20).

Because the rougher surfaces in this study exhibited multiple roughness components, theoretical and experimental data are plotted as a function of the two primary variables, RMS_1 and RMS_2 at λ_1 of 1110 nm and λ_2 of 250 nm, taken as an average of the values measured on the model surfaces. The Hamaker constant, minimum

contact separation distance, and radius of the sphere were kept identical to those used in the modified Rumpf model prediction. Figure 4-5 compares the normalized adhesion force measured between the glass sphere and model surfaces with theoretically predicted values using Eq. (4-6). Comparison of experimental and theoretical data suggests that a principle contribution to the adhesion force is van der Waals attraction. Note, however, that a discrepancy still exists between the theoretical and measured values. While these predictions represent a significant improvement over the modified Rumpf model (Fig. 4.3), the experimentally measured values of adhesion force at $RMS_2 = 1.64$ nm are consistently larger by almost a factor of two than the theoretically predicted values.

Experimental error alone ($\pm 10\%$) can not account for this difference. One remaining factor not taken into account in the proposed model is polar interactions [ISR92]. Polar forces are known to be significant in contact interactions and, therefore, may be especially important in the proposed model at low RMS roughness values. To account for these additional forces a surface energy approach is necessary for the contact interactions. This may be important because polar forces, primarily hydrogen bonding, that operate between contacting surfaces may be equal to or greater in magnitude than the van der Waals component of surface energy [ISR92]. For example, for glass surfaces the van der Waals component of the work of adhesion at contact is approximately 19 mJ/m^2 , while experimentally measured values range from 50 to 80 mJ/m^2 depending on the degree of hydroxylation [BRA32, YAM75, YAM98]. The utility of such an approach will be explored in the next section.

Contact electrification has also been reported to enhance the adhesion between dry surfaces [HOR92]. This electrostatic adhesion, related to transfer of charge during

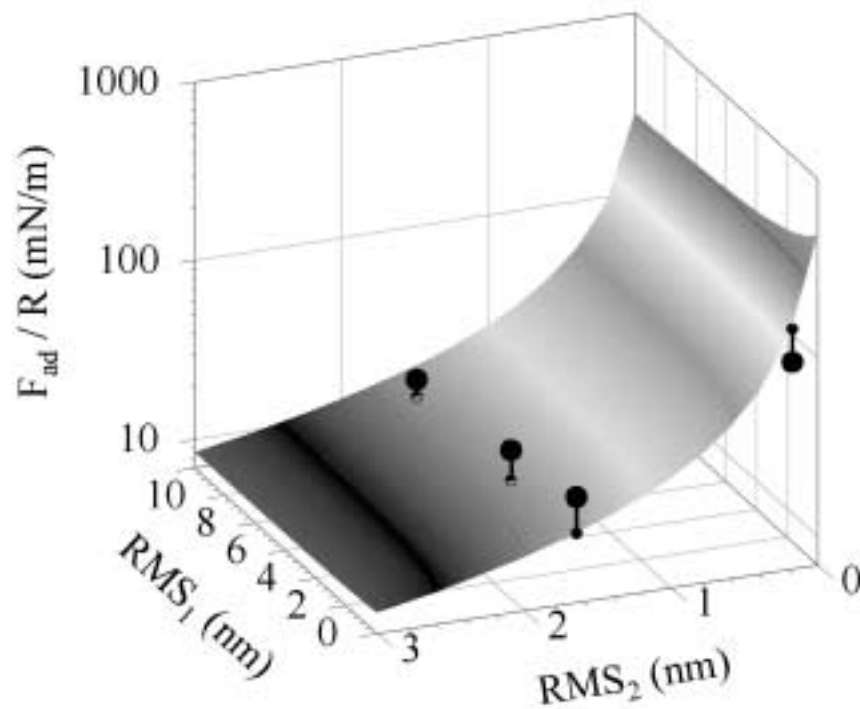


Figure 4-5: Experimental and Theoretical Adhesion for Sphere/Surface Interaction. Experimentally measured normalized adhesion and theoretical predictions for the interaction of the glass sphere with the model surfaces as a function of RMS_1 and RMS_2 . Theoretical predictions were made using Eq. (4-6) with $A_{12} = 1.31 \cdot 10^{-19}$ J, $H_0 = 0.3$ nm, $R = 10$ μ m, $\lambda_1 = 250$ nm, and $\lambda_2 = 1110$ nm.

separation of surfaces, may produce adhesion forces two orders of magnitude greater than the ideal van der Waals forces [HOR92] but was not observed during the present investigation. Possible reasons include a thin oxidation layer, observed by Auger spectroscopy, that may have increased the work function of the titanium surfaces such that charge transfer was not possible or that the measurements were conducted in air at approximately 25% relative humidity, as opposed to the experiments of Horn and Smith [HOR92] where a dry nitrogen atmosphere was used. It is possible that the water

adsorbed under these conditions was enough to dissipate any charge that accumulated on the surfaces.

Experimental results and theoretical predictions, calculated by Eq. (4-6), for the interaction of the AFM tip with the model surfaces are shown in Figure 4-6. The values of the variables used are identical to those in Figure 4-5 with the exception of the smaller radius of the adhering particle ($R = 50 \text{ nm}$) and the different Hamaker constant ($A_{12} = 2.13 \times 10^{-19} \text{ J}$). The same AFM cantilever was used in all experiments to eliminate variability in spring constant and tip dimensions. Furthermore, the tip required a “break in” period before reproducible measurements were achieved. This period is assumed to correspond to the wearing of the tip to a stable radius of curvature.

The radius of tip is smaller than either of the surface roughness peak-to-peak distances. Hence, the tip penetrates between asperities and contact forces dominate. As a result, the decrease of adhesion force upon increase of the surface roughness from $\text{RMS} = 0.2 \text{ nm}$ to 1.6 nm is only 1.5 times, whereas for the glass particle the same conditions produced a five-fold decrease in the force of adhesion. Once again the predicted interaction using Eq. (4-6) results in an underestimated value of adhesion force as compared with experimental data. This may be attributed to contributions from polar forces that are larger in magnitude in the present case because of the greater normalized surface area in contact. To more accurately evaluate the magnitude of these additional adhesion forces, the contact force between the adhering particle and an asperity may alternatively be modeled using the surface energy approach with the proposed description of the asperity radius.

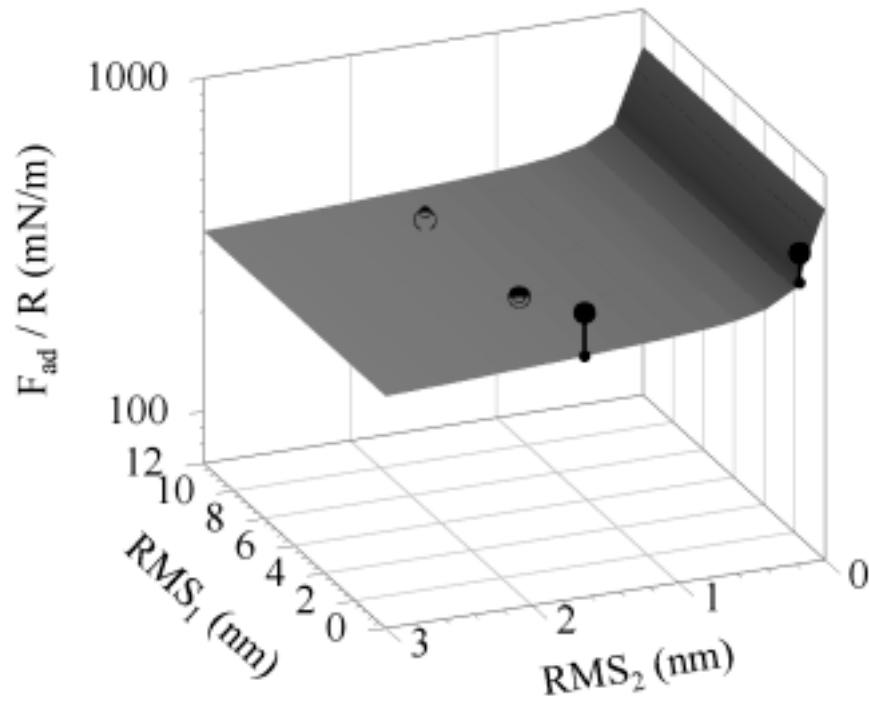


Figure 4-6: Experimental and Theoretical Adhesion for AFM Tip/Surface Interaction. Experimentally measured normalized adhesion and theoretical predictions for the interaction of the AFM cantilever tip with the model surfaces as a function of RMS_1 and RMS_2 . Theoretical predictions were made using Eq. (4-6) with $A_{12} = 2.13 \times 10^{-19}$ J, $H_0 = 0.3$ nm, $R = 50$ nm, $\lambda_1 = 250$ nm, and $\lambda_2 = 1110$ nm.

Comparison with the Proposed Model (Surface Energy Approach)

It should be noted that all equations for calculation of adhesion force based on Rumpf's model described above are developed for non-deformable surfaces. To incorporate this effect and account for the total surface energy, two limiting cases of adhesion as described in Chapter 2, both of which imply elastically deformable surfaces, are often applied. Derjaguin-Muller-Toporov (DMT) mechanics [DER75] is often applied

for harder materials where at the point of detachment there is no deformation. Similarly, Johnson-Kendall-Roberts (JKR) mechanics [JOH71] is often determined to be the limiting case for softer materials. Johnson and Greenwood [JOH97] suggested a parameter, μ , which if greater than 0.01 indicated an interaction more closely approximated by JKR mechanics as opposed to the DMT model. This parameter may be written as

$$\mu = \left(\frac{rW^2}{K^2 H_0^3} \right)^{1/3} \geq 0.01 \quad (4-7)$$

where W is the work of adhesion between the two interacting surfaces, r is the radius of the asperity, H_0 is the minimum separation distance between contacting surfaces (0.3 nm), and K is the reduced combined elastic modulus [BUR22].

$$K = \frac{4}{3} \left[\left(\frac{1-\nu_1^2}{E_1} \right) + \left(\frac{1-\nu_2^2}{E_2} \right) \right]^{-1} \quad (4-8)$$

E_1 , E_2 , ν_1 , and ν_2 are the elastic moduli and Poisson ratios for materials 1 and 2, respectively. For asperity or tip radii used in this investigation and $W = 91.5 \text{ mJ/m}^2$ (silicon nitride/tungsten interaction) the minimum value of μ is approximately 0.08, indicating that the JKR model may be used to evaluate the contact interaction between the adhering particles and asperities. Using this approach Eq. (4-6), may be rewritten by replacing the first term in this equation by adhesion force between two spheres as determined by JKR theory.

$$F_{\text{ad}} = \frac{3\pi WRr}{2(r+R)} + \frac{\left(\frac{AR}{6H_0^2} \right)}{\left(1 + \frac{58R \cdot \text{RMS}_1}{\lambda_1^2} \right) \left(1 + \frac{1.82\text{RMS}_2}{H_0} \right)^2} \quad (4-9)$$

As a final criteria to evaluate the applicability of the proposed model, the size of any plastically deformed zone should be small compared to the size of the asperity. If the two are of similar magnitudes the asperity will essentially be flattened by the adhering particle and the effect of surface roughness will be negligible. The model of Pollock and Maugis [MAU84] assumes that all of the applied force produces plastic deformation of the surface and so yields the upper limit of the plastically deformed zone. Their equation has the form

$$F_{ad} = \frac{3}{2} \pi W \frac{Rr}{(R+r)} = 3\pi a_{pl}^2 Y \quad (4-10)$$

in which the applied force is set equal to the force of adhesion, F_{ad} , determined by JKR mechanics with the work of adhesion, W , determined from the fitted values described below. R is the radius of the adhering particle (either the glass sphere or AFM tip), r is the radius of the asperity, a_{pl} is the radius of plastically deformed zone, and Y is the yield stress of the plastically deformed material (derived from the assumption that hardness is approximately $3Y$). Using this approach, the largest calculated plastic area radius between glass particle with $Y = 3.6$ GPa [ASH91], and titanium asperity with $Y = 0.18$ GPa [ASH91] and $W = 69.5$ mJ/m² is approximately 16 nm. Interactions between the AFM tip with $Y = 8.0$ GPa [ASH91], and asperities yielded values of approximately 5 nm. This radius overestimates the radius of the plastically deformed zone and is still much smaller than the radius of the smallest asperity ($0.7 \mu\text{m}$) or peak-to-peak distance (~ 250 nm). Hence it is appropriate to assume that the asperities are not significantly plastically flattened by the adhering particles. This example also reinforces the importance of considering the correct radius of the surface asperities in other types of surface interactions.

Tables 4-3 and 4-4 compare the experimentally measured adhesion between the glass sphere or AFM tip and the model surfaces to those predicted by Eq. (4-9). The principle drawback of the surface energy approach, however, is that while good estimations of van der Waals attraction for a wide variety of surfaces may be made, no such methodologies exist for the work of adhesion. To overcome this barrier a best fit approach was utilized for each pair of interacting surfaces. The results of this fit and the van der Waals component are also given in Table 4-3 and 4-4. It appears that, the van der Waals component represents approximately 50 - 70% of the total fitted interaction energy.

It should be emphasized that the majority of the refinements to the model only attempt to further increase the accuracy beyond the $\pm 50\%$ of the measured value offered by the model developed in Chapter 3, compared to the nearly 10 to 50 times

Table 4-3: Normalized Force of Adhesion: Glass Sphere (Surface Energy Approach). Predicted normalized force of adhesion between the glass sphere and model surfaces calculated by Eq. (4-9) and compared with measurement. The fitted total work of adhesion and the van der Waals contribution to the overall work of adhesion are also shown.

Sample	Work of Adhesion:		Normalized Force	
	Calculated by	Fitted Work of Adhesion: Total	of Adhesion (mN/m)	
	van der Waals (mJ/m ²)	(mJ/m ²)	Experimental	Predicted
A	39	55.0	100	100
B	39	69.5	27	23
C	39	69.5	23	22
D	39	69.5	19	25

underestimation resulting from other models which incorporate asperities with radii in the nanometer size range. This underestimation of the adhesion occurs not only with the van der Waals based Rumpf approach as detailed above, but also with more complex models considering surface energy and elastic deformation such as JKR theory. In fact, exact prediction remains difficult, even with these more rigorous analyses, due to the increased number of unknown parameters needed to apply the models. Hence, the principle finding of the present investigation is that regardless of the exact model used (Rumpf, DMT, JKR) the predicted adhesion values is primarily dependent on deriving a realistic value of the radius of the asperities on the surface.

Table 4-4: Normalized Force of Adhesion: AFM Tip (Surface Energy Approach).
 Predicted normalized force of adhesion between the AFM tip and model surfaces calculated by Eq. (4-9) and compared with measurement. The fitted total work of adhesion and the van der Waals contribution to the overall work of adhesion are also shown.

Sample	Work of Adhesion:	Fitted Work of	Normalized Force	
	Calculated by	Adhesion: Total	of Adhesion (mN/m)	
	van der Waals (mJ/m ²)	(mJ/m ²)	Experimental	Predicted
A	63	128	600	598
B	63	91.5	500	404
C	63	91.5	370	405
D	63	91.5	350	409

Summary

In this chapter, the force of adhesion between surfaces with nanoscale roughness was measured. The results validated previous investigations, at larger roughness, where a decrease of adhesion force as a function of roughness was reported [IID93, SCH95]. Measurement of adhesion was also performed at lower roughness than previously reported. It was experimentally determined that a roughness value as small as 1.6 nm RMS was significant enough to decrease the force of adhesion by nearly a factor of five. The magnitude of this decrease was additionally found to have a strong dependence on the radius of the sphere contacting the surface. When the adhesion force was probed with a sphere whose radius was of the same order or smaller than the radius or peak-to-peak distance of the roughness, the decrease of adhesion upon increase of surface roughness to 1.6 nm RMS was only 1.5 times, thus, more closely approximating the contact of an ideally smooth sphere and flat surface.

As described in Chapter 3 and 4, the key to predicting the interactions is to model the roughness in a manner that more closely describes the true geometry of the surfaces. In the proposed model, through an analysis of the surface topography by atomic force microscopy, a mathematical description of both the height and breadth of the asperities was determined, which are expressed as RMS roughness and peak-to-peak distance, respectively. The radius of the surface asperities as determined by this method was much larger than considered in previous models. As a result, the experimental force of adhesion was predicted within 50% of experimental values using a van der Waals force based approach. Previous models underestimated adhesion by 10 to 50 times. Application of the proposed geometries with JKR mechanics was found to further reduce the error, albeit with fitted (yet realistic) values of the work of adhesion. Using a realistic value of the

radius of asperities on the nanoscale was determined to be the most important parameter in accurately predicting adhesion between surface with nanoscale roughness.

In the previous chapters, adhesion models have been derived for a variety of surface geometries. However, only van der Waals and polar forces have so far been considered. It may be expected that roughness on the nanoscale may also influence other mechanisms of adhesion. Chapter 5, will explore the effect of the non-ideal interface (surface roughness) in humid atmospheres where capillary condensation may dramatically increase observed adhesion forces.

CHAPTER 5 CAPILLARY FORCES BETWEEN NANOSCALE ROUGH SURFACES

Introduction

The flow and adhesion behavior of fine powders (approximately less than 10 μm) is significantly affected by the magnitude of attractive interparticle forces. Hence, the relative humidity at which capillaries form and the magnitude of capillary forces are critical parameters in the processing of these materials. Using the general models of non-ideal surfaces developed in previous chapters, approximate theoretical formulae will be developed to predict the magnitude and onset of capillary adhesion between a smooth adhering particle and a surface with roughness on the nanometer scale. The theoretical predictions are validated using experimental adhesion values between a variety of surfaces.

In industrial operations ranging from the transport and handling of fine powders to the removal of abrasive particles after a polishing operation, the magnitude of forces between two surfaces is critical. As described in previous chapters, there are a number of approaches to predict these interactions based on van der Waals adhesion [HAM37] or through surface energy based approaches such as Johnson-Kendall-Roberts (JKR) [JOH71] or Derjaguin-Muller-Toporov (DMT) [DER75] adhesion theory. With real surfaces, however, there are a number of difficulties associated with applying these models. One principal concern is the effect nanoscale roughness has on the real area of contact and, subsequently, the magnitude of the force of adhesion. In Chapter 4, it has

been shown that deviations from ideality, as small as one nanometer RMS roughness, may significantly reduce the force of adhesion. A second concern, especially in industrial operations, is the increase in the adhesion force associated with the spontaneous formation of a meniscus in the capillary between two adhered particles or a particle adhered to a surface. This increase may significantly impact processing operations.

Concerning capillary forces, there are two critical issues that warrant discussion. Both the magnitude of the capillary force of adhesion and the environmental conditions, such as relative humidity, that allow a meniscus to form and enhance adhesion are important to predict. A number of authors have investigated the effect of relative humidity on condensation in capillaries and the validity of Kelvin's equation at various conditions [PIE67, SKI72, FIS81a, FIS81b, MEL89,]. An early detailed discussion of these phenomena related to particulate adhesion was presented by Coelho and Harnby [COE78a, COE78b]. Utilizing Kelvin's equation to describe the lesser radius of curvature of the meniscus, the Laplace equation to predict the pressure inside the meniscus, and adding the adhesion component produced by the surface tension, a description of capillary adhesion was developed. Furthermore, these authors believed that the onset of capillary forces should occur when the pressure inside the liquid annulus is equal to the vapor pressure, as the liquid would otherwise boil. Subsequently, a criteria for meniscus formation in terms of the vapor pressure and the BET constant was developed. Early experiments in general confirmed the basic form of these equations but showed that this criteria significantly overestimated the critical relative humidity for the onset of capillary forces [FIS81c].

Recently, Marmur [MAR93] and de Lazzer et al. [DEL99] have extended these basic theories for other geometries, environmental conditions, and separation distances while more accurately describing the meniscus and its effect on adhesion. De Lazzer et al. incorporated surface tension in their model and discussed capillary adhesion for a variety of probe geometries including spherical, conical, and parabolic. The ratio of the surface tension component to the internal pressure component is also explored and the conditions where they are comparable were delineated. In both papers, however, surfaces are considered to be ideally smooth.

Fisher and Israelachvili [FIS81c] investigated adhesion between smooth mica surfaces in the presence of water and cyclohexane vapors and directly measured the relative contribution of solid-solid interactions and the capillary effect on the total adhesion force. Rabinovich et al. [RAB91] further explored this area through direct measurement of the force of adhesion between fused quartz filaments in various semi-miscible liquids. Recent investigation, by Kohonen and Christenson, has also detailed the important effect of soluble contaminants on surfaces in altering the measured forces and critical relative humidity [KOH00]. The effect of surface hydrophobicity and specific surface groups on the onset of capillary force has also been the subject of direct measurement recently by Fuji et al. [FUJ99]. However, the change in roughness possibly associated with these surface modification techniques was not considered but is suggested to affect the measured adhesion.

Sirghi et al. [SIR00] further discussed the Marmur and de Lazzer's models with the incorporation of local curvature and suggested an analytical solution for capillary and surface tension adhesion forces using the approximation of a spherical particle geometry

and a symmetrical water meniscus at thermodynamic equilibrium. Theoretical results are compared with forces measured between a silicon nitride atomic force microscopy (AFM) tip and a platinum covered quartz sample with roughness on the order of 20 nm. This order of roughness is approximately the same magnitude as the AFM probe and so is not directly applicable to the case of a particle with a rough surface.

Quon et al. [QUO00] were principally concerned with the differences in surface characteristics on the capillary adhesion of surfaces. In their investigation, adhesion forces were measured between gold coated mica crossed cylinders which had been modified by alcohol or methyl self-assembled monolayers. A significant effect of the approximately 2 nm RMS roughness was observed but no theoretical formulae were developed.

Theory

Adhesion to Surfaces with Nanoscale Roughness

Before developing a predictive model of capillary forces between surfaces, a brief review of adhesion in gaseous atmospheres where no liquid annulus is expected to form is necessary. In Chapter 4, it was suggested that the force of adhesion between a smooth sphere and surface with nanoscale roughness could be expressed by the following relationship

$$F_{\text{dry}} = \frac{AR}{6H_0^2} \left[\frac{1}{1 + 58.14R \cdot \text{RMS}/\lambda^2} + \frac{1}{(1 + 1.817\text{RMS}/H_0)^2} \right] \quad (5-1)$$

where A is the Hamaker constant, R is the radius of the adhering particle, H_0 is the minimum separation distance between the adhering particle and asperity (0.3-0.4 nm), RMS is the root mean square roughness of the flat surface, and λ is the average peak-to-peak distance between asperities. In this approach the first term in brackets represents the

contact interaction of the particle with an asperity and the second term accounts for the non-contact interaction of the particle with an average surface plane. As discussed earlier, this approach models nanoscale roughness not as nanometer sized spherical asperities with their centers located at an average surface plane but rather as the caps of larger asperities with their centers located far below the surface. As a result of modeling the surface in this manner, both the height and breadth of the asperities are accounted for and more reliable predictions of experimental adhesion values are achieved, as detailed in previous chapters. In the nanoscale regime, it should be noted that the interaction of the particle with the asperity dominates the interaction and it is possible to replace the first term in the interaction with a surface energy based approach model as expressed for JKR mechanics by Eq. (5-2),

$$F_{\text{dry}} = \frac{3\pi\gamma R\lambda^2}{(\lambda^2 + 58.14R \cdot \text{RMS})} + \frac{AR}{6(H_0 + 1.817\text{RMS})^2} \quad (5-2)$$

where variables are equivalent to those in Eq. (5-1) except the surface energy parameter, γ .

In the application of this model to real systems, a relationship between the experimentally accessible RMS roughness and the true radius of the asperities was developed. From Chapter 3, if the peak-to-peak distance between asperities, λ , is known, this may be calculated as

$$r = \lambda^2 / 58.14\text{RMS} \quad (5-3)$$

Note also that the separation distance between the average surface plane and bottom of the adhering particle, H , in this model is

$$H = 1.817\text{RMS} \quad (5-4)$$

Very small deviations from an ideally smooth surface can account for large deviations in adhesion. For example, as detailed in Chapter 4, roughness of 1 or 2 nm RMS is significant enough to reduce theoretical adhesion by an order of magnitude or more. It is believed that similar effects may be observed in capillary adhesion processes.

Capillary Adhesion to Surfaces with Nanoscale Roughness

The geometry of a liquid annulus between an ideally smooth solid sphere and flat substrate is shown in Figure 5-1. For simplicity the system may be described by a Cartesian coordinate system since rotational symmetry is assumed about the ordinate axis. The capillary adhesion (detachment) force F_C between the particle and substrate has two principal components. The first force component, F_p , arises from the pressure differential, ΔP , between the inside and outside the liquid annulus. The second, F_s , arises from the vertical component of the surface tension acting along the meniscus. The sum of these forces may be written as

$$F_C = F_p + F_s = \pi x^2 \Delta P + 2\pi\gamma_L R \sin(\theta_1 + \alpha) \quad (5-5)$$

where the pressure difference, ΔP , in agreement with Laplace's Equation [ADA67], is equal to

$$\Delta P = \gamma_L \left(\frac{1}{r} - \frac{1}{x} \right) \quad (5-6)$$

and γ_L is the surface tension of liquid, R is the radius of the adhering particle, r is radius of the meniscus, x is horizontal distance of intersection between the meniscus and the adhering particle, θ_1 is the contact angle of water with the particle, and α is the angle between the ordinate axis and a radius to the intersection of the particle with the liquid meniscus. The angle α may also be found by the arctangent of the slope of the particle surface at point x ,

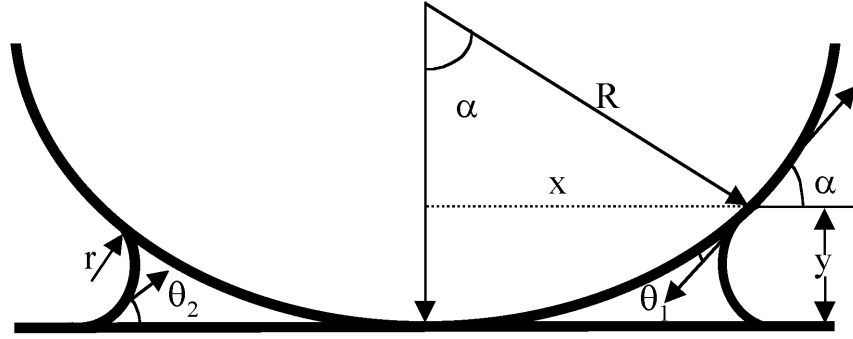


Figure 5-1: Capillary Schematic. Schematic illustration of the liquid annulus formed in a capillary created by the adhesion of an ideally smooth spherical particle to an ideally smooth flat substrate.

$$\alpha = \arctan\left(\frac{dy}{dx}\right) \quad (5-7)$$

The equilibrium radius of the meniscus, r , is given by Kelvin's equation [ADA67]

$$r = \frac{-V\gamma_L}{N_a kT \ln(P/P_s)} = \frac{-V\gamma_L}{kT \ln \psi} \quad (5-8)$$

where V is the molar volume of the liquid, γ_L is the surface tension of the liquid, N_a is Avogadro's number, kT is the product of Boltzman's constant and absolute temperature, P and P_s are the vapor pressure and saturated vapor pressure, and ψ is relative humidity.

The analytical formulae for the calculation of capillary force based on Eqs. (5-5 to 5-8) were suggested by Marmur [MAR93] and de Lazzari et al. [DEL99]. However, both works only describe the force as function of the horizontal distance, x , where the meniscus intersects the adhering particle. Unfortunately this value is not known experimentally. Additionally, to describe the dependence of the capillary force on roughness, the effect of separation distance between the particle and substrate must be determined. Figure 5-2 shows the geometry of a smooth spherical particle adhered to a rough flat surface in the presence of capillary condensation.

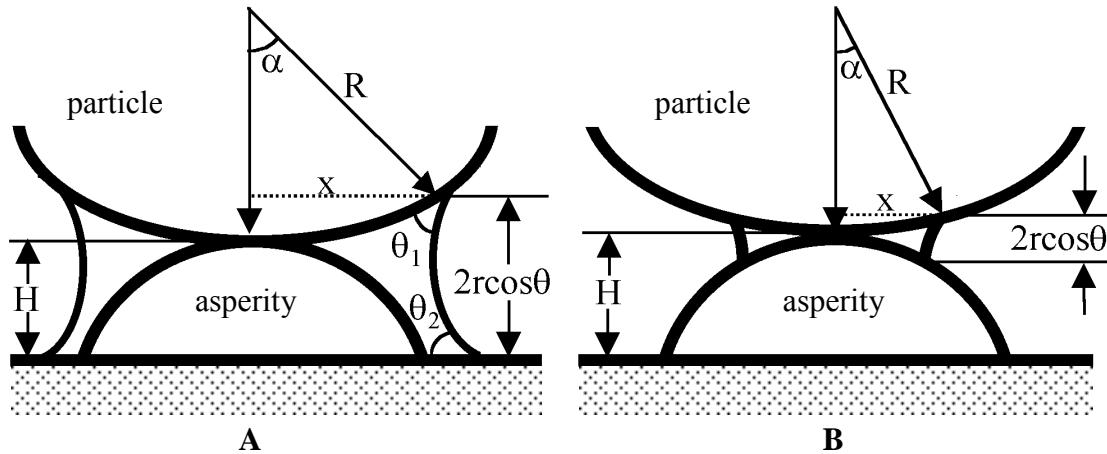


Figure 5-2: Particle/Asperity Capillaries. Schematic illustration of the meniscus formed in a capillary created by the adhesion of an ideally smooth particle to an asperity on a flat substrate for conditions in which the relative humidity is high, 2a, and for which the relative humidity is low, 2b.

For both high and low humidity ranges, Figure 5-2a and 5-2b, respectively, schematically describe the liquid annulus formed by capillary condensation. For high relative humidity (Figure 5-2a), to describe the vertical distance between the surface of the particle, at a point defined by the intersection of the meniscus with the sphere at distance x , and average surface plane, y , the following geometric relationship may be written

$$y = R + H - R \cos \alpha = r \cos(\theta_1 + \alpha) + r \cos \theta_2 \quad (5-9)$$

where R is the radius of the adhering particle, H is the separation distance between the bottom of the adhering particle and the average surface plane, α is the angle between the ordinate axis and a radius to the intersection of the particle with the liquid meniscus, r is the radius of the meniscus, and θ_1 and θ_2 are the contact angles of the particle and flat substrate, respectively.

Assuming that the volume of the liquid annulus to be small (i.e. x , y , and $r \ll R$),

Eq. (5-9) results in a quadratic equation, which may be solved for α to yield

$$\alpha = -\frac{r \sin \theta_1}{R} + \sqrt{\frac{r^2 \sin^2 \theta_1}{R^2} - \frac{2H - 2r(\cos \theta_1 + \cos \theta_2)}{R}} \quad (5-10)$$

Eq. (5-5), (5-6), (5-8), and (5-10) allow calculation of capillary force. An especially simplified solution is obtained for a small contact angle (θ_1 and $\theta_2 < 1$ rad)

where from Eq. (5-10)

$$\alpha^2 = \frac{2r(\cos \theta_1 + \cos \theta_2) - 2H}{R} \quad (5-11)$$

Additionally from Eqs. (5-5) and (5-6) it follows that

$$F_p = \pi \gamma_L x^2 / r = \pi \gamma_L R^2 \alpha^2 / r \quad (5-12)$$

Substituting α^2 from Eq. (5-11) in Eq. (5-12) the simplified equation for capillary force may be derived as

$$F_p = 4\pi \gamma_L R \cos \theta \left[1 - \frac{H}{2r \cos \theta} \right] \quad (5-13)$$

where

$$\cos \theta = \frac{\cos \theta_1 + \cos \theta_2}{2} \quad (5-14)$$

It should be noted that Eq. (5-13) is applicable only if $H \leq 2r \cos \theta$. In other words, that the liquid meniscus spans the distance from the particle to the average surface plane, Fig. 5-2a.

The separation distance between the adhering particle and the average surface plane, H , for spherical asperities with their centers located beneath the average surface plane has been shown previously, Eq. (5-4), to be approximated by $1.817RMS$. Hence, for a small annulus volume (compared to particle radius) and small contact angle (hydrophilic surface), the capillary force between sphere and flat rough samples can be calculated by Eqs. (5-4), (5-8), and (5-13). Note that in the development of this simplified

model of capillary adhesion, the effect of wetting films and the transition from a film to liquid annulus as described in detail by Derjaguin and Churaev [DER84, DER87] is not considered.

For the low humidity case (Figure 5-2b), when the equilibrium radius of the meniscus is very low, as described by the Kelvin equation, the liquid annulus is actually formed between two spheres, the particle and the asperity. For this situation, an effective radius, R_{eff} , should be considered, as described by Derjaguin et al. [DER34],

$$R_{\text{eff}} = \frac{2RR_1}{R + R_1} \quad (5-15)$$

where R is the radius of the adhering particle and R_1 is radius of the asperity. In the case when R is in the range of micrometers and R_1 is on the nanometer scale, the effective radius is quite small. As a result, very low capillary adhesion should be observed in the low relative humidity regime. Significantly greater capillary adhesion force would result once the relative humidity became high enough to produced an annulus that covers the asperity completely and spanned the distance to the average surface plane, as illustrated in Figure 5-2a. This situation leads to the concept of a critical relative humidity needed to first observe capillary forces.

A Critical Relative Humidity for Capillary Forces

For an ideally smooth sphere adhered to a smooth flat substrate ($r \rightarrow \infty$) at zero separation distance, the classic formula follows from Eq. (5-13)

$$F_p = 4\pi\gamma_L R \cos \theta \quad (5-16)$$

This relationship has no dependence on the relative humidity and, consequently, should have a fixed value even at zero percent relative humidity. Experimentally, this clearly is not the case [FIS81c, RAB91]. Therefore, there should be a point at which

capillary forces first start to appear and below which they are absent. There are at least two approaches to this problem. The first was suggested by Coelho and Harnby [COE78a, COE78b] and is based on the assumption of thermodynamic equilibrium between the liquid meniscus, bulk liquid in the annulus, and vapor. Equilibrium also necessitates that the liquid in the annulus is under greater pressure than that of the vapor. Otherwise, the liquid in the meniscus would boil. The critical values of relative humidity, obtained within this framework, are of the order of 70-99% relative humidity which are significantly higher than experimentally observed values [FIS81c]. This approach has also been challenged by the observation, during pore size distribution measurement for example, that nitrogen vapor can fill nanometer sized pores. However, in these pores the negative pressure can achieve several hundreds of atmospheres, according to Laplace's Equation, Eq. (5-6). A possible reason for this discrepancy is that the liquid in the pores may be supersaturated due to the lack of defects needed to initiate boiling.

A second approach to the problem of critical humidity was suggested by Rabinovich et al. [RAB91]. It was proposed that there is a certain annulus volume or dimension, below which, the adsorbed molecules can not be considered a macroscopic phase and, consequently, no surface tension or capillary force would exist at a humidity less than a critical value. The authors, after analysis of literature data detailing force measurements in the semi-miscible water/octamethylcyclotetrasiloxane mixtures between ideally smooth mica [CHR85, CHR87], and their own experimental results for butanol/water mixtures between silica surfaces, found that the critical radius of the meniscus corresponded to be approximately 1 nm.

Both of these approaches were suggested for ideally smooth solids. As follows from Eq. (5-13), there may be an additional criteria for the observation of capillary adhesion between surfaces with nanoscale roughness. An initial approach is that the critical relative humidity corresponds to the humidity at which the capillary force (described by Eq. (5-13)) is equal to zero. However, a more important characteristic is the point at which the capillary force exceeds the adhesion between the “dry” surfaces. At zero or low humidity, only a thin mono-molecular film exists on the surface which can not form a meniscus. In this situation Eqs. (5-1) and (5-2), developed for dry surfaces, are appropriate. Above the critical humidity, the capillary forces are expected to act in addition to the dry adhesive forces.

Of course this last point brings up an interesting consideration because the region of the surfaces in the liquid annulus are no longer acting through air but rather through liquid. This is important because the magnitude of van der Waals forces for solids through water, for instance, are generally significantly lower than in air. For example, the Hamaker constant of silica interacting through water is approximately 0.8×10^{-20} J [RAB90], which is 8 times less than the Hamaker constant of silica interacting through air, 6.5×10^{-20} J [RAB90]. In many cases the contribution of van der Waals force through the liquid annulus may be neglected.

To account for this condition, the integration procedure suggested by Derjaguin [DER34] whereby the interaction energies of rings of increasing radii on the flat surface with their corresponding areas on the adhered particle are summed to provide the net force of attraction, may be applied. Assuming that the net attraction within the annulus is small, the van der Waals attraction of the remaining dry surfaces, F_{dry} , is equivalent to a

sphere of equal radius but at a distance above the average surface plane equal to the height of the meniscus.

$$F_{\text{dry}}(H) = F_{\text{dry}}(H_0 + y) = \frac{AR}{6(H_0 + 2r \cos \theta)^2} \quad (5-17)$$

Where H_0 is shortest distance between the two surfaces, y is the maximum height of the meniscus, A is Hamaker's constant, R is the radius of the adhering particle, and θ is the contact angle. After a significant relative humidity has been achieved, the total force of adhesion between the two surfaces should be calculated as

$$F = F_C + F_{\text{dry}} \quad (5-18)$$

Where F_C and F_{dry} are calculated with Eqs. (5-13) and (5-17), respectively. Note that the radius of the meniscus and, therefore, the height in Eq. (5-17) increases in magnitude quickly with increasing relative humidity. Hence, it follows that at high relative humidity the contribution of van der Waals attractive forces becomes smaller and adhesion is principally dominated by the capillary force.

Experimental

Materials

Adhesion force was measured between 20-40 μm glass microspheres from Duke Scientific Corp. and a variety of substrates. The spheres were found to have an RMS roughness of less than 0.2 nm. Silica substrates included an oxidized, to approximately 180 nm, silicon wafer of 0.2 nm RMS roughness provided by Dr. Hans Arwin (Linköping University, Sweden); a plasma enhanced chemical vapor deposited (PE-CVD) 2 μm thick coating of 0.3 nm RMS roughness silica on silicon supplied by Motorola Company; and a sample of the PE-CVD silica boiled in a 1-1 mixture of hydrogen peroxide and ammonia

for 6 hours producing an RMS roughness of 0.7 nm. Images of non-etched and etched PE-CVD silica surfaces are shown in Figure 5-3a and 5-3b. Measurements were also performed between the spheres and a sapphire substrate (basal plane) supplied by MTI Corp. of 0.3 nm RMS roughness, a sputtered titanium surface deposited on silicon of 1.4 nm RMS roughness, and a sputtered silver surface of 3.0 nm RMS roughness both acquired from Motorola Corporation.

All silica, glass, and alumina surfaces were cleaned by rinsing in acetone and methanol followed by repeated rinsing and boiling in acidified deionized water for at least 8 hours. Cleaning was performed immediately prior to experimentation. Also before each experiment, particles were glued to tapping mode TESP rectangular atomic force microscopy (AFM) cantilevers, supplied by Digital Instruments Inc. using a low melting temperature resin, Epon R 1004f from Shell Chemicals Company.

Methods

Surface force was measured on a Digital Instruments Nanoscope IIIa according to the methods described by Ducker et al. [DUC92]. The sphere, attached to a cantilever of known spring constant, was positioned close to the flat substrate. Then, as the substrate was moved towards and away from the particle by a piezoelectric tube, the deflection of the cantilever was monitored by a laser that reflects from the top of the cantilever onto a position sensitive photodiode. In this manner, the force between the two surfaces as a function of separation distance was obtained. The force/distance profiles and values presented are normalized by dividing the measured force by the radius of the sphere. In other words, the data is presented in terms of energy per unit area of flat surfaces. This enables determination of the force for different geometries and sizes of particles as long

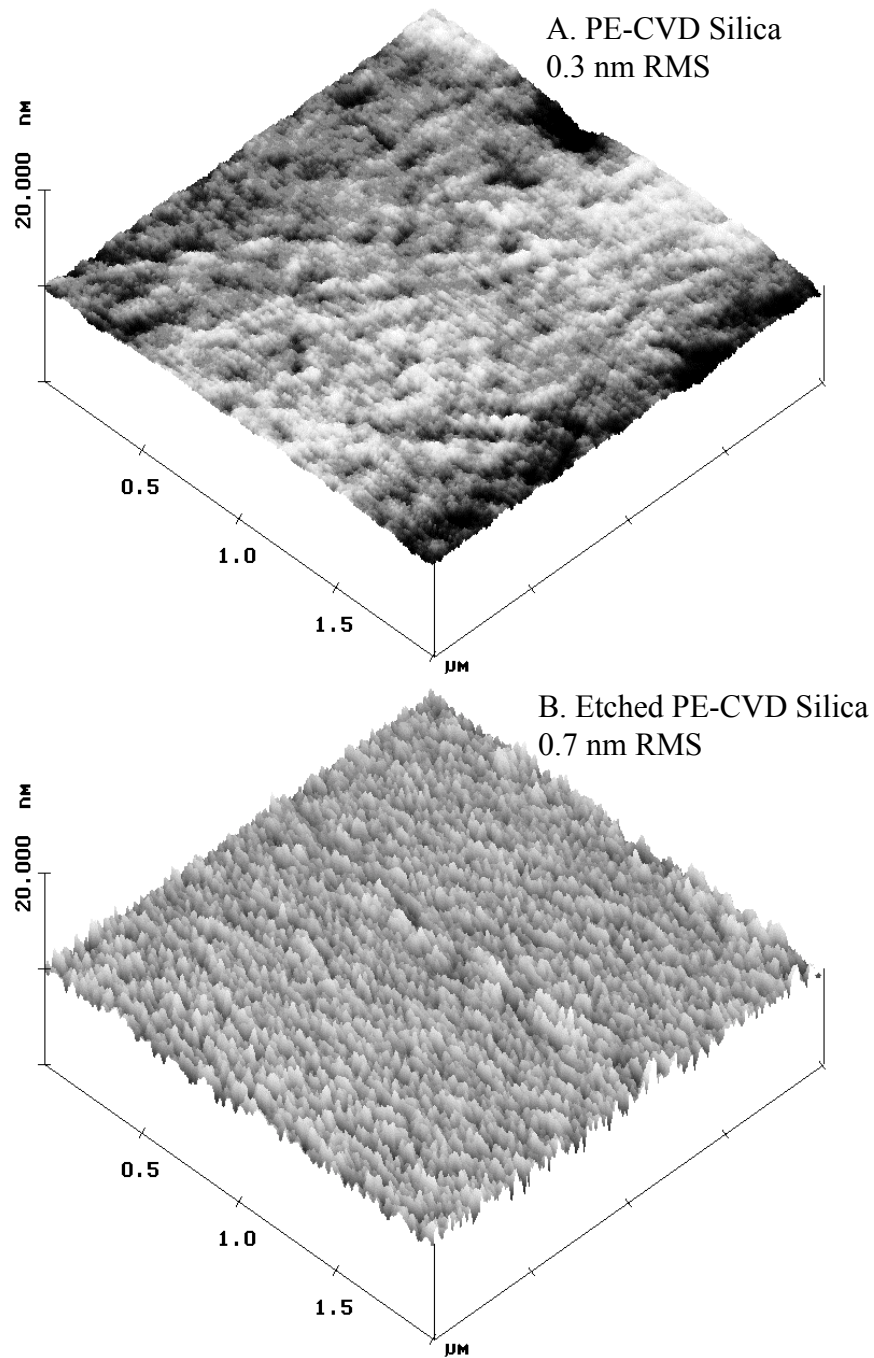


Figure 5-3: Morphology of CVD Silica Samples. Atomic force microscopy images of 2 x 2 µm areas with a total vertical scale of 20 nm (10 nm/division) of the rougher silica samples utilized in this investigation. Figure 3a is the PE-CVD silica and 3b is the PE-CVD silica etched in ammonia/peroxide solution. Images were taken using contact mode AFM.

as the range of the forces is much less than the particle's radius of curvature. Surface roughness was measured using contact mode AFM and images are presented without filtering.

To control the gaseous atmosphere, an environmental chamber was constructed that encased the entire AFM (without microscope). The chamber was fitted with a recirculating fan and the AFM was placed on a vibration isolation pad within the chamber. Relative humidity was monitored by two Fisher Scientific High Accuracy Thermo-Hygrometers located at the top and bottom of the chamber. In a typical experiment, the gaseous atmosphere within the chamber was saturated with water in dishes and then allowed to dry over time. To achieve low relative humidity, desiccant was opened or pure nitrogen gas was used to flush the chamber. Each reported adhesion data point is the average of at least 20 measurements taken at different locations on the surface.

The adhesion force was found to increase as a function of applied load and then become constant above a critical loading value. This suggests that a certain amount of pressure is necessary to bring surfaces into intimate contact and allow enough time for a capillary to form [ATA98]. In this system, an applied normalized load greater than approximately 2 N/m was found to produce relatively constant results and all adhesion data is reported after applying a load greater than this value.

Results and Discussion

A characteristic force/distance curve for the smoothest silica sample at 54% relative humidity is shown in Figure 5-4. Upon approach of the two surfaces, as separation distances become small, long range van der Waals attractive forces are

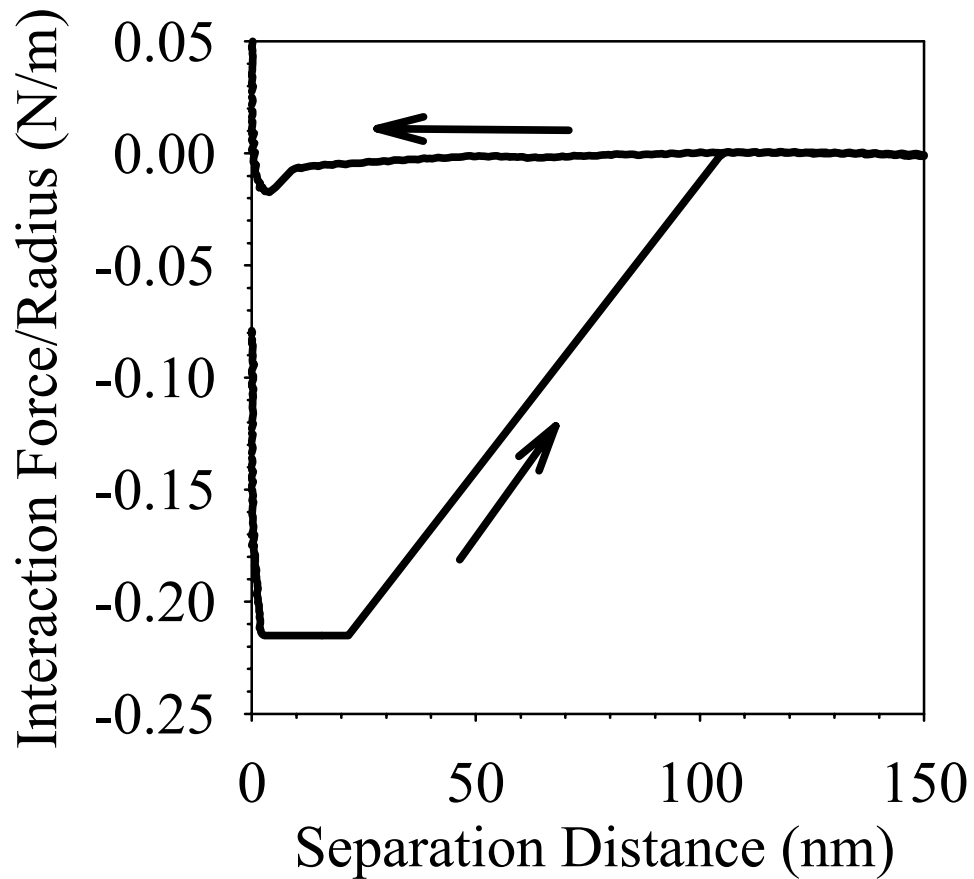


Figure 5-4: Approaching and Retracting Force Profiles. Typical approaching and retracting force curves for the glass sphere interacting with the oxidized silicon wafer sample at 54% relative humidity. Arrows indicate the direction of travel either approaching (leftward pointing arrow) or retracting (rightward pointing arrow).

observed to pull the sphere towards the surface starting at approximately 8 nm separation distance. When the gradient of the attractive forces becomes greater than the spring constant, the mechanical equilibrium of the cantilever is overcome and the sphere jumps into contact with the flat surface. After the point of contact, pressure is still applied to the surfaces up to a known load and then the surfaces are pulled apart from one another. Due to the magnitude of the adhesion forces, the particle attached to the tip of the cantilever

does not separate from the substrate as the cantilever starts to be pulled away. However, when the deflection force of the cantilever equals the force of adhesion, the sphere releases from the surface, and jumps to its equilibrium position. From the product of this distance and the spring constant of the cantilever, the force of adhesion may be obtained. This method is often necessary because, due to the limited range of the photodiode, evidenced by the flat portion of the retraction curve, the minimum in the retraction curve can not always be directly observed. However, for cases in which both the minimum and critical separation distance may be observed, the agreement between the two is good.

The dependence of adhesion force as a function of relative humidity for the silica samples of different roughness is given in Figure 5-5. Of interest first is the significant decrease in the magnitude of the adhesion force with an increasing surface roughness in the low relative humidity regime. It can be observed that a increase from approximately 0.2 nm to 0.7 nm in surface RMS roughness decreases the observed dry adhesion by over an order of magnitude. Note also that the adhesion between the smoothest samples results in a surface energy of 60 mJ/m^2 for JKR adhesion mechanics which is in the range reported in the literature [BRA32, YAM75, YAM98]. This general behavior of a regime where, as a function of relative humidity, there is no increase in the magnitude of the force of adhesion was found for all the silica samples. However, as expected for each sample, there is a critical relative humidity at which the force of adhesion begins to increase. Additionally, for each substrate, the transition does not result in a jump to a single adhesion value predicted by Eq. (5-16) for ideally smooth surfaces. Instead adhesion forces increases as relative humidity increases.

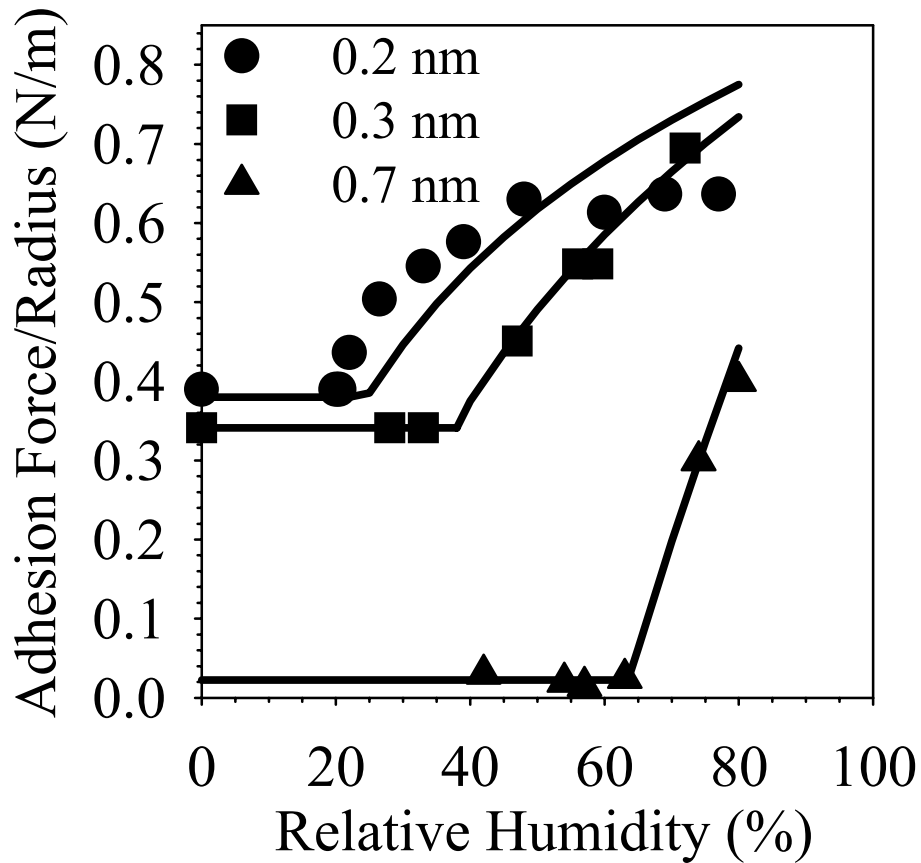


Figure 5-5: Adhesion Profiles for Silica. Force of adhesion as a function of relative humidity for silica surfaces of increasing roughness. Circles represent the oxidized silicon wafer (0.2 nm measured RMS roughness), squares represent the PE-CVD substrate (0.3 nm measured RMS roughness), and triangles represent the etched PE-CVD surface (0.7 nm measured RMS roughness). Also shown are theoretical predictions for both the dry adhesion and capillary adhesion regimes based on the information in Table 5-1.

the transition occurs at approximately 25% relative humidity, which is significantly lower than the 70-99% relative humidity predicted by the thermodynamic equilibrium model suggested by Coelho and Harnby [COE78a, COE78b]. As a result, it may be suggested that liquid inside the annulus is metastable rather than in thermodynamic equilibrium.

The minimum relative humidity for the onset of observable capillary forces corresponds to a radius of approximately 0.4 nm which coincides with the critical radius derived from the experiments of Fisher and Israelachvili [FIS81c] for water and cyclohexane vapors between mica surfaces. This value is comparable but smaller than the critical radius, 1 nm, found by Rabinovich et al. [RAB91] for nearly saturated solutions of water in butanol and by Christenson and coworkers [CHR85, CHR78] for water in octamethyl cyclotetrasiloxane. It may be possible that the geometry of the surfaces, their radii, the medium (vapor or solution), and condensate composition also has an impact on this critical radius.

Also presented in Figure 5-5 are the theoretical predictions of the dry (horizontal lines from Eq. (5-2)) and capillary forces (from Eq. (5-13)) for the silica surfaces. It appears that the relatively simple theoretical approach to the capillary adhesion between surfaces with nanoscale roughness reasonable predicts the experimental data. For all samples, a surface energy of 60 mJ/m^2 , a contact angle of 20° , and a surface tension of 72 mN/m was applied. The surface parameters and fitted values of surface roughness are presented in Table 5-1. Average peak-to-peak distances derived from Eq. (5-2) correspond adequately with those taken from the images of the surfaces and the measured adhesion values. Fitted values of the roughness, based on adhesion forces measured in the capillary regime, are also similar to measured values. Although roughness trends and general magnitude are easily discerned, there may still be error associated with background noise, imaging conditions, and uniformity of the substrates. Additionally, in reality there is a distribution of distances between asperities. To more accurately correlate experimental and theoretical predictions, these surface characteristics need to be more

accurately described. However, given the level of sophistication employed, the models are reasonably adequate.

The adhesion as a function of relative humidity for a number of other materials investigated in the present study is presented in Figure 5-6. The surface characteristics and fitting parameters are also detailed in Table 5-1. The shape of the curves are very similar to that of silica. As roughness increases, the dry force of adhesion decreases significantly, as predicted by Eq. (5-2). The relative humidity at which capillary forces begin to dominate the interaction also increases with increasing roughness, in agreement with Eq. (5-13). The absolute values of the forces also correspond well to those in the silica system indicating the importance of surface roughness in controlling adhesion over

Table 5-1: Substrate Characteristics and Adhesion Parameters. Characteristics of the substrates used in this investigation and the results of analysis by the proposed models.

Flat Substrate	Measured RMS Roughness (nm)	Average Peak- to-Peak Distance (nm)	Measured Dry Adhesion Force (mN/m)	Fit to Capillary Adhesion RMS Roughness (nm)
Oxidized Silicon	0.2	490	380	0.22
PE-CVD Silica	0.3	650	340	0.34
Etched PE- CVD Silica	0.7	130	23	1.20
Sapphire	0.3	250	150	0.38
Titanium	1.4	215	31	1.20
Silver	3.0	610	316	0.58

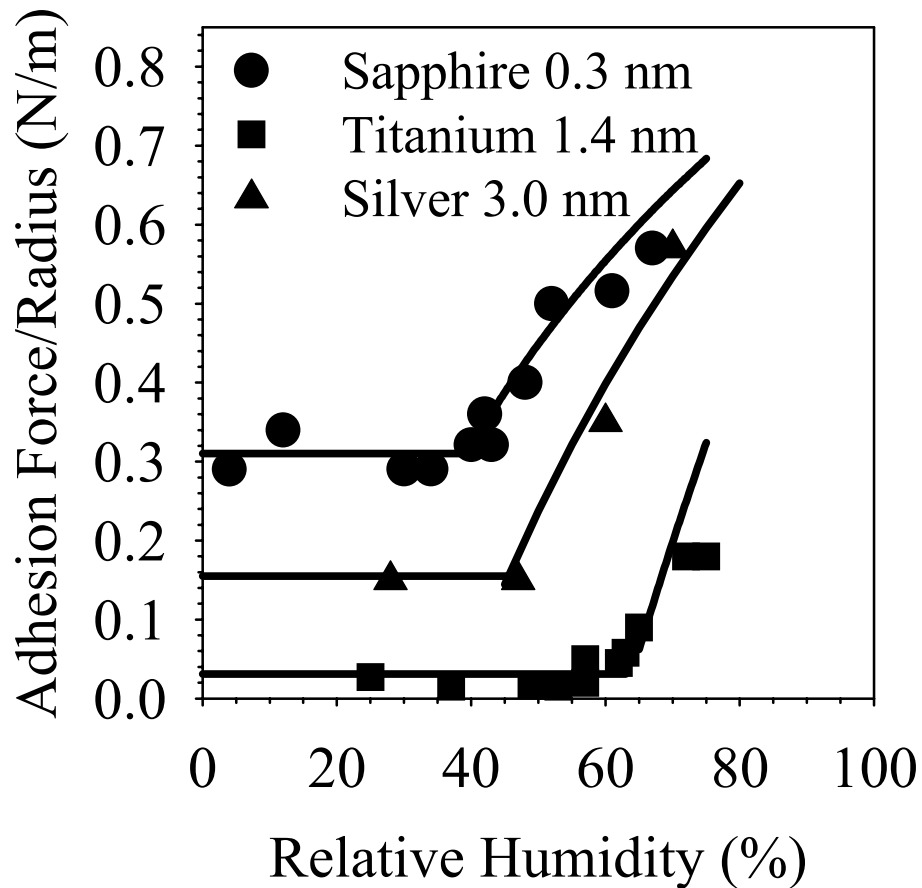


Figure 5-6: Adhesion Force Profile for Other Substrates. Force of adhesion as a function of relative humidity for substrates of sapphire (circles: measured RMS roughness of 0.3), titanium (squares: measured RMS roughness of 1.4), and silver (triangles: measured RMS roughness 3.0 nm). Also shown are theoretical predictions for both the dry adhesion and capillary adhesion regimes based on the information in Table 5-1.

other surface properties such as the Hamaker constant or polar forces. The model of capillary forces between surfaces with nanoscale roughness developed in this investigation is also in relative agreement with the experimental results of Quon et al. [QUO00] in which the adhesion of mica coated with rough gold layers, functionalized by surfactants, was measured.

The one material that did not behave as predicted in either the dry adhesion or capillary adhesion regimes was silver. Although the RMS roughness as measured by AFM was 3.0 nm, the capillary force model most closely fit to an RMS roughness of 0.53 nm. Similarly, in the dry adhesion region, it is seen that the magnitude of the adhesion force is significantly greater than expected for a surface with a 3.0 nm RMS roughness. Although the surface profile did not show any unusual characteristics, this contradiction may be understood if the higher plasticity of silver is accounted for. It is possible that asperities of this size combined with the relatively low yield strength of silver resulted in asperities under the adhering particle being plastically deformed. The deformation would result in a more intimate contact between the surfaces and increase the dry adhesion forces [SIN97]. The surfaces would also be allowed to come closer together such that the radius of the meniscus needed to observe capillary forces is lower.

It should be noted that the minimum critical relative humidity needed to observe capillary forces corresponds to approximately 25% for smooth surfaces. This value may either be explained by the minimum size of macroscopic liquid phase or by the effect of surface roughness in the range of 0.2 nm RMS. In this regime, it may no longer be appropriate to describe surfaces in terms of macroscopic parameters. Instead, atomic scale considerations may need to be developed for specific interfaces. In the case of greater roughness, it is clearly observed that the critical humidity is controlled by the surface roughness rather than the minimum possible radius of the liquid meniscus.

The adhesion forces presented in this investigation show sizable deviation from ideally smooth surfaces. This is significant considering that surface roughness was only varied by a few nanometers. These examples are meant to illustrate that even minuscule

surface roughness plays a major role in controlling the adhesion of surfaces. Many industrial powders and surfaces contain asperities that are significantly larger than explored here, but these data suggest that it may be the smallest scale of roughness that principally controls the interaction of surfaces whether they are in the dry or humid atmospheric regime. The formulas derived in this investigation are simplified, but even these basic approaches can elucidate the possible role of nanoscale roughness if the geometry of the surface is known.

Summary

In this chapter, a theoretical framework was developed to predict the magnitude and onset of capillary and dry adhesion forces in the presence of nanoscale roughness. This basic framework was validated with direct measurement of surface forces using atomic force microscopy. It is found that there is a significant decrease in dry adhesion force for a variety of surfaces with only an increase of RMS surface roughness of a nanometer or two. Similarly, capillary adhesion was also substantially lower in the presence of nanoscale roughness. In addition to this lower magnitude, the critical relative humidity, where capillary forces are first observed, increases as roughness on the nanoscale increases. Although other scales of roughness may be present on real surfaces, it is suggested that the smallest scale of roughness primarily controls the adhesion of surfaces.

In Chapter 6, the concept of a non-ideal interface will be expanded to describe the behavior of colloidal particles and surfaces in a aqueous environment. Instead of surface roughness dominating the interaction the effect of a layer changing in composition from the bulk solid material to that of the fluid will be explored. Although the mathematical

description is different from the preceding chapters, these systems once again will illustrate the importance of the true nature of the interface at the nanoscale when predicting bulk properties.

CHAPTER 6 INFLUENCE OF A TRANSITION LAYER ON INTERPARTICLE FORCE

Introduction

In previous chapters, the non-ideality of the surface has been modeled in terms of surface roughness. The chemical nature of the surface was not considered in detail. This may be appropriate for interactions in gaseous media because it is the real area in contact principally controls the adhesion. This is appropriate for most materials, especially hydrophilic dielectrics, which have similar Hamaker constants and polar force groups. The magnitude of both these interactions also decreases rapidly with increasing separation distance. Alternatively, In liquid media van der Waals forces are significantly weaker and particles are rarely in contact with each other. In these systems, attractive forces are often of the same magnitude as, for example, electrostatic or steric repulsive forces. Hence, small differences in magnitude or separation distance between the particles may have a significant impact on the ensemble behavior of a suspension.

In this chapter, the influence of a non-ideal solid/liquid interface will be discussed. The silica/water system will be used as a specific example of this phenomena. Direct measurement of surface forces has revealed that silica surfaces seem to have a short range repulsion not accounted for by classical DLVO theory. The two leading hypotheses for the origin of the non-DLVO force are either (i) structuring of water at the silica interface or (ii) water penetration into the surface resulting in a gel-layer. In this chapter, the interaction of silica surfaces will be reviewed from the perspective of the

non-DLVO force origin. In an attempt to more accurately describe the behavior of silica and glass surfaces, alternate models of how surfaces with gel-layers should interact based on the concept of a non-ideal interface are proposed. This non-ideal interface is shown to have a significant impact on the colloidal behavior of silica particles in aqueous solution and may have additional impact on other systems where the interface may not be atomically sharp.

Through colloid stability studies [ILE79, YOT93B] and direct measurement of surface force [RAB82], silica surfaces have been shown to exhibit large repulsive forces at relatively short distances (less than 10 nm) in aqueous solution. This force cannot be predicted by standard application of electrostatic repulsion and van der Waals attraction as described by the DLVO theory [DER41, VER48] and has not been found, so far, to occur between other surfaces such as mica [PAS83] alumina [DUC94, PED98], or titania [YOT93A]. Consequently, there has been much discussion in the literature as to the origin of these non-DLVO forces.

Two hypotheses have been proposed. The first suggests that the non-DLVO force is due to structuring of water at the silica surface (structural force) [DER74]. As a result of the more limited conformations available to the water molecules in the region very close to the surface, the total free energy is greater than in the bulk. Hence, when two similarly oriented layers overlap, repulsion is observed. This assertion has been supported by molecular dynamic [FOR97] and lattice simulations [BES97] demonstrating that bonding sites on surfaces may alter the structure of water in the first few layers.

The second proposed mechanism suggests that water molecules may dissolve or diffuse into and swell the silica surface (gel-layer) reducing the surface mechanical

properties [TAD68]. Hence, repulsion may be attributed to the strain of elastic deformation or to steric repulsion of silicic acid chains which to constitute the gel-layer. With either mechanism, the effect of these forces may have significant implications for rheological properties, colloid stability, selective reagent adsorption, filtration, and chemical mechanical polishing of both silica and materials related to silica.

Long Range Interaction Forces

Significant advances, such as confirmation of the general expressions of van der Waals attraction and electrostatic repulsion, have been made by measurement of the forces acting between silica and glass surfaces in air and aqueous media. The first direct measurement of interaction forces between approaching silica surfaces in aqueous solutions were made by Rabinovich et al. [RAB82] and Peschel et al. [PES82]. Since, studies have been performed with nearly all types of modern surface force measurement devices including the surface force apparatus [HOR89], atomic force microscope [DUC91], and interfacial gauge [YAM98] with relatively the same result. Due to an increasingly negative surface charge with increasing pH, an electrostatic repulsive force dominates the interaction at relatively large separation distances (approximately greater than 10 nm) and low electrolyte concentrations. At these separation distances, the measured forces have been fitted by DLVO theory under a variety of boundary conditions (constant potential [RAB82], constant charge [HOR89], and charge regulation [GRA93]). However, at small separation distances (approximately less than 10 nm) a strong repulsive force, that cannot be explained by standard application of DLVO theory, is observed along with minimal or no adhesion between the surfaces. A notable exception, to be discussed later, is the work of Yaminsky et al. [YAM98] and Vigil et al.

[VIG94] in which adhesion was observed and subsequently explained by the fusion of surfaces when pressed together.

Short-range repulsive forces have also been observed in other inorganic systems [PAS80, DUC94], but only above some critical electrolyte concentration. Additionally, the magnitude of repulsion and critical concentration of electrolyte needed (typically of the order of millimoles) is closely linked to the type and valency of ions in solution [PAS83]. However, in silica and glass systems the additional force does not seem to be strongly dependent on the type or concentration of electrolyte. In fact, a decrease in magnitude of the non-DLVO forces with increasing electrolyte concentration has been reported [YOT93, RAB82, COL98]. As a result of these investigations, it is generally assumed that the origin of the non-DLVO forces on silica is different than in other oxide systems.

Structuring of Water at the Silica Interface

Several authors have attempted to delineate the origin of the non-DLVO force in the silica system. Initial experiments focused on measuring the interaction of silica and glass surfaces at different pH and electrolyte concentrations. Although most measurements were qualitatively similar, differences such as surface potential at a particular condition still exist. As a result, the relative magnitude and extent of the repulsive forces in the silica systems were determined but little could be said about their origin. Some of the variations in these early results may be attributed to the fact that a variety of amorphous silicas and glasses of different thermal history and compositions were used and that surface preparation procedures are not standardized. Most authors achieved a high level of cleanliness in their experiments with respect to organic and

particulate contamination but in doing so often neglected the possible changes in the actual surface of the silica or glass. For example, with differing calcination temperatures and times not only will the number of silanol groups on the surface change, thus affecting contact angle and surface potential [GRA93], but the type and strength also are expected to change [LIU96]. Additionally, at very high temperatures ($>900^{\circ}\text{C}$) strained ring structures are reported to form in glasses thus further changing the number, strength, and dissociation constants of the silanol groups [GRA95].

Few authors [GRA93, FIE96, KAM98] have attempted to determine the origin of the non-DLVO force by directly comparing similar surfaces treated in different manners. Kamiya [KAM98], for example, measured the force between an AFM tip and sol-gel derived monoliths prepared by different methods. By increasing the water to organosilane precursor ratio, silica gels with surfaces hydrated to various extents, as characterized by FT-IR, were produced. It was found that the additional repulsion increased as the hydroxyl concentration of the surface increased. Sol-gel derived structures are actually aggregates of nanometer scale spheres. Through various sol-gel techniques the size of these spheres was also varied. It was found that as the size of the spheres comprising the gel decreased below approximately 7 nm, the additional repulsion disappeared. This effect was attributed to the angles and spacing of the hydroxyl groups on the surfaces, due to the radius of curvature being too large to create a structured water layer. While these results support the hypothesis of a structured water layer, a rigorous interpretation is difficult because the surfaces used were not regular or smooth and the interacting body was silicon nitride of unknown radius.

Fielden [FIE96] measured forces between a glass sphere and oxidized boron doped silicon wafer that had either been rehydroxylated with water plasma or heat treated at 1050°C and then exposed to a short burst of “dry” argon plasma leaving the surfaces with a contact angle of approximately 45°. He observed differences in the force curves due to surface charge but did not attempt to determine whether the changes affected the non-DLVO forces or the dissociation constants of the remaining silanol groups (charge regulation parameters).

Finally, in one of the more extensive studies, Grabbe et al. [GRA93] used the surface force apparatus to measure the force between nearly pure amorphous sheets of silica that had been flame polished (contact angle $\cong 45^\circ$), steamed (contact angle $\cong 0^\circ$), and exposed to ammonia vapor (contact angle $\cong 0^\circ$). Forces were then measured as a function of electrolyte concentration and charge regulation parameters extracted. Differences in surface charge were noted with the steamed surface exhibiting a slightly higher surface charge than the flame polished surface. The ammonia etched surface, however, showed a surface charge at low ionic strength that was approximately twice that of the steamed sample. This increase was attributed to the formation of a gel-layer on the silica surface when exposed to a strong base. It was noted however, that within the accuracy of the experiments, the existence of this gel-layer or the steaming process did not significantly affect the magnitude of the non-DLVO forces. As a result, it was concluded that the additional repulsion was not primarily affected by the treatment of the surface but that the presence of a silica surface was all that was required to induce the non-DLVO force.

As mentioned previously, molecular dynamic and lattice simulations have also been performed which predict that some sort of longer range order should be present if the initial layer of water is oriented by the surface [FOR97, BES97]. Using lattice theory, Besseling [BES97] showed that a surface comprised of various ratios and numbers of electron donors or acceptors could result in water structuring (hydration) or depletion from a surface (hydrophobicity) and that these could result in non-DLVO repulsion or attraction. The hydroxylated silica surface at low pH is comprised primarily of electron acceptors (hydroxyl groups) and as such would be expected to structure water, resulting in a repulsive force. However, none of these theoretical techniques can currently make reliable predictions of the magnitude of the hydration force at a given separation distance.

Gel-Layer Formation

In the glass corrosion [COO90] and silica synthesis literature [ILE79, BRI90], it has been proposed that, as part of the dissolution process, water may break silicon/oxygen bonds and form hydroxylated surfaces. Upon longer periods of contact, some bonds of the silica tetrahedral supporting these structures may also be broken and begin to form silicic acid chains. The maximum length of these chains is subsequently determined by the kinetics of the dissolution process and the probability of breaking the links in the silicic acid chain. Eventually, as the solution reaches saturation, the silica surface is thought to consist of a distribution of these chains in equilibrium with reprecipitated silica from the solution. While these mechanisms form the basis for silica synthesis and corrosion, these are commonly observed only at relatively high pH because hydroxyl groups in solution are necessary to catalyze the reaction between water and the

silicon/oxygen bond. At the mid pH range (~ 2 to 9), these reaction mechanisms are relatively slow.

Recently, however, other authors have suggested that these reactions may also have significant implications in the mid pH regime. Both Vigil et al. [VIG94] using the surface force apparatus and Yaminsky et al. [YAM98] using the interfacial gauge technique report an adhesion force that develops upon contact of glass surfaces even under low ionic strength conditions. It is suggested that due to the constant breakage and reformation of the silica network, the surface may actually fuse together even in medium pH solution and that the kinetics of this reaction are relatively fast.

The authors differ, however, on how best to explain the additional repulsion upon approach of surfaces. Vigil et al. [VIG94] attempted to minimize the region of the non-DLVO force by shifting the start of the electrostatic forces, but not the van der Waals force outwards from the surface to account for the thickness of the suspected gel-layer. By this method, the experimentally measured values were fitted to distances as low as approximately 1 nm. However, surface forces are still measured even inside the area of the suspected gel-layer. Why no increase or change in slope in repulsion occurs for these data points with this method of analysis is not yet clear.

Yaminsky et al. [YAM98] utilized a different approach to minimize the unexplained portion of the experimental data. They simply proposed that van der Waals attraction should be neglected in the silica system. Under this assumption the experimental data was fitted to distances less than 1 nm. It is important to note that, in the data presented, scattering becomes significant at lower force levels and as such, much of the long range electrical forces are eliminated. This could possibly create an artificially

good fit. Also contradictory to the assumption of a near zero van der Waals force is the fact that Zhmud et al. [ZHU2000] at low pH (~ 3), as well as Horn et al. [HOR89], Meagher [MEA92], and Fielden [FIE96] at high electrolyte concentration (>0.1 M) have shown what appear to be the effect of apparently normal attractive van der Waals forces as surfaces approached one another.

While both existing water structure and gel-layer models may be used to explain the presence of an additional force, neither currently accounts for the attraction observed between silica surfaces under the above conditions. The remainder of this chapter will attempt to more accurately describe the behavior of silica and glass surfaces using alternate models of how such non-ideal surfaces may interact. It should be noted that, due to a lack of theoretical understanding and physical evidence other than force measurements, structural forces have often been employed when simple explanations fail to explain observed phenomena. The analysis that follows does not rule out the possibility of structural forces but rather offers an alternative explanation, based on current understanding.

Forces between Surfaces with Transition Layers

In agreement with previous attempts to model surfaces with gel-layers, it is assumed that the origin of the electrostatic forces is concurrent with the outer edge of the gel-layer. However, in difference to some of the previous models, it is assumed that the force needed to deform the gel-layer is far in excess of the forces applied during surface force measurement. As a result, steric based repulsion is not considered. This model is appropriate if the silica surface does not consist of long silicic acid chains under these mid pH conditions, but rather that the silica surface is merely swelled with water. The

primary reason for this assumption is that potentiometric titrations performed on silica indicate that the number of hydroxyl groups in acidic environments [TAD68] closely corresponds to the number of hydroxyl groups under dry conditions [ZHU87]. Which in turn, match closely with the theoretically predicted value for glass surfaces [LIU96]. These investigations suggest that a significant number of Si-O-Si bonds are not broken in the presence of acidic aqueous solutions and thus the silica surface should be treated as a hard surface. Since electrostatic forces are not expected to change and steric forces due to silicic acid chains are not being considered, the role of van der Waals attractive forces needs to be investigated in more detail in the presence of gel-layers.

The simplest model is to assume that the gel-layer is so diffuse, in terms of silica, that the Hamaker constant is effectively zero. As a result, van der Waals force should either be shifted to the start of what should be considered bulk silica as in Vigil et al. [VIG94] or neglected entirely as by Yaminsky et al. [YAM98] depending on the thickness of the gel-layer. However, as stated earlier, neither of these methods can account for attraction between silica surfaces. The concept that the repulsive non-DLVO force is not an additional repulsion at all but rather a lack of attraction by van der Waals forces as implied in these works is not without merit. To utilize this concept additional theory must be developed.

Homogeneous Gel-Layer

The above models require no modification to the distance dependent properties of the van der Waals force. However, if van der Waals attraction were to decrease as surfaces approached each other, a similar effect on the non-DLVO repulsive force could be achieved. As described below, a thin gel-layer on the order of nanometers, could

produce this effect. At large separation distances (> 10 nm for example) the contribution of the gel-layer to the overall van der Waals attraction would be small and surfaces would behave as predicted by DLVO theory. However, since van der Waals force is proportional to separation distance squared, the effect of gel-layer becomes more significant at lower separation distances. Hence, at very close surface separations, the van der Waals force may be entirely dominated by the gel-layer. Considering that the Hamaker constant of the gel is lower than that of the pure silica, the net attraction will be reduced.

This requires that an effective Hamaker constant that varies as a function of separation distance. As a first approximation, the gel-layer may be treated as a homogenous coating of fixed Hamaker constant between that of silica and water, as shown schematically in Figure 6-1. The theoretical calculation of the effective Hamaker constant for multi-layer systems is a complex task, but was much simplified by introduction of the method of surface plasmons, developed by Casimir [CAS48b] and van Kampen et al. [VAN68] which has been shown to be equivalent to the full Lifshitz derivation. Using this approach, Ninham and Parsegian [NIN70b] derived an analytical equation for disjoining pressure in a five layer system (corresponding to Figure 6-1) with a gel-layer of thickness δ . Integrating the disjoining pressure yields the specific energy of van der Waals interaction between two flat surfaces, E_{vdW} , as a function of separation distance, H ,

$$E_{vdW}(H) = -\frac{1}{12\pi} \left[\frac{C}{H^2} + \frac{D}{(H + \delta)^2} + \frac{E}{(H + 2\delta)^2} \right] \quad (6-1)$$

where $C = A_{232}$, $D = -2A_{123}$, and $E = A_{121}$. A_{ijk} are the Hamaker constants describing the interaction between materials i and k through medium j and the subscripts themselves

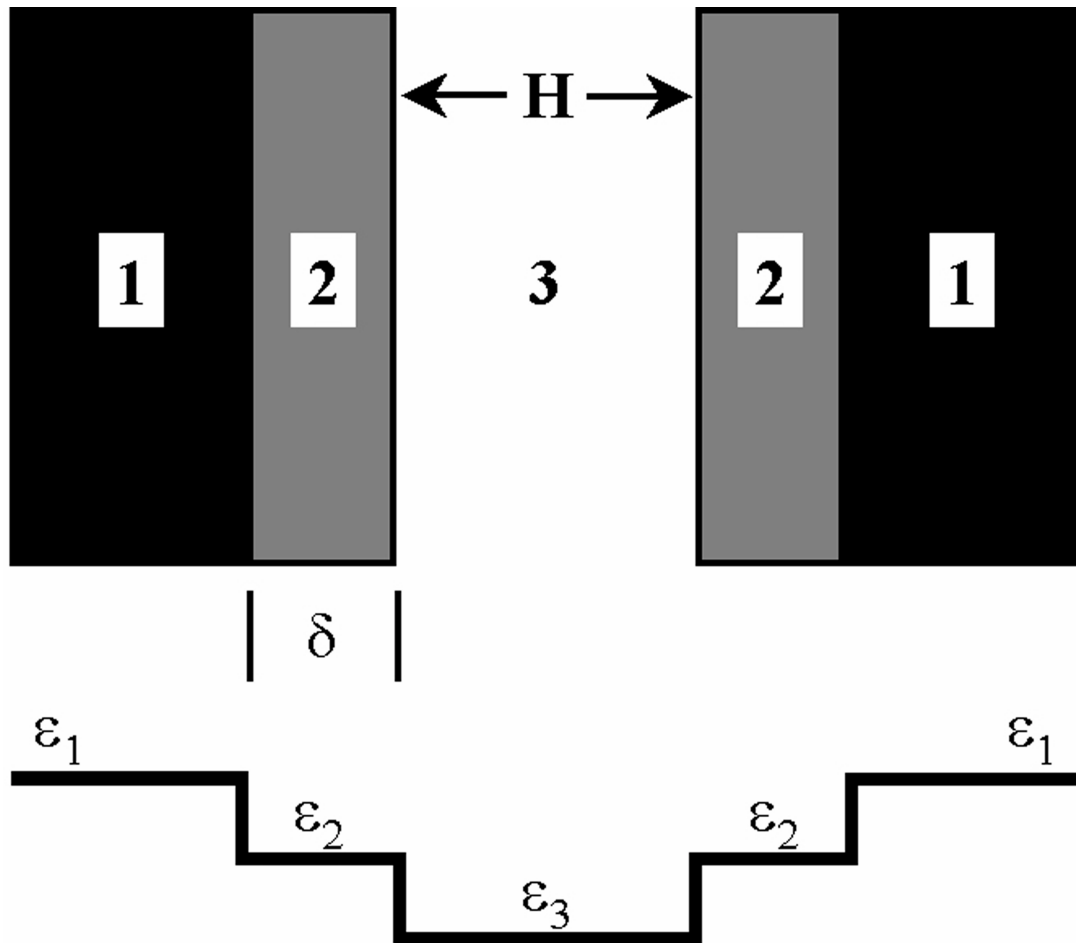


Figure 6-1: Five Layer Ideal Interaction. Schematic diagram of a five layer model with homogeneous gel-layers. Material 1 is the bulk solid. Layer 2 is the homogeneous gel-layer of thickness δ , separated by distance H . Region 3 is the intervening solution. The corresponding dielectric permittivities (ϵ_1 , ϵ_2 , and ϵ_3), schematically shown below the Figure, also change as a step function at each interface.

refer to the layers depicted in Figure 6-1. Note, that the interaction force may be calculated for other geometries through the application of Derjaguin's approximation. This solution was further expanded with more rigorous boundary conditions by Langbein [LAN72, LAN74] for any number of layers. For a five layer system, the overall equation

is the same as Eq. (6-1), but in Langbein's model C, D, and E have different functional forms and are significantly more difficult to apply in standard practice.

Gel-Layer with an Exponential Compositional Decay

In the models mentioned above, the proposed gel-layer is assumed to have a specific Hamaker constant implying a uniform homogeneous composition. For many systems, this model is not appropriate. For example, if the gel-layer on silica is a result of diffusion of water into the silica tetrahedral network, a smooth transition in composition from bulk silica to bulk water could be envisioned. To simplify calculation and to apply this model to the silica system, it is suggested that the dielectric permittivity at any given position in the gel-layer be proportional to composition with the components being pure water and pure silica.

With this assumption, the gel-layer becomes similar to the model developed by Parsegian and Weiss [PAR72] for the case of oil droplets in a semi-miscible solvent (water). For this interaction, the transition layer (gel-layer) was modeled as a layer of thickness δ of continuously changing composition from one interface to the other as shown in Figure 6-2. Using this model, the van der Waals force for semi-infinite planes through a liquid media in the presence of a compositional gradient between the two phases was calculated by solving Maxwell's equations for electric displacement with the following assumptions and conditions: 1. non-retarded limit of van der Waals force (relatively small separation distance); 2. non-metallic interacting materials (low Hamaker constant); 3. composition and dielectric permittivity follow an exponential decay distribution from one pure material to the other; 4. symmetric system (interaction of identical materials).

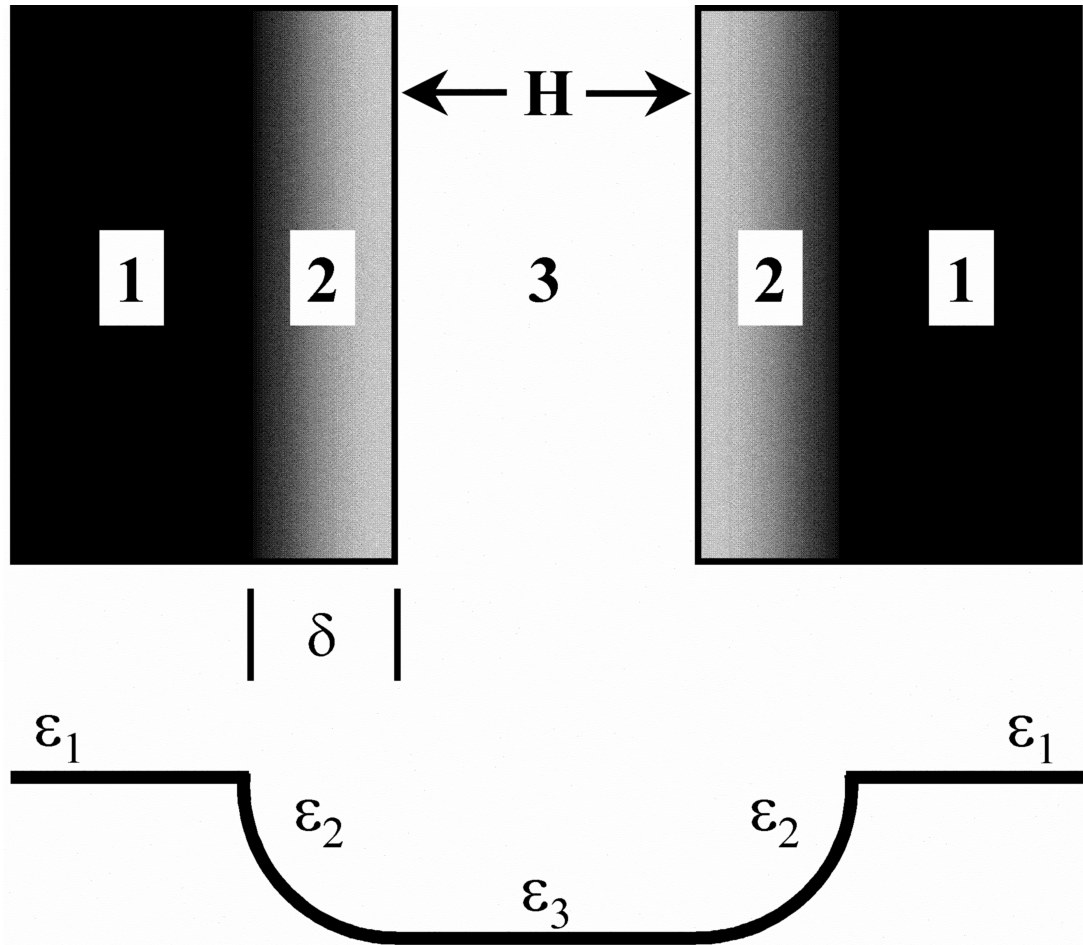


Figure 6-2: Five Layer Non-Ideal Interaction. Schematic diagram of a five layer model, similar to Figure 6-1, but with smooth transitions at each interface. Composition of the gel-layer changes exponentially from bulk silica to bulk water. The dielectric spectra of layer two is no longer a constant but varies between that of pure silica and pure water depending on position.

The third assumption may be written as

$$\varepsilon_2(z, i\xi) = \Gamma(\xi) \exp(-\lambda(\xi)|z|) \quad (6-2)$$

where ε_2 is dielectric permittivity of the gel-layer as a function of position z and imaginary frequency, $i\xi$. Γ is a coefficient and λ is the reciprocal decay length of the exponential function that defines the composition. Assuming a smooth composition gradient from one material to another, Parsegian and Weiss for and oil/water transition

layer were then able to develop a relationship between λ and the thickness of the gel-layer, δ .

$$\lambda(\xi) = (1/\delta) \ln(\epsilon_3(i\xi)/\epsilon_1(i\xi)) \quad (6-3)$$

Where ϵ_1 and ϵ_3 are the dielectric permittivities of the bulk material and water, respectively.

The authors then derived Γ as a function of ϵ_1 and ϵ_3 , so that the function $\epsilon_2(z, i\xi)$ is dependent only on the dielectric properties of materials 1 and 3. This approximation, decreases the number of variables needed to calculate the van der Waals force, hence, simplifying the calculation while retaining many of the features that can not be predicted by the homogeneous layer models. Parsegian and Weiss used the assumptions and the distribution of ϵ_2 defined by Eqs. (6-2) and (6-3) to determine the van der Waals interaction of droplets of hydrocarbon oil in water. The following equations for the effective Hamaker “constant”, A_{eff} , were obtained by Parsegian and Weiss [PAR72] with above-mentioned limitations

$$A_{\text{eff}}(H, \delta) = 1.5kT \sum_{n=0}^{\infty} \int_0^{\infty} x \ln[1 - \Delta_c^2(i\xi_n, x) \exp(-x)] dx \quad (6-4)$$

where

$$\Delta_c(i\xi_n, x) = \frac{\theta \left(1 - \exp\left(-\sqrt{\theta^2 + \frac{\delta^2}{H^2} x^2}\right) \right)}{\left(\frac{\delta}{H} x + \sqrt{\theta^2 + \frac{\delta^2}{H^2} x^2} \right) \left(1 - \exp\left(-\sqrt{\theta^2 + \frac{\delta^2}{H^2} x^2}\right) \right)} \quad (6-5)$$

$\xi_n = 2\pi n kT/\hbar$, and $\theta(\xi_n) = \lambda(\xi_n) \delta$. In the above formulas, A_{eff} is the effective Hamaker constant, H is separation distance, δ is the gel-layer thickness, kT are Boltzmann’s constant and temperature respectively, n is the whole number set, x is an integration variable, and \hbar is the reduced Plank’s constant.

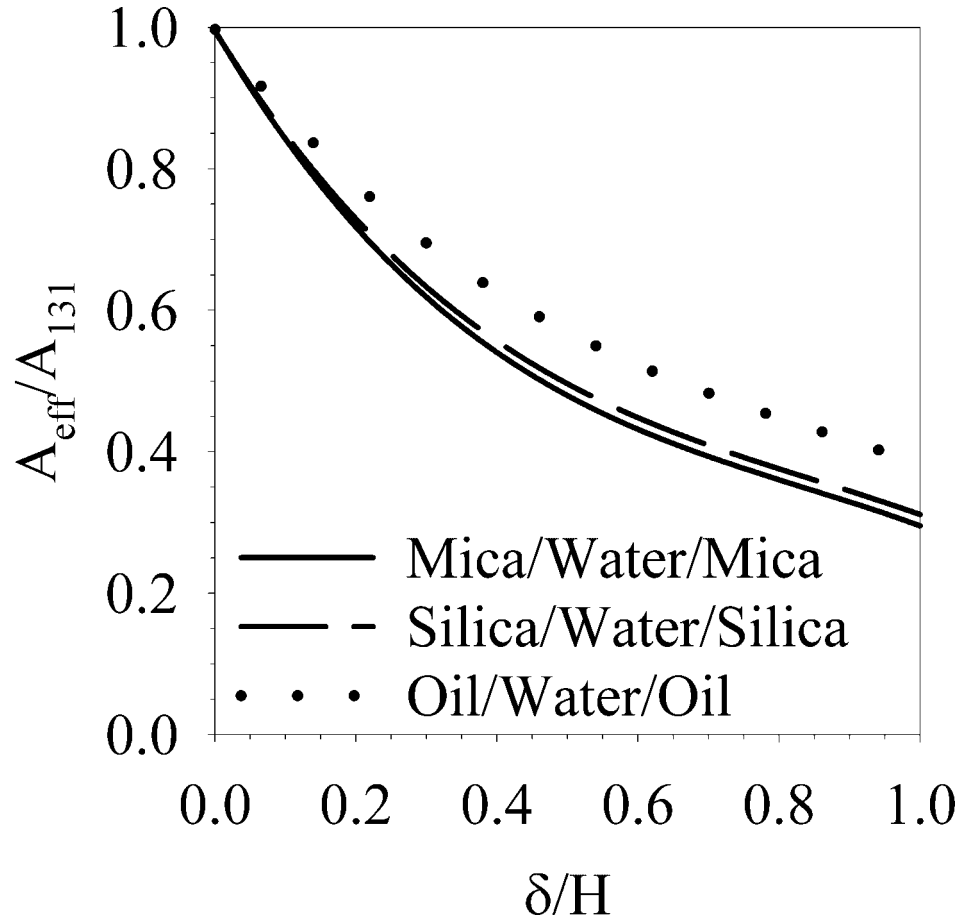


Figure 6-3: Effective Hamaker Constant. The effective Hamaker constant, A_{eff} , normalized by the bulk Hamaker constant, A_{131} , calculated using the dielectric spectra of mica/water/mica (solid line), silica/water/silica (dash dot line), and oil/water/oil (dashed line), with transition layers, interact through water as a function of the ratio of the gel-layer thickness, δ , to separation distance, H . As δ/H approaches zero, the effective Hamaker constant equals that of the bulk material, corresponding to large separation distances. The effect of a gel-layer on the effective Hamaker constant for materials with different properties is remarkably similar.

The numerical computer solution of A_{eff}/A_{131} as a function of the ratio of transition layer thickness over separation distance is shown in Figure 6-3 for the hydrocarbon/water/ hydrocarbon, mica/water/mica, and silica/water/silica systems. Based on the dielectric spectra used in this investigation, if the thickness of the transition layer, δ , was zero, A_{131} for oil, silica, and mica through water is 5.7×10^{-21} , 14.2×10^{-21} , and

26.5×10^{-21} J, respectively. Note, that these values were based on specific dielectric spectra and thus may vary from those reported elsewhere, but all are close to reported values including that of silica which matches well with the value of 12×10^{-21} J measured experimentally for glass fibers [RAB82]. It is also interesting to note that even though oil, silica, and mica are quite different materials with absolute Hamaker constants, A_{131} , varying by a factor of five, the dependence of the normalized Hamaker constants on gel-layer thickness and separation distance are very similar. For practical application of the effective Hamaker value an analytical solution is desirable. Hence, for each system a best fit to the results obtained by numerical integration was performed. The relative effective Hamaker constant of all three systems could be adequately described by an equation of the form

$$\frac{A_{\text{eff}}}{A_{131}} = a \cdot \exp\left(-b \frac{\delta}{H}\right) + c \cdot \exp\left(-d \frac{\delta}{H}\right) \quad (6-6)$$

where a, b, c, d are fitting values given in Table 6-1 for each system.

Table 6-1: Fitting Parameters for the Relative Effective Hamaker Constant. Values of the fitting parameters used in Eq. (6-6) to describe the distant dependant properties of the relative effective Hamaker constants calculated for the oil/water/oil, silica/water/silica, and mica/water/mica systems shown in Figure 6-3.

Parameter	System		
	Oil/Water/Oil	Silica/Water/Silica	Mica/Water/Mica
a	0.3961	0.4980	0.5114
b	2.6574	2.9099	3.0128
c	0.6037	0.5009	0.4878
d	0.5185	0.5437	0.5630

In the remainder of this study, the above relation for the silica/water/silica system will be utilized to more clearly establish the possible role of a gel or transition layer on the interaction of surfaces. This will be accomplished by directly comparing experimentally measured interaction force curves with the above proposed theories.

Experimental

Materials

Interparticle forces were measured between a plain glass microscope slide, Fisherfinest from Fisher Scientific Inc., and a 30-40 μm glass microsphere from Duke Scientific Corp. Both were found to have a root mean squared surface roughness less than 0.5 nm as measured by atomic force microscopy. Deionized water was produced by a Continental Water Systems Corp. system had a specific conductivity of $\sim 0.4 \mu\text{S}/\text{cm}$ and a natural pH of 5.8. All chemicals were provided by Fisher Scientific Inc. and were at least ACS reagent grade.

All glass surfaces were cleaned by rinsing in acetone and methanol followed by repeated rinsing with concentrated nitric acid and deionized water. After which they were boiled in acidified (pH 2-4) water for 24 hours. Such a treatment has been reported, for the Fisherfinest slides, to result in a surface that is primarily silica [FU98]. Cleaning was performed immediately prior to experimentation. Also before each experiment, particles were glued to triangular AFM cantilevers supplied by Digital Instruments Inc. (200 μm long, thick legged) using a low melting temperature resin, Epon R 1004f from Shell Chemicals Company.

After the boiling treatment, some surfaces were subsequently heat treated at 600°C for 24 hours. This treatment is expected to eliminate any physically adsorbed water on or in the glass surface. Additionally, treatment at temperatures greater than 500°C has been shown to significantly decrease the density and change the type of silanol groups on the silica surface [ARM69]. Hence, it is expected that a gel-layer on the treated sample would be thinner than the boiled surfaces, or non-existent.

Methods

Surface force was measured on a Digital Instruments Nanoscope IIIa in a fused silica liquid cell according to the methods described by Ducker et al. [DUC91]. The glass sphere attached to a cantilever of known spring constant was positioned close to the flat glass plate. Then, as the plate was moved towards and away from the particle by a piezoelectric tube, the deflection of the cantilever was monitored by a laser that reflects from the top of the cantilever onto a split photodiode. The force between the two surfaces as a function of separation distance was obtained. The force/distance profiles presented are normalized by dividing the measured force by the radius of the sphere, in other words the data is presented in terms of energy per unit area of flat surfaces. This enables determination of the force for different geometries and sizes of particles as long as the range of the forces is much less than the radius of curvature. The electrostatic force is extremely sensitive to small changes in electrolyte concentration. Hence, the specific conductivity of all solutions was measured in order to calculate the precise ionic strength. As a result, in fitting the electrostatic forces, the only variable parameter becomes the Stern potential at infinite separation.

Results

Figure 6-4 shows the total measured interaction force between glass surfaces in 2.5×10^{-4} and 1.0×10^{-3} M KCl solutions at pH 4 for the boiled surfaces. Figure 6-5, presents force profiles of the heat treated surfaces for 2.4×10^{-4} and 0.85×10^{-3} M KCl also at pH 4. At pH 4 electrostatic forces are relatively small compared to those at higher pH and as such, the non-DLVO forces are more discernible. Considering that the inaccuracy in fitting the electrostatic dominated part of the force curve increases as surface charge decreases and a region of net attraction is undesirable as it may lead to mechanical instability of the cantilever (jump in); the pH needs to be kept somewhat higher than the isoelectric point (approximately pH 2). In this manner, the interaction force can be fitted, while maintaining high sensitivity to the region in which the non-DLVO forces exist.

Electrostatic repulsive forces and Stern potentials were determined by fitting the measured interaction force profiles using the algorithm of Chan et al. [CHA80] with a constant surface charge boundary condition. To avoid complications from the region of non-DLVO forces, the measured force interactions were fitted to theory at distances greater than 20 nm. At least 10 measurements were made under each condition at different locations on the glass substrate. Due to instrument sensitivity, the fitting of the region of constant compliance (zero separation distance), and using the ionic strength determined by conductivity measurements, the fitted Stern potential was found to vary by ± 2 mV.

As expected for both boiled and heat treated surfaces, Stern potential decreases in absolute magnitude with increasing ionic strength. In the case of the boiled system from -24 to -17 mV and between the heat treated surfaces the potential decreases from -33 to

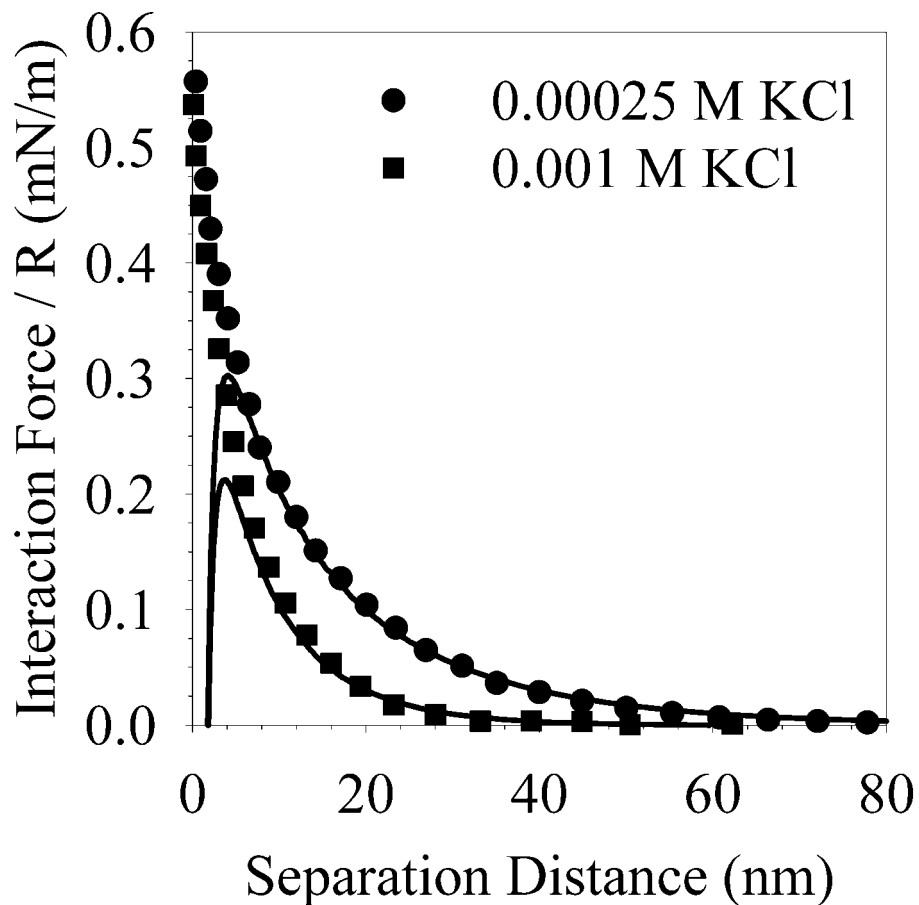


Figure 6-4: Interaction Force Profile between Boiled Surfaces. Experimentally measured force profiles for boiled glass surfaces at pH 4 in 2.5×10^{-4} and 1.0×10^{-3} M KCl solution. Curves were fit using the standard application of non-linear DLVO theory with a constant charge boundary condition, a Hamaker constant of 12×10^{-21} J, and non-retarded van der Waals forces. This procedure yielded a Stern potential at infinite separation distance of -24 mV for the lower ionic strength solution and -17 mV for the higher ionic strength solution.

-22 mV. Measurements at pH 6 and pH 9 were also performed for both systems but are not presented graphically here. Trends in Stern potential are similar to those at pH 4. For the particular glass plates and spheres used, the Stern potential even at pH 9 was lower than other reported values for pure silica indicating that the surface may still retain some of the characteristics of the glass. The potentials were, however, consistent over several

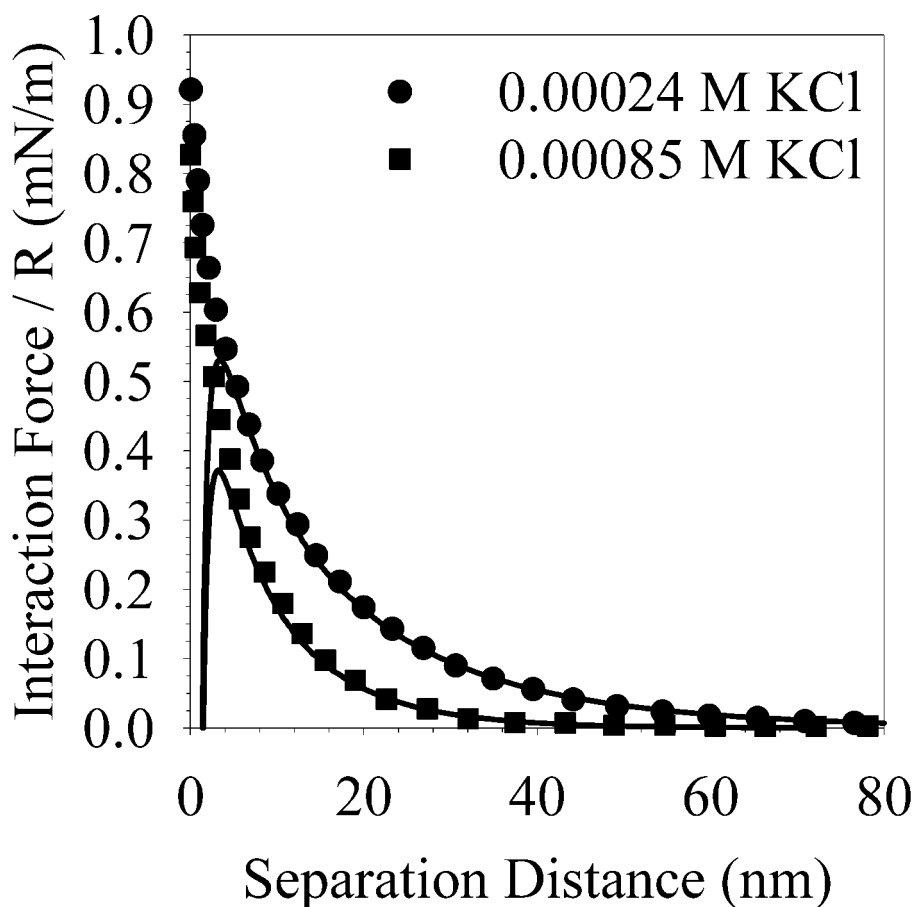


Figure 6-5: Interaction Force Profile between Heat Treated Surfaces. Experimentally measured force profiles for the surfaces heated at 600 °C at pH 4 in 2.4×10^{-4} and 0.85×10^{-3} M KCl solution. Curves were fit using the standard application of non-linear DLVO theory with a constant charge boundary condition, a Hamaker constant of 12×10^{-21} J, and non-retarded van der Waals forces. This procedure yielded a Stern potential at infinite separation distance of -33 mV for the lower ionic strength solution and -22 mV for the higher ionic strength solution.

different experiments in both the boiled and heat treated samples. Additionally, none of the force profiles showed adhesion upon separation of the surfaces.

In Figure 6-6, a representative interaction force profile (approaching) and the retracting (adhesion) curve is presented for a heat treated sample at pH 2 in 0.02 M KCl.

When surface potential is low and electrolyte concentration is high, no long range

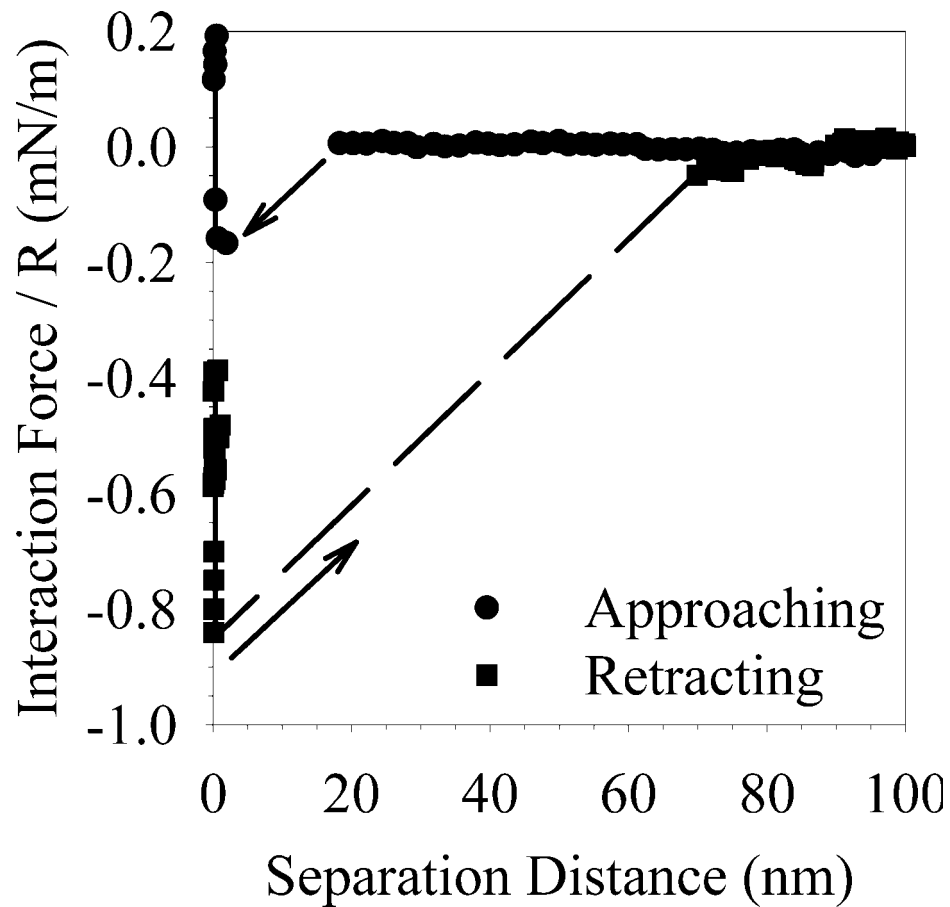


Figure 6-6: Interaction Force Profile in Attractive Regime. Experimentally measured force profile for 600 °C heat treated surfaces at pH 2 in 0.2 M KCl solution. Both the approaching and retracting curves are presented. Upon approach to the surface, at approximately 17 nm, the attractive force gradient becomes large enough to cause the cantilever to jump to the surface (indicated by arrow). Similarly, the cantilever must be deflected 70 nm (8.4 nN) before detachment from the surface occurs (indicated by dashed line and arrow).

repulsion is observed and as the two surfaces approach each other, attractive van der Waals forces dominate the interaction and cause the surfaces to jump into contact. Furthermore, as the two surfaces are separated significant adhesion is observed.

Discussion

Previous Gel-Layer Models

Figure 6-7 depicts an interaction force curve between boiled surfaces at pH 4 in 2.5×10^{-4} M KCl with fits based on standard application of DLVO theory and by just the electrostatic force as indirectly suggested by Yaminsky et al. [YAM98]. It is clear that at a separation distance of approximately 6 nm, van der Waals attraction begins to dominate in the standard application of DLVO theory resulting in theory deviating from experiment. However, if van der Waals attraction is neglected entirely, below 20 nm the theoretical electrostatic repulsion is significantly greater than the experimentally measured forces. Hence, if structural forces are not to be invoked, the concept of a reduced van der Waals attraction is necessary. Note also that without van der Waals attraction there is also no clear explanation for the attraction measured between surfaces at pH 2 (Figure 6-6).

Homogeneous Gel-Layer Model

To determine which model of a gel-layer most appropriately describes the measured interaction force between glass surfaces, the experimental effective Hamaker constant, A_{eff} , as a function of separation distance must be determined. To extract this parameter many curves were first fitted to the numerical solution of electrostatic repulsion at large separation distances. Subsequently, the Hamaker constant required to fit the experimental data at different separation distances was calculated based on the non-retarded van der Waals force between a sphere and flat plate, Eq. (6-7).

$$A_{\text{eff}}(H) = \frac{F_{\text{vdW}} 6H^2}{R} \quad (6-7)$$

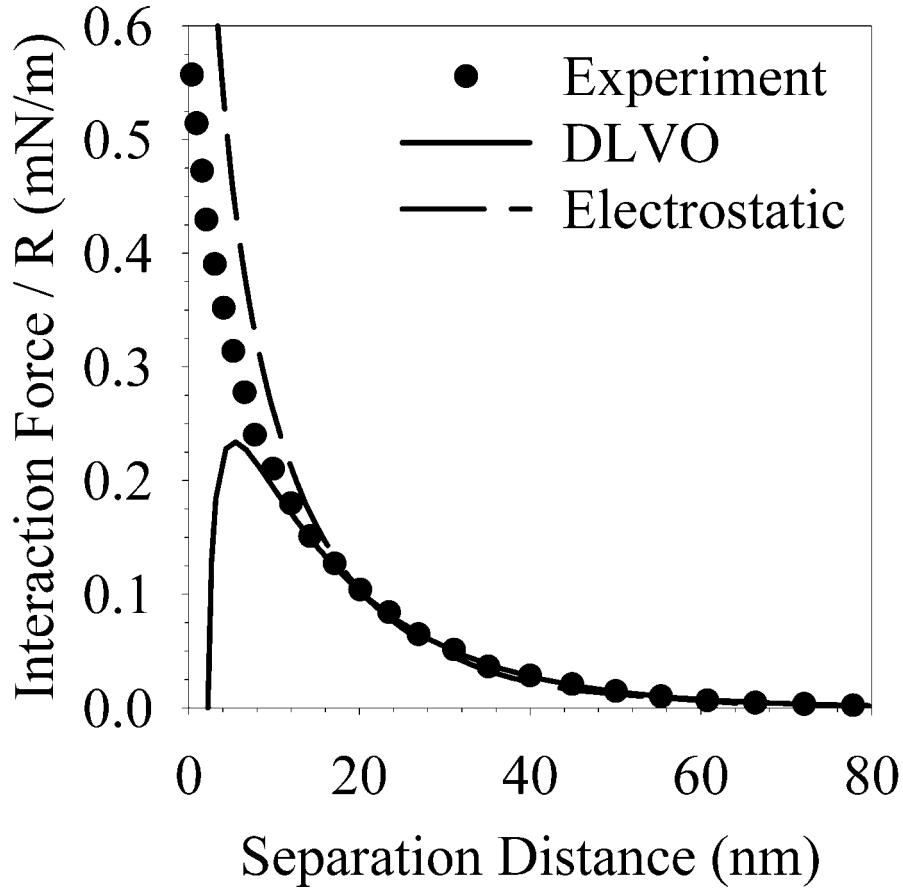


Figure 6-7: Interaction Force Profile with Electrostatic and DLVO Fitting.

Experimentally measured force profile for the boiled glass surface at pH 4 in 2.5×10^{-4} M KCl solution. Shown is the total DLVO force (solid line) and electrostatic component (dashed line) fitted using the standard application of non-linear DLVO theory with a constant charge boundary condition, a Hamaker constant of 12×10^{-21} J, non-retarded van der Waals forces, and a Stern potential at infinite separation distance of -24 mV. To fit the entire measured interaction force an additional repulsive force or reduced van der Waals attractive force is needed.

Where F_{vdW} is the difference in force between the electrostatic repulsion and measured force, H is the separation distance between surfaces, and R is the radius of the sphere used in the experiment. The results of this analysis are shown in Figure 6-8. It was found upon subtracting the electrostatic component that there was no discernable difference in the effective Hamaker constant at different pH or with heat treatment of the

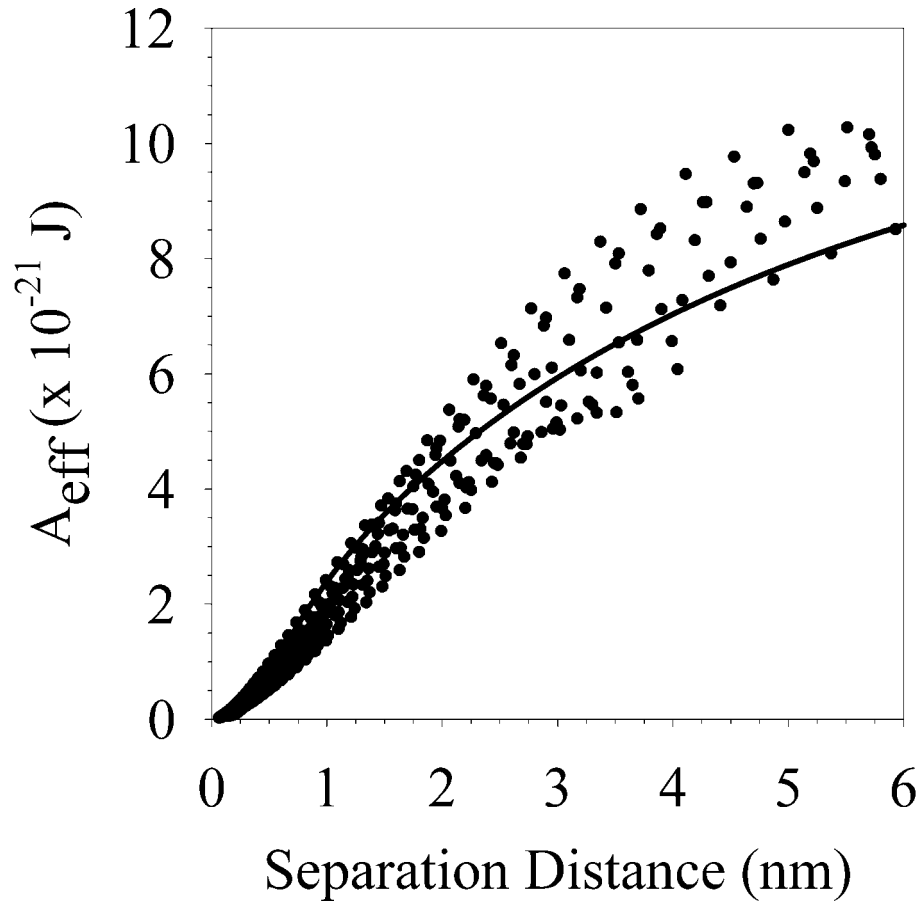


Figure 6-8: Experimental Effective Hamaker Constant. Experimentally determined effective Hamaker constant, A_{eff} , as a function of separation distance for the boiled and heat treated samples at pH 4, 6, and 9. After subtraction of the electrostatic force, no discernable difference in A_{eff} was indicated as a function of pH or ionic strength. Shown also is the best theoretical fit using the transition layer model, Eq (6-6) with the fitting parameters for silica. With a Hamaker constant of 14.2×10^{-21} J an average gel-layer thickness for all conditions investigated is approximately 2.0 nm.

surfaces. Figure 6-8 contains data from all experimental conditions for each of the surfaces. Even though these are glass surfaces, this result is consistent with previous investigations on silica [GRA95] that found that surface treatment had little effect on the non-DLVO forces.

From the data in Figure 6-8, it can be seen that at larger separation distances (> 5 nm) the effective Hamaker constant approaches an asymptote of approximately 14×10^{-21} J. Note that the precise experimental value of the plateau is difficult to determine because the difference between the electrostatic component and the measured profile becomes small. This is also the reason for the increased scatter of the data at larger separation distances. However, at shorter separation distances the value of the effective Hamaker constant decreases rapidly towards zero as the two surfaces approach each other.

Although much easier to apply than the gel model of a compositional gradient, from the experimental determination of A_{eff} in Figure 6-8, the model of a homogeneous gel-layer can not be used to explain the data. At zero separation distance, the lowest A_{eff} would equal the Hamaker constant chosen for the gel-layer. Since experimentally A_{eff} approaches zero, no value can be chosen which will result in a reasonable gel-layer thickness. Hence, to fit A_{eff} below approximately 3 nm a gel-layer model with a gradient of composition must be employed.

Gel-Layer with an Exponential Compositional Decay

Using Eq. (6-6) with the parameters for the silica/water/silica system and using a bulk Hamaker constant, A_{131} , of 14×10^{-21} J, it is possible to perform a best fit analysis of the experimental A_{eff} values in Figure 6-8 with only the gel-layer thickness, δ , as a variable. These results are shown in Figure 6-8 as a solid line. Over the range of separation distances where the non-DLVO force is present, this model seems to provide an adequate explanation of the experimental observations. The average gel-layer thickness for all conditions calculated by this approach is 2.0 nm.

That such thin layers could have a significant impact in the overall surface forces and stability of particles is surprising but may be reasonable. One would also expect, if the gel-layer remained composed of an unbroken silica network, that the stress of accommodating water in the structure would limit the maximum thickness. Also, the non-DLVO force on silica can be measured even if the surface has only been exposed to water for a short period of time (minutes), indicating that the formation of such a layer is rapid. Furthermore, dry techniques such as TEM, NMR, and ellipsometry have not been able to conclusively distinguish the presence of a swelled silica layer indicating that the process is rapidly reversible upon removal from water. These observations suggest that if a gel-layer forms on the silica surface, it needs to be relatively thin in order to meet the kinetic requirements. A relatively fast rate of formation would also explain why the gel-layer thickness calculated for the heat treated sample was similar to the boiled sample.

It is important, to once again revisit the possible effect of such a gel-layer, as described above, on the theoretical behavior of silica. Figure 6-9 shows both the van der Waals attraction between two silica particles in water, and between two particles with a compositional gradient gel-layer of 2.0 nm thickness. Note that at larger distances the modified van der Waals force is lower in magnitude but similar in shape to the prediction without gel-layers. This is the area of interaction where the bulk Hamaker constant dominates the interaction. However, as separation distance becomes smaller the effect of the gel-layer becomes more pronounced as the net attraction actually approaches zero whereas the standard formula predicts strong attraction. This has significant implications in explaining the measured force interactions and colloidal stability under low pH or high ionic strength conditions.

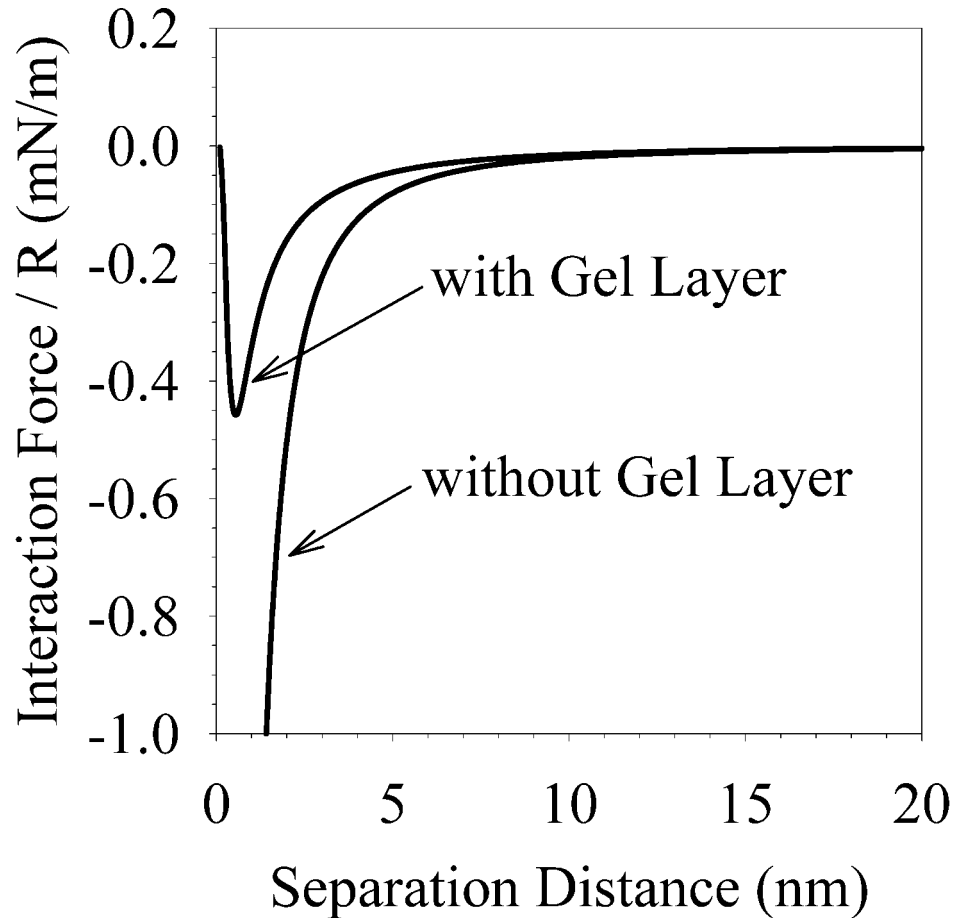


Figure 6-9: Theoretical van der Waals Force Comparison. Comparison of van der Waals attraction between hypothetical silica surfaces with and without transition gel-layers of 2.0 nm thickness and A_{131} of 12×10^{-21} J. Attraction is still predicted in the presence of a transition layer but the magnitude is decreased.

Figure 6-10 depicts a series of theoretical interactions between silica particles with gel-layers as a function of ionic strength. At low ionic strength (e.g. 0.001 M), on the background of a rather large electrostatic repulsion, the modified van der Waals force is less attractive and hence appears on the total force of interaction as an additional repulsive force. However, as ionic strength is increased, van der Waals attraction becomes more significant until at much higher electrolyte concentrations (e.g. 1 M) the theory predicts attraction and adhesion between the surfaces.

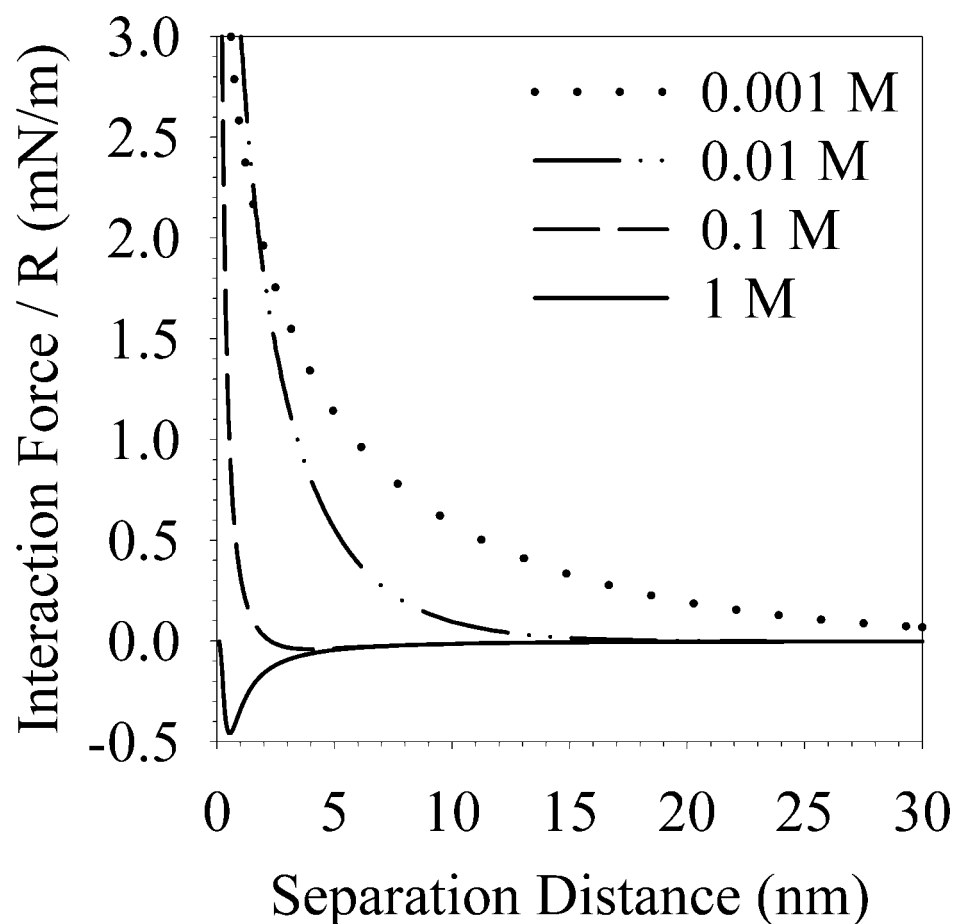


Figure 6-10: Theoretical Interaction Force Profiles. Theoretical force distance profiles for a hypothetical silica surfaces with a gel-layer of 2.0 nm thickness and A_{131} of 12×10^{-21} J. Conditions are 0.001 M at -50 mV (dotted line), 0.01 M at -35 mV (dashed dot dot line), 0.1 M and -12 mV (dashed line), and 1 M at 0 mV (solid line). At low ionic strength and high surface charge the lack of attraction appears as an additional repulsive force. However, as ionic strength is increased van der Waals attraction begins to dominate and instability may occur.

Experimental values for the boiled samples fitted using the modified van der Waals approach are shown in Figure 6-11. A gel-layer thickness of 2.2 nm is used for the low ionic strength curve and 1.9 nm for the data collected in 0.001 M electrolyte solution. These values provide reasonable fits to less than a nanometer separation distance. Several sets of data taken from the literature [GRA95] were also fitted in this manner and yielded

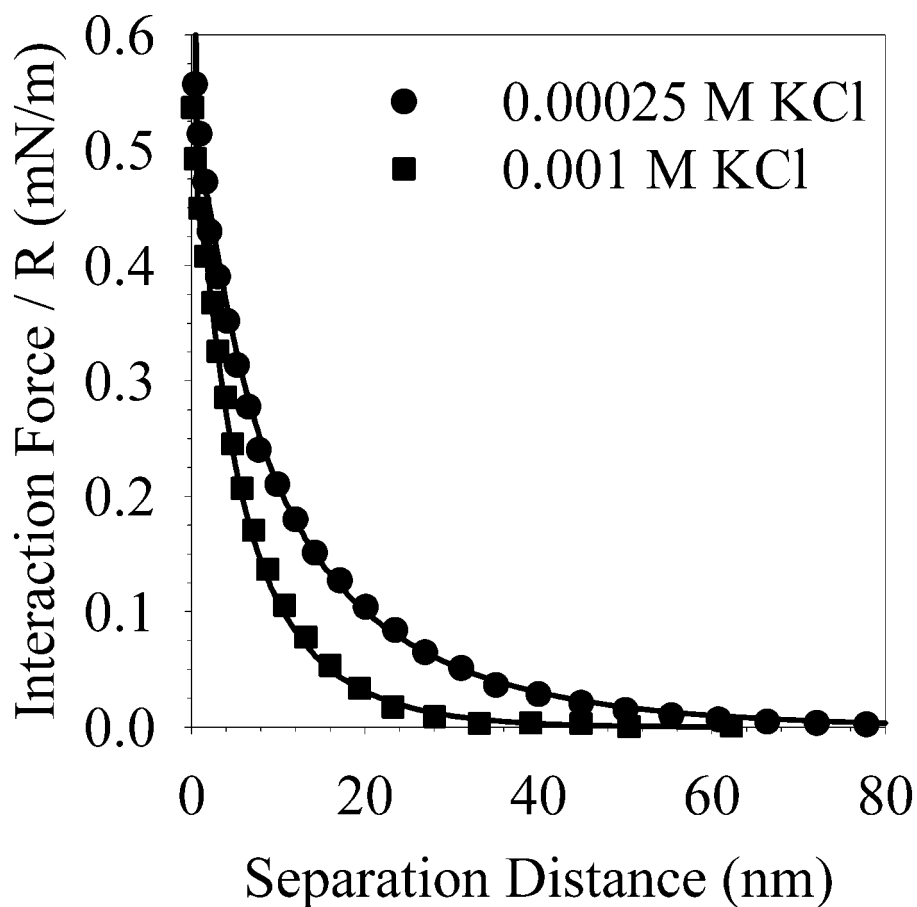


Figure 6-11: Fitted Interaction Force Profiles. Experimentally measured force profiles for boiled glass surfaces at pH 4 in 2.5×10^{-4} and 1.0×10^{-3} M KCl solution. Curves were fit using the same conditions as Figure 4 but van der Waals attraction is reduced by the presence of a 2.2 nm thick gel-layer for the lower ionic strength solution and 1.9 nm for the higher ionic strength solution.

gel-layers of similar thickness. Indicating that this approach may be applicable to both silica and glass systems.

The combination of what appears to be an additional repulsion while retaining the ability to predict the coagulation of silica at low pH or high ionic strength is a unique feature of this approach to modeling the interaction of glass surfaces. Unfortunately, more experimental evidence is needed before a definitive conclusion as to the origin of

the non-DLVO force on silica may be drawn. Although this method of analysis does not completely resolve the issue of structural forces and gel-layers it does suggest that the surface of silica is quite complicated and that multiple processes may be simultaneously occurring.

Summary

Although a large number authors have measured the interaction forces between silica and glass surfaces in aqueous solution, there is still no clear consensus as to the origin of the non-DLVO forces. While not discounting structural forces between silica surfaces it was shown in this study that modeling a gel-layer on silica as a rigid surface, swelled by water could predict the behavior of these materials under a wide variety of solution conditions. This was done by calculating the decrease in van der Waals force that accompanies the formation of a gel-layer.

Once again, as described in this chapter, a non-ideality of the interface on the nanometer scale is seen to have significant impact on interparticle force prediction. That the structure of the interface on this scale should have such a dramatic influence, raises the question as to how interfaces are modeled in general. As more control of ensemble particulate behavior is desired and as limits of particulate processing behavior are extended to extreme conditions, it is likely that many of the concepts discussed in this study and a more detailed description of the both the physical and chemical make up of the interface will be necessary.

CHAPTER 7 SUMMARY AND SUGGESTIONS FOR FUTURE WORK

Summary

Most theoretical descriptions of the interaction of surfaces are derived for ideal surfaces. In other words, for interfaces that may be described as perfectly smooth and discrete. This assumption is generally valid at relatively large surface separation distances. However, in adhesion phenomena and processing in extreme environments (such as high electrolyte concentration, extremes of pH, temperature, or high applied force particles may approach to separation distances where the structure of the interface at the nanometer scale may significantly influence interaction forces and macroscopic behavior. An understanding of these effects is critical to developing next generation processing models.

In this study, it was shown that the non-ideality of interfaces may indeed have dramatic impact for the interaction of surfaces at small separation distances. In adhesion phenomena it was demonstrated that roughness on the order of a nanometer or two was significant enough to reduce the theoretically predicted adhesion for ideal interfaces by an order of magnitude. Furthermore the relative humidity at which capillary forces were first observed increased from approximately 20% to nearly 60%. These observations are expected to have significant influence on the macroscopic behavior of surfaces but are not often accounted for in predictive models. These results also highlight the importance

of the real area in contact and that it is roughness at the smallest scale, that principally controls the adhesion between surfaces.

The key to more accurate prediction of adhesion between surfaces with nanoscale roughness is to improve the manner in which the interface is described. Through development of a model that takes into account both the height of an asperity above an average surface plane as well as its breadth, relationships were developed to predict the experimentally measured adhesion in both dry atmospheres and under humid conditions that allow capillaries to form. A more important consideration, however, is that these models provide a basis for the design of particulates and surfaces of controlled properties.

Similar to adhesion phenomena, the impact of a non-ideal interface was also explored in reference to particles in colloidal suspension. Silica surfaces at small separation distances do not behave as predicted by the sum of van der Waals attraction and electrostatic repulsion. To resolve this dilemma, the interface of silica was modeled as a transition layer with composition ranging from bulk silica to bulk water. Using this description of the interface, it was possible to determine the effect of such a transition layer on the van der Waals and electrostatic forces. If such a transition layer were very thin it would have little effect on the predicted interaction between two particles at large separation distances. However, as the surfaces closely approached one another, the effect of the transition layer would become more pronounced and result in a weakened attraction.

In this investigation, it was determined that a transition layer thickness of approximately two nanometers was sufficient to describe the full range of silica behavior without the need to invoke other types of surface forces. Silica is just one example where

the concept of a transition layer may be useful to describe interaction behavior. One can imagine, that a transition layer on a biological particle, such as a bacteria or virus, could affect its ability to adsorb to filter media. Also the liquid/gas interface is not discrete and varies in density on the nanometer scale. This would have significant implications for wetting films and bubble attachment to surfaces.

The predictive methodologies discussed in this study highlight the importance of characterization of the interface at the nanoscale. For both types of non-ideal interfaces discussed, deviations in the range of a few nanometers dominated system behavior. This characterization is expected to play an important role in the development of predictive models for increased process control.

Suggestions for Future Work

There are several areas in which the topics delineated in this study may be expanded upon and further validated. The problem and influence of nanoscale roughness on particulate adhesion needs to be further investigated in ensemble particulate systems. Experimental observation and theoretical predictions of cohesive powder flow in bins, hoppers, and pneumatic conveying could be performed with particles of controlled surface roughness. Linking this ensemble behavior with macroscopic measurement in controlled shear cells and interactions on the particle level is necessary for advanced design of particulate handling systems and design of particles with predictable flow behavior.

It is also clear that when two particles contact one another, they might not always contact at a single asperity and that the average asperity size and spacing developed in this study does not fully describe the asperity size distribution. Due to this distribution

and other randomizing factors, there is not expected to be a single adhesion force at which particles interact. Hence, to truly implement adhesion forces into predictive models of powder flow, statistical methods need to be developed in order to describe the range and probability of the adhesion force for a given interaction. This concept would also be useful in the removal of particulates from surfaces where, with only a few experiments, the force needed to remove a specified percentage of the contaminating particles could be calculated.

Further investigation into the effect of transition layers on interparticle forces is required. In the silica system, the transition layer that may exist on silica in the mid pH regime. However, with regards to chemical mechanical polishing of interlevel dielectric materials, there is interest in delineating the properties and effect of such a layer on the interaction of an abrasive particle and the surface at high pH. In fact, transition layers or other chemically altered layers are expected to play a primary role in controlling the behavior in many polishing systems. The key to accurate prediction of the behavior of these systems is to characterize the surfaces in more detail. Only when the physical, morphological, and chemical properties of these non-ideal interfaces are known may predictions of interparticle force and ensemble behavior be properly attempted.

For both types on non-ideal interface described above, particles may be forced to interact under loads greater than applied in this investigation. Under such forces, plastic deformation between the surfaces may occur. Currently, there are predictions of the adhesion resulting from elastic deformations or plastic deformation but no theory exists that links the two. However, even during a simple indentation hardness measurement, it is clear that some of the energy is dissipated by plastic deformation and some by elastic.

This is evidenced by the difference in depth between the point at which pressure is released and the final depth of the indent. Describing this interaction is critical for the prediction of the flow behavior of soft particles as well as the formation of composite particles. Finite element modeling combined with a time dependent elastic-plastic deformation models (as are currently being developed for soil and rock mechanics applications) could be used to determine energy loss, contact area, and stresses in such an interaction.

LIST OF REFERENCES

- ADA67 Adamson, A. W., Physical Chemistry of Surfaces, 2nd ed., Interscience Publishers, New York, 1967.
- ARM69 Armistead, C. G., Tyler, A. J., Hambleton, F. H., Mitchell, S. A., and Hockey, J. A., J. of Phys. Chem., **73**, 3947 (1969).
- ASH91 Ashby, M. F., and Jones, D. R. H., Engineering Materials 1, Pergamon Press, Oxford, International Ser. On Materials Science and Technology, **34**, 1991.
- ATA98 Ata, A., Synthesis of Composite Particles by Dry Coating Techniques, Ph.D. Dissertation, University of Florida, Gainesville, 1998.
- ATT00 Attard, P., Antelmi, D., and Larson, I., Langmuir, **16**, 1542 (2000).
- BER96 Bergström, L., Meurk, A., Arwin, H., and Rowcliffe, D. J., J. Am. Cer. Soc., **79**, 339 (1996).
- BES97 Besseling N., Langmuir, **13**, 2113 (1997).
- BRA32 Bradley, R. S., Phil. Magazine, Ser. 7, **13**, 853 (1932).
- BRE74 Bree, J. L., Van, M. J., Paulis, J. A., Verhaar, B. J., and Schrau, K., Physica, **78**, 187 (1974).
- BRI90 Brinker, C. J. and Scherer, G. W., Sol-Gel Science: The Physics and Chemistry of Sol-Gel Processing, Harcourt Brace Jovanovich, Boston, 1990.
- BRI92 Briscoe, B. J. and Panesar, S. S., J. Phys. D: Appl. Phys., **25**, A20 (1992).
- BUR99 Burnham, N. A. and Kulik, A. J., in Handbook of Micro/Nano Tribology, 2nd ed., (Bhushan, B. Ed.), CRC Press, New York, 1999.
- CAS48a Casimir, H. B. G. and Polder, D., Phys. Rev., **73**, 360 (1948).
- CAS48b Casimir, H. B. G., Proc. Kon. Nederl. Akad. Wetensch., B., **51**, 793 (1948).
- CHA13 Chapman D. L., Phil. Mag., **25**, 475 (1913).
- CHA80 Chan, D. Y. C., Pashley, R. M., and White, L. R., J. Colloid and Interface Sci., **77**, 283 (1980).

- CHR85 Christenson, H. K., J. Colloid and Interface Sci., 104, 234 (1985).
- CHR87 Christenson, H. K. and Blom, C. E., J. Chem. Phys., 86, 419 (1987).
- COE78a Coelho, M. C. and Harnby, N., Powder Tech., 20, 197 (1978).
- COE78b Coelho, M. C. and Harnby, N., Powder Tech., 20, 201 (1978).
- COL98 Colic, M., Fisher, M. L., and Franks, G. V., Langmuir, 14, 6107 (1998).
- COO90 Cook, L. M., J. of Non-Crystalline Solids, 120, 152 (1990).
- CZA80 Czarnecki, J. and Dabros, T., J., Colloid and Interface Sci., 78, 25 (1980).
- DAG00 Dagastine, R. R., Prieve, D. C., and White, L. R., J. Colloid and Interface Sci., 231, 351 (2000).
- DEB36 de Boer, J. H., Trans. Faraday Soc., 32, 10 (1936).
- DEL99 de Lazzer, A., Dreyer, M., and Rath, H. R., Langmuir, 15, 4551 (1999).
- DER34 Derjaguin, B. V., Kolloid Zeitschrift, 69, 155 (1934).
- DER41 Derjaguin, B. V. and Landau, L. D., Acta Phys. Chim. USSR, 14, 633 (1941).
- DER74 Derjaguin, B. V. and Churaev, N. V., J. of Colloid and Interface Sci., 49, 249 (1974).
- DER75 Derjaguin, B. V., Muller, V. M., and Toporov, Y. P., J. Colloid Interface Sci., 53, 314 (1975).
- DER84 Derjaguin, B. V. and Churaev, N. V., Wetting Films, Nauka, Moscow, 1984.
- DER87 Derjaguin, B. V., Churaev, N. V., and Muller, V. M., Surface Forces, Plenum Publishing Corp., New York, 1987.
- DER88 Derjaguin, B. V., Churaev, N. V., and Rabinovich, Y. I., Advances in Colloid and Interface Sci., 28, 197 (1988).
- DUC91 Ducker, W., Senden, T., and Pashley, R. M., Nature, 353, 239 (1991).
- DUC92 Ducker, W. A. and Senden, T. J., Langmuir, 8, 1831 (1992).
- DUC94 Ducker, W., Xu, Z., Clarke, D., and Israelachvili, J. N., J. of the Amer. Cer. Soc., 77, 437 (1994).
- FER00 Fernández-Vera, J. M., Garcia-Molina, R., J. Colloid and Interface Sci., 231, 394 (2000).

- FIE96 Fielden, M. L., Colloidal Forces Measured between Two Solid Surfaces and between a Solid Surface and a Bubble, Ph.D. Dissertation, Univ. of South Australia, Adelaide, Australia, 1996.
- FIS81a Fisher, L. R. and Israelachvili, J. N., J. Colloid Interface Sci., 80, 528 (1981).
- FIS81b Fisher, L. R., Gamble, R. A., and Middlehurst, J., Nature, 290, 575 (1981).
- FIS81c Fisher, L. R. and Israelachvili, J. N., Colloids and Surfaces A: Physicochem. Eng. Aspects, 3, 303 (1981).
- FOR97 Forsman, J., Woodward, C. E., and Jönsson, B., Langmuir, 13, 5459 (1997).
- FU98 Fu, Z. and Santore, M., Colloids and Surfaces A, 135, 63 (1998).
- FUJ99 Fuji, M., Machida, K., Takei, T., Watanbe, T., and Chikazawa, M., Langmuir, 15, 4584 (1999).
- FUL75 Fuller, K. N. G. and Tabor, F. R. S., Proc. Roy. Soc. London A: Math. and Phys. Sci., 345, 327 (1975).
- GIN72 Gingell, D. and Parsegian, V. A., J. Theor. Biol., 36, 41 (1972).
- GOU10 Gouy, G., J. Phys. Radium, 9, 457 (1910).
- GRA47 Grahame, D.C., Chem. Rev., 41, 441 (1947).
- GRA93 Grabbe, A. and Horn, R., J. of Colloid and Interface Sci., 157, 375 (1993).
- GRA95 Grabbe, A., Michalske, T. A., and Smith, W. L., J. Phys. Chem., 99, 4648 (1995).
- GRE66 Greenwood, J. A. and Williamson, J. B. P., Proc. Roy. Soc. London A: Math. and Phys. Sci., 295, 300 (1966).
- GRE81 Gregory, J., J. Colloid and Interface Sci., 83, 138 (1981).
- HAM37 Hamaker, H. C., Physica, 4, 1058 (1937).
- HEN31 Henry, D. C., Proc. Roy. Soc. (London), A133, 106 (1931).
- HER81 Hertz, H., J. Reine Angew. Math., 92, 156 (1881).
- HOG66 Hogg, R., Healy, T. W., and Feurstenau, D. W., Trans. Faraday Soc., 62, 1638 (1966).
- HOR89 Horn, R., Smith, D., and Haller, W., Chem. Phys. Lett., 162, 404 (1989).
- HOR92 Horn, R. G. and Smith, D. T., Science, 256, 362 (1992).

- HOU80 Hough, D. B. and White, L. R., Adv. Colloid and Interface Sci., 14, 3 (1980).
- HÜC24 Hückel, E., Physik. Z., 25, 204 (1924).
- HUN01 Hunter, R. J., Foundations of Colloid Science, 2nd ed., Oxford University Press, Oxford, 2001.
- IID93 Iida, K., Otsuka, A., Danjo, K., and Sunada, H., Chem. Pharm. Bull., 41, 1621, (1993).
- ILE79 Iler, R., The Chemistry of Silica, Wiley-Interscience, New York, 1979.
- ISR92 Israelachvili, J. N., Intermolecular and Surface Forces, Academic Press, London, 1992.
- JOH71 Johnson, K. L., Kendall, K., and Roberts, A. D., Proc. Roy. Soc. London A: Math. and Phys. Sci., 324, 301 (1971).
- JOH97 Johnson, K. L. and Greenwood, J. A., J. Colloid Interface Sci., 192 326 (1997).
- KAM98 Kamiya, H., Yoshida, M., and Mitsui, M., in Surface-Controlled Nanoscale Materials for High Value Added Applications: Materials Research Society Proceedings Vol. 501, p. 241, MRS, Warrendale, PA, 1998.
- KOH00 Kohonen, M. M. and Christenson, H. K., Langmuir, 16, 7285 (2000).
- KRU67 Krupp, H., Adv. Colloid Interface Sci., 1, 111 (1967).
- LAN72 Langbein, D. J., Adhesion, 3, 213 (1972).
- LAN74 Langbein, D. J., Adhesion, 6, 1 (1974).
- LEN28 Lennard-Jones, J. E. and Dent, B. M., Trans. Faraday Soc., 24, 98 (1928).
- LIF56 Lifshitz, E. M., Sov. Phys. JETP, 2, 73 (1956).
- LIU96 Liu, C. C. and Maciel, G. E., J. Amer. Chem. Soc., 118, 5103 (1996).
- LON37 London, F., Trans. Faraday Soc., 33, 8 (1937).
- LYK95 Lyklema, J., Fundamentals of Interface and Colloid Science, Vol. II: Solid-Liquid Interfaces, Academic Press, London, 1995.
- MAH76 Mahanty, J. and Ninham, B. W., Dispersion Forces, Academic Press, New York (1976).
- MAR93 Marmur, A., Langmuir, 9, 1922 (1993).

- MAS94 Masuda, H., Gotoh, K., Fukada, H., and Banba, Y., Adv. Powder Technology, 5, 205 (1994).
- MAU84 Maugis, D. and Pollock, H. M., Acta Metall., 32, 1323 (1984).
- MAU92 Maugis, D., J. Colloid and Interface Sci., 150, 243 (1992).
- MEA92 Meagher, L., J. of Colloid and Interface Sci., 152, 293 (1992).
- MEL89 Melrose, J. C., Langmuir, 5, 293 (1989).
- MEU97 Meurk, A., Luckham, P. F., and Bergstrom, L., Langmuir, 13, 389 (1997).
- MIL92 Miller, J. D., Yalamanchili, M. R., and Kellar, J. J., Langmuir, 8, 1464 (1992).
- MIZ96 Mizes, H. A., in Advances in Particle Adhesion, (D. S. Ramani and L. H. Sharpe, Eds.) p. 155. Gordon and Breach Publishers, Australia, 1996.
- NIN70a Ninham, B. W., and Parsegian, V. A., Biophys. J., 10, 646 (1970).
- NIN70b Ninham, B. W., and Parsegian, V. A., J. Chem Phys., 53, 3398 (1970).
- NIN97 Ninham, B. W., and Yaminsky, V. V., Langmuir, 13, 2097 (1997).
- OSH82 Ohshima, H., Healy, T. W., and White, L. R., J. Colloid and Interface Sci., 89, 484 (1982).
- OSH94 Ohshima, H., J. Colloid and Interface Sci., 168, 269 (1994).
- PAR72 Parsegian, V. A. and Weiss, G. H., J. Colloid Interface Sci., 40, 35 (1972).
- PAS77 Pashley, R. M., J. Colloid and Interface Sci., 62, 344 (1977).
- PAS80 Pashley, R. M., J. Colloid and Interface Sci., 80, 153 (1980).
- PAS82 Pashley, R. M., J. Colloid and Interface Sci., 83, 531 (1982).
- PAS83 Pashley, R. M. and Israelachvili, J. N., J. Colloid and Interface Sci., 97, 446 (1983).
- PED98 Pederson, H. G., Particle Interactions An AFM Study of Colloidal Systems, Ph.D. Dissertation, Technical University of Denmark, 1998.
- PES82 Peschel, G., Belouschek, P., Müller, M. M., Müller, M. R., and König, R., Colloid and Polymer Sci., 260, 444 (1982).
- PIE67 Pietsch, W. and Rumpf, H., Chemie-Ing. Techn., 39, 885 (1967).
- QUO00 Quon, R. A., Ulman, A., and Vanderlick, T. K., Langmuir, 16, 8912 (2000).

- RAB82 Rabinovich, Y., Derjaguin, B.V., and Churaev, N.V., Adv. in Colloid Sci., 16, 63 (1982).
- RAB89 Rabinovich, Ya. I. and Churaev, N. V., Colloid J. USSR, 51, 65 (1989).
- RAB90 Rabinovich, Y. I. and Churaev, N. V., Colloid J. USSR, 52 256 (1990).
- RAB91 Rabinovich, Y. I., Movchan, T. G., Churaev, N. V., and Ten, P. G., Langmuir, 7, 817 (1991).
- RAB94 Rabinovich, Ya. I. and Yoon, R.-H., Colloids and Surfaces A, 93, 263 (1994).
- RUM90 Rumpf, H., Particle Technology, Chapman and Hall, London, 1990.
- SCH95 Schaefer, D. M., Carpenter, M., Gady, B., Reifenberger, R., DeMejo, L. P., and Rimai, D. S., in Fundamentals of Adhesion and Interfaces, (D. S. Rimai, L. P. DeMejo, and K. L. Mittal, Eds.), p. 35. VSP, 1995.
- SIN97 Singh, R. K., Ata, A., Fitz-Gerald, J., Rabinovich, Y. I., and Hendrickson, W., Kona: Powder and Particle, 15, 121 (1997).
- SIR00 Sirghi, L., Nakagiri, N., Sugisaki, K., Sugimura, H., and Takai, O., Langmuir, 16, 7796 (2000).
- SKI72 Skinner, L. M. and Sambles, J. R., Aerosol Sci., 3, 199 (1972).
- SMO21 Smoluchowski, M. von, Handbuch der Electricität und des Magnetismus, Vol. II, Brath, Leipzig, 1921.
- STE24 Stern, O., Z. Electrochem., 30, 508 (1924).
- TAB69 Tabor, D. and Winterton, R. H. S., Proc. R. Soc. London A, 312, 435 (1969).
- TAB77 Tabor, D., J. Colloid and Interface Sci., 58, 2 (1977).
- TAD68 Tadros, Th. F. and Lyklema, J., J. Electroanal. Chem., 17, 267 (1968).
- VAN68 van Kampen, N. G., Nijboer, B. R. A., and Schram, K., Phys. Lett. A, 26, 307 (1968).
- VAN73 van der Waals, J. D., Over de Continuïteit van de Gas- En Vloeistofoestand (On the Continuity of the Gaseous and Liquid States), Ph.D. Dissertation, Leiden University, Netherlands, 1873.
- VEE97 Veeramasuneni, S., Hu, Y., and Miller, J. D., Surface Science, 382, 127 (1997).
- VER48 Verwey, E. J. W. and Overbeek, J. Th. G., Theory of the Stability of Lyophobic Colloids, Elsevier, Amsterdam, 1948.

- VIG94 Vigil, G., Xu, Z., Steinberg, S., and Israelachvili, J. N., J. of Colloid and Interface Sci., 165, 367 (1994).
- VIS72 Visser, J., Adv. Colloid Interface Sci., 3, 331 (1972).
- XIA00 Xiao, X., and Qian, L., Langmuir, 16, 8153 (2000).
- XIE97 Xie, H. Y., Powder Tech., 94, 99 (1997).
- YAM75 Yaminsky, V. V., Yusupov, R. K., Amelina, A. A., Pechelin, and V. A., Shchukin, E. D., Colloid J. USSR, 37, 918 (1975).
- YAM98 Yaminsky, V. V., Ninham, B. W., and Pashley, R. M., Langmuir, 14, 3223 (1998).
- YOT93a Yotsumoto, H. and Yoon, R.-H., J. Colloid and Interface Sci., 157, 426 (1993).
- YOT93b Yotsumoto, H. and Yoon, R.-H., J. Colloid and Interface Sci., 157, 434 (1993).
- ZHM00 Zhmud, B. V., Meurk, A., and Bergstörn, L., Colloids and Surfaces A., 164, 3 (2000).
- ZHU87 Zhuravlev, L. T., Langmuir, 3, 316 (1987).

BIOGRAPHICAL SKETCH

Joshua was born in Concord, Massachusetts on November 6, 1972 to Joel and Judith Adler and was raised in the town of Littleton, Massachusetts with his sister Jerusha. After his freshman year at Littleton High School he transferred to Venice High School, Venice, Florida where he was valedictorian of the class of 1991. By summer 1995 he had earned a Bachelor of Science degree, with honors, from the University of Florida, Gainesville, in the Department of Materials Science and Engineering with a specialization in Ceramics Science. He then continued his education in pursuit of a Doctor of Philosophy degree in the Department of Materials Science and Engineering. In the Spring of 2001 he earned this degree with specializations in both Ceramics Science and Particle Science and Technology. The latter specialty arose from extensive collaboration with and participation in the NSF Engineering Research Center for Particle Science and Technology at the University of Florida. After graduation he plans to join Intel Corporation, Portland, Oregon.